Titre: Title:	Modeling and Optimization of Solar Power Plants with Battery Energy Storage Systems
Auteur: Author:	Marie-Liesse Koch
Date:	2026
Type:	Mémoire ou thèse / Dissertation or Thesis
Référence: Citation:	Koch, M.-L. (2026). Modeling and Optimization of Solar Power Plants with Battery Energy Storage Systems [Mémoire de maîtrise, Polytechnique Montréal]. PolyPublie. https://publications.polymtl.ca/76208/

URL de PolyPublie: PolyPublie URL:	https://publications.polymtl.ca/76208/
Directeurs de recherche: Advisors:	Michaël Kummert
Programme: Program:	Génie énergétique

POLYTECHNIQUE MONTRÉAL

affiliée à l'Université de Montréal

Modeling and Optimization of Solar Power Plants with Battery Energy Storage Systems

MARIE-LIESSE KOCH

Département de génie mécanique

Mémoire présenté en vue de l'obtention du diplôme de *Maîtrise ès sciences appliquées*

Génie énergétique

Mars 2026

POLYTECHNIQUE MONTRÉAL

affiliée à l'Université de Montréal

Ce mémoire intitulé :

Modeling and Optimization of Solar Power Plants with Battery Energy Storage Systems

présenté par **Marie-Liesse KOCH**

en vue de l'obtention du diplôme de *Maîtrise ès sciences appliquées*

a été dûment accepté par le jury d'examen constitué de :

Hanane DAGDOUGUI, présidente

Michaël KUMMERT, membre et directeur de recherche

Jean-Marie KLEIN, membre externe

DEDICATION

“We discover the path not by seeing the end, but by moving forward, one step at a time.”

ACKNOWLEDGEMENTS

I would like to sincerely thank my master thesis supervisor, Michaël Kummert, for his guidance, expertise, and advice throughout this research. His support and encouragement have been essential.

I would also like to thank the team at Equans for their support during this project. I am especially grateful to Nicolas for trusting me with this work, and to Jean-Marie and Benoît for their constant assistance, advice, and encouragement throughout the project. Your guidance and collaboration were essential in the successful completion of this research.

Finally, I wish to acknowledge the Beelab for providing a stimulating research environment and access to the resources and discussions that greatly facilitated this work.

RÉSUMÉ

Le secteur de l'énergie est actuellement le principal contributeur aux émissions mondiales de gaz à effet de serre, représentant environ 75 % des émissions totales, ce chiffre comprenant la production de cette énergie, son transport et sa consommation finale (Ge & Friedrich, 2024). Pour cette raison, la décarbonation de la production d'énergie constitue un enjeu central des efforts internationaux visant à limiter le changement climatique.

Dans ce contexte, le déploiement à grande échelle des centrales photovoltaïques (PV) s'accélère dans le monde entier (IEA, 2024a). Bien que la production photovoltaïque soit aujourd'hui une technologie mature et compétitive sur le plan économique, sa variabilité et son imprévisibilité posent des défis lors de son intégration au réseau et de sa participation aux marchés d'électricité (Gevorgian et al., 2022). Les systèmes de stockage d'énergie par batteries (BESS) sont de plus en plus proposés pour atténuer cette variabilité, améliorer la flexibilité opérationnelle et augmenter la valeur économique des systèmes (Gifford, 2020).

Cependant, de nombreuses évaluations technico-économiques des centrales PV couplées à des BESS reposent sur des hypothèses de modélisation simplifiées, telles qu'une résolution temporelle insuffisante, un comportement des batteries idéalisé et une prise en compte limitée de la dégradation. Pour pallier ces limitations, un cadre de modélisation complet a été développé avec le langage de programmation Julia (Bezanson et al., 2017) pour étudier les stratégies d'intégration PV-BESS. Ce travail aborde plusieurs défis de modélisation : la représentation précise de la production PV, la modélisation réaliste du comportement dynamique et du vieillissement des batteries, et l'évaluation de scénarios à l'échelle du réseau.

Un modèle PV a d'abord été développé à partir des travaux de Duffie et Beckman (2013). Les résultats ont montré que l'ignorance des fluctuations de l'irradiance à l'échelle minute peut conduire à une sous-estimation du vieillissement cyclique des batteries, soulignant l'importance de données PV à haute résolution. Pour y remédier, une méthodologie de reconstitution de données solaires à la minute à partir de données horaires (*downscaling*) inspirée de celle développée par Hofmann (2014) a été reproduite et améliorée.

Ensuite, un modèle dynamique de batterie basé sur une représentation en circuit équivalent a été développé et couplé à des modèles de vieillissement calendaire et cyclique. Le modèle a été calibré à partir de données publiques de la cellule commerciale K2 LFP18650E (Chueh et al., 2024; K2

Energy Solutions, Inc., n.d.-a). Contrairement aux modèles conventionnels utilisés dans des logiciels comme SAM (NREL, 2025) ou PVsyst (PVsyst SA., 2025), qui dépendent uniquement de l'état de charge (SOC), le modèle présenté prend en compte à la fois le SOC et le courant.

Pour garantir une application réaliste à l'échelle des centrales solaires, tous les composants électriques du système PV - incluant les onduleurs, transformateurs et équipements auxiliaires - ont été intégrés dans le cadre de simulation. Plusieurs stratégies d'intégration ont ensuite été analysées pour répondre à différents objectifs opérationnels :

- La stabilisation du réseau via le déplacement de la charge vers des heures de consommations plus élevées
- Le lissage de la production solaire pour pouvoir améliorer la prévisibilité la génération PV
- L'optimisation financière via la participation aux marchés de l'électricité.

Globalement, cette étude confirme que la performance et le vieillissement des batteries dépendent fortement de leur scénario d'utilisation. Selon la stratégie de déploiement, les BESS intégrés peuvent répondre efficacement à de multiples défis techniques et réseau. De plus, lorsqu'ils sont correctement gérés, les systèmes PV-BESS peuvent être économiquement viables et, dans certains cas, rentables.

ABSTRACT

The energy sector is currently the predominant contributor to global greenhouse gas emissions, accounting for approximately 75 % of total emissions, including energy production, transportation, and end-use consumption (Ge & Friedrich, 2024). For this reason, decarbonizing energy production is at the heart of international efforts to mitigate climate change.

In that context, large-scale deployment of photovoltaic (PV) power plants is accelerating worldwide (IEA, 2024a). While PV generation is today a mature and cost-competitive technology, its inherent variability and unpredictability pose challenges for grid integration and market participation (Gevorgian et al., 2022). Battery energy storage systems (BESS) are increasingly presented as a solution to mitigate this variability, improve operational flexibility and increase economic value (Gifford, 2020).

However, many techno-economic assessments of PV-coupled BESS power plants rely on simplified modeling assumptions, such as using insufficiently detailed temporal resolution, idealized battery behavior, and limited consideration of degradation effects.

To investigate this topic, a comprehensive modeling framework has been developed in the Julia programming language (Bezanson et al., 2017) to study PV-BESS integration strategies. This work addresses several modeling challenges: accurate representation of PV generation data, realistic battery dynamics and aging behavior, and grid level scenario evaluation.

To achieve that goal, a PV model has been first developed based on Duffie and Beckman's work (2013). Additionally, the results of this work showed that ignoring minute-level fluctuations of irradiance can lead to the underestimation of cyclic battery aging, highlighting the importance of minute-resolution PV data for realistic PV-BESS simulations. To address this issue, a downscaling methodology based on Hofmann's (2014) approach has been reproduced and improved.

Then, a dynamic battery model based on an equivalent circuit representation has been developed and coupled with calendar and cycle aging models. The model has been calibrated using publicly available data for the commercial K2 LFP18650E cell (Chueh et al., 2024; K2 Energy Solutions, Inc., n.d.-a). Unlike battery models used in traditional energy simulation software such as SAM (NREL, 2025) or PVsyst (PVsyst SA., 2025), which are based on parameters evolving only with

the battery state of charge (SOC), the presented model's parameters account for both the battery SOC and current.

Finally, to ensure realistic application for utility-scale solar farms, all electrical components of the PV system - including inverters, transformers, and auxiliary equipment – have been integrated into the simulation framework.

To conclude this work, several integration strategies were analyzed to address different operational objectives:

- Grid stabilization through peak shaving and PV production shifting to better match high-demand periods
- Firming solar output by smoothing the generation profile of PV plants
- Financial optimization via participation in electricity markets

Overall, this study confirmed that the performance and aging of the BESS are strongly correlated to their operational utilization. Depending on how they are deployed, integrated BESS can effectively address multiple technical and grid challenges. Furthermore, the results showed that, when properly managed, PV-BESS systems can be economically viable and, in some cases, very profitable.

TABLE OF CONTENTS

LIST OF TABLES

LIST OF FIGURES

LIST OF ABBREVIATIONS AND SYMBOLS

ABBREVIATIONS

AC	Alternative Current
BESS	Battery Energy Storage System
BMS	Battery Management System
CAISO	California Independent System Operator
CAPEX	Capital Expenditure
C-rate	Current rate
CO_2	Carbon Dioxide
DAM	Day-Ahead Market
DC	Direct Current
DHI	Direct Horizontal Irradiation
DNI	Direct Normal Irradiation
DOD	Depth Of Discharge
DPBP	Discount Payback Period
ECM	Equivalent Circuit Model
EOL	End Of Life
IEA	International Energy Agency
IEC	Internation Electrotechnical Commission
IRA	Inflation Reduction Act
IRENA	International Renewable Energy Agency
GHG	Greenhouse Gas
GHI	Global Horizontal Irradiation
GTI	Global Tilted Irradiation

HV	High Voltage
HVAC	Heating Ventilation Air Conditioning
LFP	Lithium Fer Phosphate
LIB	Lithium-ion Battery
LV	Low Voltage
MV	Medium Voltage
NPV	Net Present Value
O&M	Operation and Maintenance
OPEX	Operational Expenditure
PEI	Peak Efficiency Index
PV	Photovoltaic
RAM	Resource Adequacy Market
RTM	Real-Time Market
SOC	State of Charge
SOH	State of Health
STC	Standard Testing Condition
TPM	Transition Probability Matrix

SYMBOLS

	Solar irradiance	
F_{diff}	Diffuse fraction	$-$
F_{ref}	Reflected fraction	$-$
G_{clear}	Received extraterrestrial irradiance	W/m^2
G_{ext}	Extraterrestrial irradiance	W/m^2
G_t	Global tilted irradiance	W/m^2
$G_{b,t}$	Beam tilted irradiance	W/m^2
$G_{r,t}$	Reflected tilted irradiance	W/m^2

G_{sc}	Solar constant	W/m^2
α	Sun elevation	°
	One diode PV model	
E_g	Silicon band gap	eV
G_{ref}	Reference irradiance	W/m^2
I_0	Reverse saturation diode's current	A
I_{mp}	Maximum power current	A
I_{ph}	Photogenerated current	A
I_{sc}	Short-circuit current	A
k_b	Boltzmann constant	J/K
m	Ideality factor	$-$
N_{cs}	Number of cells in series	$-$
q	Elementary charge	C
R_s	Series resistance	Ω
R_{sh}	Shunt resistance	Ω
T_c	Cell temperature – one diode PV model	K
T_{ref}	Reference temperature	K
V_{mp}	Maximum power voltage	V
α	Current temperature coefficient	K/A
β	Voltage temperature coeffiecent	V/A
	Downscaling algorithm	
k_t	Clearness index at time t	-
$\overline{k_{day}}$	Daily average of hourly k_t	-
$\widetilde{k_{day}}$	Daily variability of hourly k_t	-
P_{ij}	Probability to go from state i to j	-
Δk_t	Intra-hour k_t variability	-
	Battery dynamic model	
a_0	Shepherd's model parameter	V
a_1	Shepherd's model parameter	$-$
a_2	Shepherd's model parameter	V

a_3	Shepherd's model parameter	Ah^{-1}
C_{bat}	Battery capacity	Ah
C_1	Polarization capacitance	F
C_{bat}	Battery rated capacity	Ah
C_{eff}	Battery effective capacity	Ah
C_1	Polarization capacitance	F
E_a	Activation energy	kj/mol
I_{bat}	Battery current	A
k	Peukert coefficient	$-$
P_{bat}	Battery power	W
R_{int}	Internal resistance	Ω
R_0	Ohmic resistance	Ω
R_1	Polarization resistance	Ω
V_{bat}	Battery Voltage	V
$V_{cut-off}$	Battery cut-off voltage	V
V_{nom}	Battery nominal voltage	V
V_{OC}	Battery open voltage	V
τ	Transient time constant	s
	Battery aging model	
A	Cyclic aging parameter	$\%.Ah^{-z}$
a, b	Calendar aging model parameters	$-$
$C_{degradation}$	Calendar aging degradation	%
$C^*_{degradation}$	Cyclic aging degradation	%
R	Gas constant	$J.mol^{-1}.K^{-1}$
z	Cyclic aging parameters	$-$
	Solar farm architecture	
C_{bat}	Thermal capacitance of the battery	$J.K^{-1}$
C_{cont}	Thermal capacitance of the container	$J.K^{-1}$
EI_A	Efficiency index	$-$
k	Load factor of the transformer	%

k_{PEI}	Load factor at the peak efficiency index	%
N_{cell}	Number of battery cells in the pack	$-$
P_0	No load loss	W
P_{Aux}	Power sent to the auxiliary components	MW
P_{Bat}	Battery power between the BESS container and the battery inverter	MW
$P_{Bat,Inv}$	Battery power between the battery inverter and the MV transformer	MW
$P_{Bat,MV}$	Battery power between the MV transformer and the grid junction	MW
P_{c0}	Cooling power	W
P_{DA}	Power committed in the day-ahead market	MW
P_{RT}	Power actually sold in the real-time market	MW
P_{Grid}	Power at the grid junction	MW
$P_{Grid,HV}$	Power inhected into the grid, after the HV transformer	MW
P_{HVAC}	HVAC power	W
$P_{PV,Inv}$	PV power post invertor	MW
$P_{PV,MV}$	PV power post MV transformer	MW
PEI	Peak Efficiency Index	%
R_w	equivalent resistance of the wires	Ω
S_r	Rated power of the transformer	VA
T_{bat}	Battery temperature	K
T_{cont}	Container temperature	K
R_0	Battery internal resistance	Ω
UA_{bat}	Heat transfer coefficient between battery and container air	W/K
UA_{cont}	Heat transfer coefficient between ambient air and container	W/K
Π_{gain}	Total revenue	$
Π_{DA}	Day-ahead prices	$\$/MWh$
Π_{RT}	Real-time prices	$\$/MWh$
η_{HVAC}	HVAC efficiency	$-$

Battery integration scenario		
$C_{initial}$	Initial cost (i.e. CAPEX)	\$
f	Scalar form factor in scenario 2	m^2
i	Inflation rate	%
r	Nominal discount rate	%
$t_{evening}$	Difference between the stop of the ramp-down time and the sun set	min
$t_{morning}$	Difference between the start of the ramp-up time and the sun rise	min
P_{obj}	Setpoint instruction for the BESS in all scenarios	MW
$P_{cut-off}$	Maximum PV power allowed to be exported to the grid in scenario 1	MW
γ_i	Penalty weights in the different optimization processes	$-$

LIST OF APPENDICES

CHAPTER 1 INTRODUCTION

The energy transition is now widely recognized as a necessity to meet climate targets and carbon neutrality. According to the International Energy Agency, a rapid and large-scale deployment of renewable energy sources is required to achieve net-zero emission pathways (IEA, 2024a). Among these technologies, photovoltaic (PV) generation plays a central role due to its modularity, rapidly decreasing costs, and global availability. As a result, the increasing penetration of photovoltaic generation in power systems has become a key driver of the energy transition (Wang et al., 2023).

However, the high variability, intermittency and uncertainty of solar resources pose significant challenges for grid integration, particularly at high penetration levels. They include for example, increased ramp rates, reduced predictability of power injections, and potential violations of grid stability constraints. The consequences of these characteristics are known as inflexibility in electric power systems (Rahman et al., 2024).

Battery energy storage systems (BESS) have emerged as a critical technology to mitigate these challenges by providing short-term flexibility, power smoothing, and energy shifting capabilities (Gifford, 2020). In utility-scale applications, batteries can also enable participation in multiple grid services, such as frequency support, power firming, and energy arbitrage, thereby improving the overall financial performance as well as the system flexibility (Rahman et al., 2024).

However, the deployment of BESS remains associated with significant challenges. From an economic perspective, batteries represent a large capital investment, and their profitability depends on the chosen operational strategies and market conditions (NREL, 2024a). Additionally, from an ecological point of view, the manufacturing and end-of-life management of lithium-ion batteries raise concerns related to resource extraction and sustainability (Llamas-Orozco et al., 2023). Moreover, BESS are characterized by limited lifetime and relatively short discharge durations (DOE, 2023). Because of these different challenges, the integration of BESS can be justified only through rigorous long-term performance assessment.

A limitation in existing studies lies in the modeling tools commonly used to evaluate PV and PV-BESS systems. Battery behavior and degradation are very sensitive to short-term power fluctuations induced by PV variability (Omoyele et al., 2024), which require minute-level simulations, whereas tools such as PVsyst (PVsyst SA., 2025) rely on hourly time steps.

Additionally, their battery models are typically limited to equivalent circuit models with fixed parameters, as in SAM (NREL, 2015) and Energy Plus (DOE, n.d.) for example. As a result, those software programs can fail to model SOC or current-dependent responses. They also underestimate degradation mechanisms driven by cycling counting.

This thesis aims to address this gap by developing a complete modeling framework capable of simultaneously representing high-resolution PV production, realistic battery dynamics, and aging mechanisms over long time horizons. The usefulness of the developed framework will be demonstrated by assessing different BESS control strategies to maximize revenue.

1.1 Research objectives

The primary objective of this research is to evaluate the long-term technical and economic performance of grid-connected PV plants equipped with BESS. To achieve this goal, the following sub-objectives are pursued:

- **SO1:** Develop a PV model and data preparation procedure capable of reconstructing minute-level irradiance and power output information.
- **SO2:** Develop a full-domain LFP battery equivalent-circuit model, coupled with an aging model that captures both cycling and calendar degradation mechanisms.
- **SO3:** Construct a complete electrical model of a solar power plant.
- **SO4:** Evaluate different BESS integration strategies by analyzing their impact on the battery performance, aging and their economic return.

1.2 Thesis organization

The remainder of this thesis is structured as follows:

Chapter 2 focuses on PV production modeling and irradiance downscaling. It presents the methodology used to generate minute-resolution PV power data and validates the approach against measured data.

Chapter 3 is dedicated to battery modeling. It introduces the dynamic battery model and the associated aging models, and evaluates their behavior under realistic cycling conditions.

Chapter 4 addresses grid connection and long-term system performance. It integrates the PV and battery models into a complete PV-BESS framework, evaluates grid interaction under multiple operational strategies, and analyzes technical, economic, and aging-related outcomes.

Chapter 5 concludes the thesis by summarizing the main findings and providing recommendations for the design and operation of PV-coupled BESS, as well as directions for future research.

CHAPTER 2 PHOTOVOLTAIC PRODUCTION

The following chapter is separated into two different sections. The first one presents a photovoltaic production model and the second one presents a minute-resolution downscaling algorithm for irradiance.

2.1 Literature review

2.1.1 The growing importance of renewable energy

The deployment of renewable – especially solar – energy systems is one of the most effective and efficient solutions to address the increasingly important issues of oil depletion and climate change mitigation.(Wang et al., 2023)

High levels of renewable energy integration are no longer only projects but already a reality for some areas. As presented by the IEA, "some power systems today are effectively managing high levels of variable renewable energy. Systems such as those in Denmark, Ireland, South Australia and Spain have reached Phase 4 or higher, integrating from 35 up to 75 % of variable renewable energy in their annual generation" (IEA, 2024a). This trend can be considered as a global one. Indeed, installed solar photovoltaics and wind power capacities have more than doubled between 2018 and 2023 in the world. In addition, this growth is not set to be reduced as the COP28 pledged to triple global renewable capacity by 2030. (IEA, 2024a)

By 2025, renewables are projected to generate more electricity worldwide than coal for the first time. Solar PV alone is expected to meet roughly half of the growth in global electricity demand over 2024 and 2025. (IEA, 2024b). A recent report on 2025 first semester confirmed this trend as it show that renewables surpassed coal in global electricity generation for the first time, and that solar and wind growth exceeded global demand growth. (Wiatros-Motyka, 2025)

2.1.2 Photovoltaic production model

2.1.2.1 PV output prediction – Standard one diode model

The following model is based on the model developed by Duffie & Beckman (2013), also used in Pvsyst. It describes the functioning of a standard one diode model, based on the equivalent circuit shown in Figure 2.1.

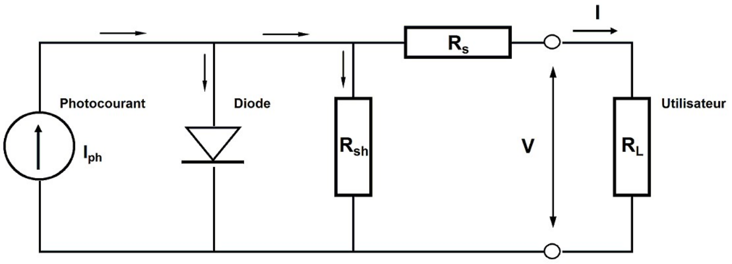

Figure 2.1 - Equivalent circuit model of a PV cell, (Duffie & Beckman, 2013)

The current supplied by the module [in A] is expressed as:

$$I = I_{ph} - I_0\left(exp\left(\frac{V + I.R_s}{N_{cs}V_t}\right) - 1\right) - \frac{V + I.R_s}{R_{sh}} \qquad 2.1$$

Where I_{ph} is the photogenerated current, I_0 is the reverse saturation diode's current, R_s the series resistance, R_{sh} the shunt resistance and $V_t = \frac{mk_bT_c}{q}$ represents the semiconductor thermal voltage, with T_c the effective temperature of the cells and N_{cs} the number of cells in series.

To determine these five parameters, we must first calculate $I_{ph,ref}, I_{0,ref}, R_{s,ref}, R_{sh,ref}$ and $V_{t,ref}$ which are the parameters under STC conditions. To calculate them, the manufacturer provided data for the three characteristics points of a PV panel IV curve can be used. Those data points are the short-circuit current value, the open-circuit voltage value, and the maximum power point coordinates, as shown on Figure 2.2.

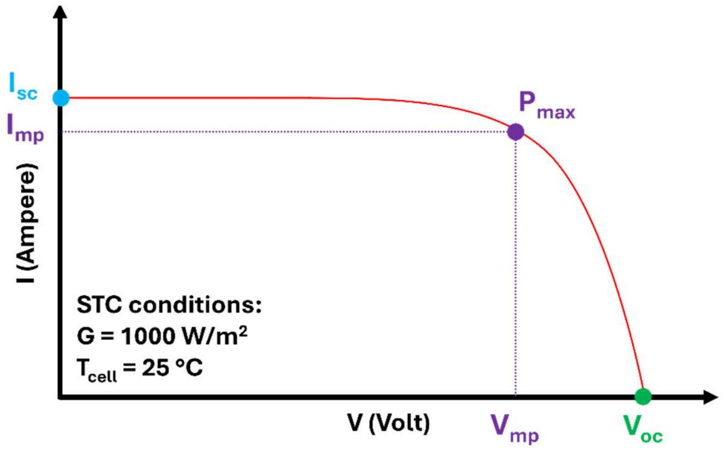

Figure 2.2 - Characteristics points of a PV panel IV curve

The parameters under STC can be calculated using the equations presented in Eq. 2.2, where α is the current temperature coefficient, β the voltage one and E_g is the silicon band gap, equal to 1.121 ev.

$$\begin{cases} I_{ph,ref} = I_{sc} \\ V_{t,ref} = \dfrac{\beta T_{Ref} - V_{OC}}{\dfrac{N_{cs}\alpha T_{Ref}}{I_{sc}} - 3N_{cs} - \dfrac{qE_g N_{cs}}{k_b T_{Ref}}} \\ I_{0,ref} = I_{sc}.exp\left(\dfrac{-V_{OC}}{N_{cs}V_{t,ref}}\right) \\ R_{sh,ref} = \dfrac{V_{mp}}{0.2(I_{sc} - I_{mp})} \end{cases} \quad 2.2$$

Finally, we can calculate $R_{s,ref}$, by solving Eq. 2.1 at maximum power point (V_{mp}, I_{mp}).

Once all parameters have been determined under STC, the effect of temperature can be included to calculate the different parameters under operating conditions. T_c refers to the cell temperature and G_t is the global tilted irradiance, which calculations are presented in Annex A.

$$\begin{cases} I_{ph} = \dfrac{G_t}{G_{ref}}(I_{ph,ref} + \alpha(T_c - T_{Ref})) \\ I_0 = I_{0,ref}\left(\dfrac{T_c}{T_{Ref}}\right)^3 exp\left(\dfrac{qE_g}{k_b}\left(\dfrac{1}{T_{Ref}} - \dfrac{1}{T_c}\right)\right) \\ R_s = R_{s,ref} \\ R_{sh} = \dfrac{G_{ref}}{G_t}R_{sh,ref} \\ V_t = \dfrac{T_c}{T_{Ref}}V_{t,ref} \end{cases} \quad 2.3$$

The cell temperature is estimated as:

$$T_c = T_{amb} + \frac{T_{NOTC} - 20}{800}G_t \quad 2.4$$

PV modules are equipped with maximum power point tracking devices, that set I and V to maximize the output P, meaning that:

$$\left.\frac{dP}{dV}\right|_{Vmp} = 0 \quad 2.5$$

$$I_{mp} + V_{mp}\frac{dI}{dV}\bigg|_{Vmp} = 0$$

From Eq. 2.5 we can deduce the first equation of system 2.6. Its resolution leads to the determination of P_{mp}:

$$\begin{cases} \dfrac{I_{mp}}{V_{mp}} = \dfrac{\dfrac{I_0}{a}exp\left(\dfrac{V_{mp}+I_{mp}R_s}{a}\right)+\dfrac{1}{R_{sh}}}{1+\dfrac{R_s}{R_{sh}}+\dfrac{I_oR_s}{a}exp\left(\dfrac{V_{mp}+I_{mp}R_s}{a}\right)} \\ I_{mp} = I_{ph} - I_o\left(exp\left(\dfrac{V_{mp}+I_{mp}R_s}{N_{cs}V_t}\right)-1\right)-\dfrac{V_{mp}+I_{mp}R_s}{R_{sh}} \\ P_{mp} = V_{mp}I_{mp} \end{cases} \quad 2.6$$

With $a = \frac{k_bT_cN_{cs}}{q}$.

2.1.2.2 PV output prediction – Explicit model

The previous model while being physically accurate has a high computational demand to solve system 2.6. A solution to find P_{mp} more easily is to rewrite Eq. 2.1 using a first order Taylor development (Pedroza-Díaz et al., 2025):

$$exp\left(\frac{I.R_s}{N_{cs}V_t}\right) \approx 1 + \frac{I.R_s}{N_{cs}V_t} \quad 2.7$$

This exponential can be substituted in Eq. 2.1, which allows the variable I to be isolated, becoming an explicit model:

$$I = \frac{I_{ph} - I_0\left(\exp\left(\frac{V}{N_{cs}V_t}\right)-1\right)-\frac{V}{R_{sh}}}{1+\frac{I_0R_s}{N_{cs}*V_t}exp\left(\frac{V}{N_{cs}V_t}\right)+\frac{R_s}{R_{sh}}} \quad 2.8$$

Finally, the power output can be expressed as a function of V alone, which makes it easy to find its maximum.

2.1.2.3 Incident angle modifier

The incidence effect, commonly referred to as the incidence angle modifier (IAM), describes the reduction in the irradiance effectively reaching the surface of the PV cells relative to the irradiance under normal incidence. This reduction is caused by reflections at the glass cover and increases as the angle of incidence becomes larger. (PVsyst, n.d.)

As presented on Figure 2.3, PVsyst implements an IAM function that characterizes the loss of optical transmission as a function of the incidence angle for each PV panels in their database.

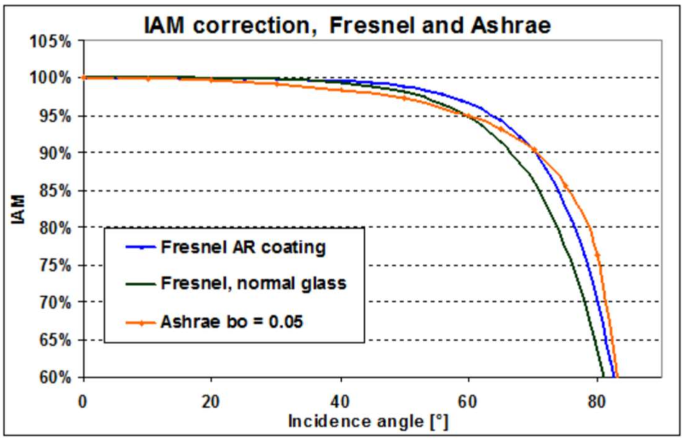

Figure 2.3 - IAM as a function of θ, from (PVsyst SA., 2025)

This factor is applied only to the DNI component of total irradiance. For the diffuse and reflected components, two separate factors need to be calculated (Ríos-Ledesma et al., 2026):

$$\begin{cases} F_{diff} = \dfrac{\int_{\varphi=0}^{\varphi=2\pi} \int_{0}^{\theta^{\varphi}} IAM(\theta)\cos(\theta)\, d\theta d\varphi}{\int_{0}^{2\pi} \int_{0}^{\theta^{\varphi}} \cos(\theta)\, d\theta d\varphi} \\ F_{ref} = \dfrac{\int_{\varphi=0}^{\varphi=2\pi} \int_{\theta^{\varphi}}^{\pi/2} IAM(\theta)\cos(\theta)\, d\theta d\varphi}{\int_{0}^{2\pi} \int_{\theta^{\varphi}}^{\pi/2} \cos(\theta)\, d\theta d\varphi} \end{cases} \quad 2.9$$

Where $\theta^{\varphi} = \arctan\left(\frac{\cot(\beta)}{\cos(\varphi)}\right)$. It is a geometrical angle that represents the azimuth angle of an incoming ray around the module, measured in the PV plane from the direction of maximum tilt. It is used here to separate the ray that comes from above the panel (diffuse) from the one that comes from below (reflected).

Finally, the GTI on the panel is calculated as:

$$GTI^* = IAM(\theta) * G_{b,t} + F_{diff} * G_{d,t} + F_{ref} * G_{r,t} \quad 2.10$$

In situations where only the GHI is available, Erbs model (1982) is used to reconstruct the different irradiance components.

$$\begin{cases} DHI = k_d * GHI \\ DNI = (GHI - DHI)/\cos(\theta_z) \end{cases} \quad 2.11$$

Where θ_z is the zenith angle, and k_d is the diffuse fraction.

The diffuse fraction k_d is calculated using the clearness index k_t, that will be defined with more details in section 2.3.2.2.

$$k_d = \begin{cases} 1 - 0.09 * k_t, & k_t < 0.22 \\ 0.9511 - 0.1604 * k_t + 4.388 * k_t^2 - 16.638 * k_t^3 + 12.336 * k_t^4, & 0.8 > k_t \geq 0.22 \\ 0.165, & k_t > 0.8 \end{cases} \quad 2.12$$

2.2 Model validation: comparison with PVsyst and measured data

2.2.1 IV curve

The reference software used to validate the model is PVsyst (PVsyst SA., 2025). It is a widely used software tool for the design, simulation, and analysis of PV systems, both for academic studies and industrial practice. (PVsyst, n.d.)

To ensure a robust validation of the model, different PV technologies must be considered. Crystalline silicon technologies, which include both monocrystalline and polycrystalline cells, are the most widely adopted, accounting for approximately 87% of global PV module shipments in 2024. Given their dominance in utility-scale solar farms, they serve as a primary reference for performance evaluation. In addition, thin-film technologies (such as CdTe) are also tested, as they offer distinct electrical characteristics. (Precedence Research, 2024)

The I-V curves of three selected PV panel models can be compared under different conditions as presented in Figure 2.4, Figure 2.5, Figure 2.6 and The continuous lines represent PVsyst model results, and the cross markers the previously presented model.

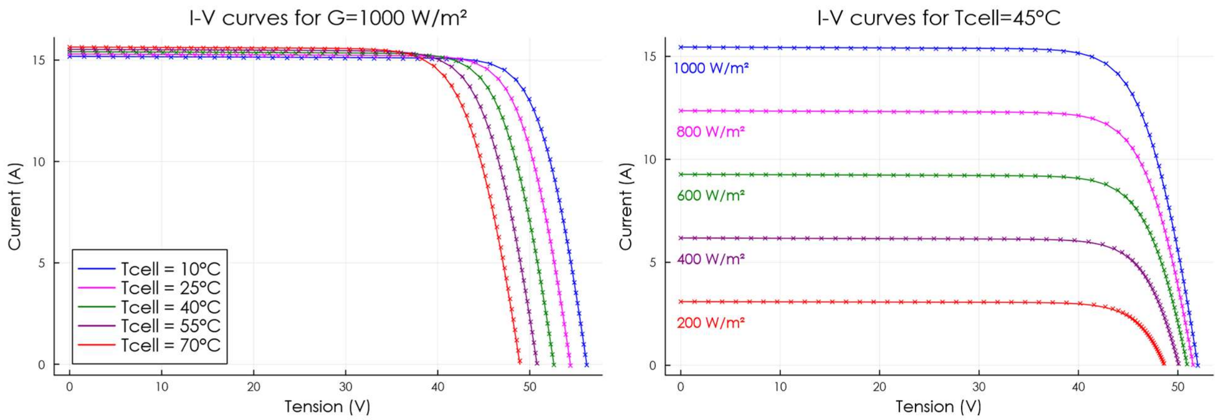

Figure 2.4 - Characteristic curves of the LR7-72HGD-620M Bifacial under different irradiance and cell temperature

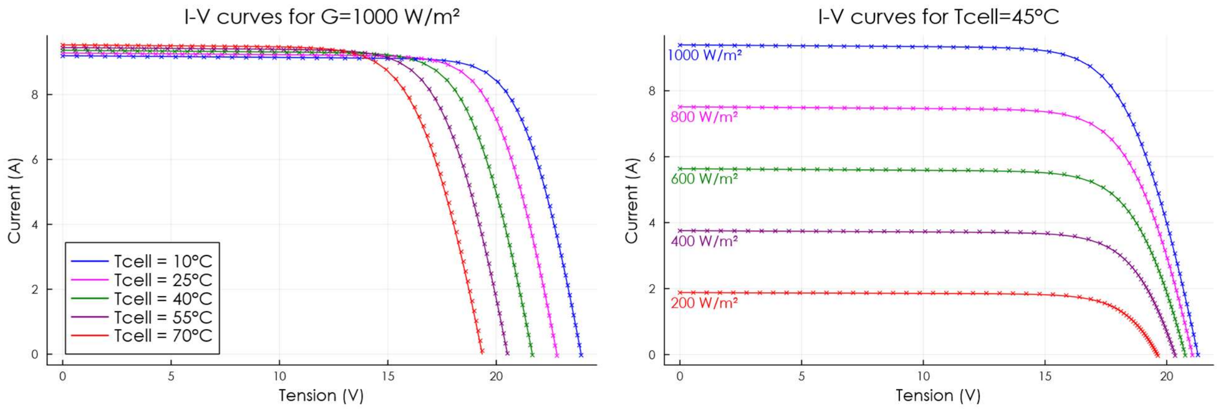

Figure 2.5 - Characteristic curves of the Poly160Wp36 Generic panel under different irradiance and cell temperature

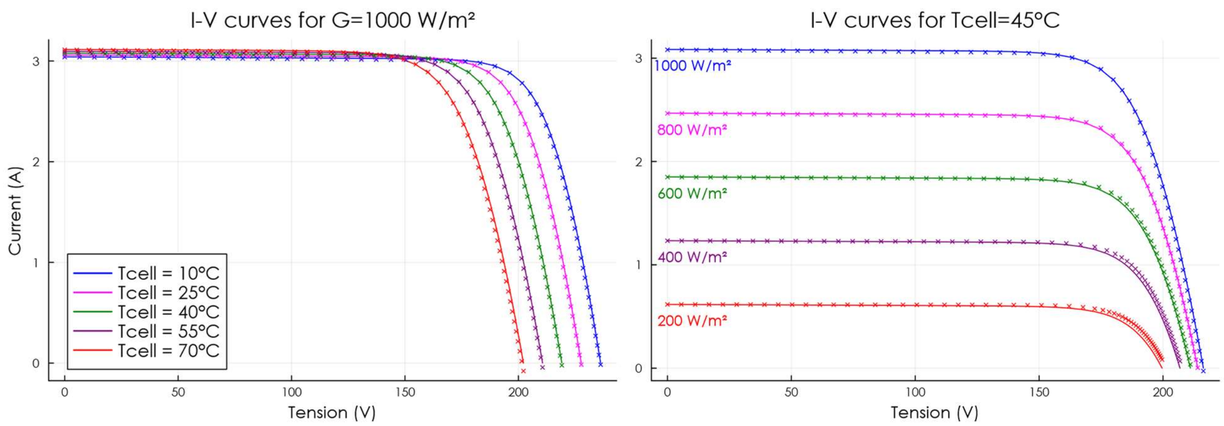

Figure 2.6 - Characteristic curves of the FS-7540A-FT1 panel under different irradiance and cell temperature

The simulated curves match well with the first two models from PVsyst (Figure 2.4 and Figure 2.5) but the model is less accurate for the last one (Figure 2.6). To quantify the accuracy of the proposed model, two performance indicators are used. The first one is the coefficient of determination R^2 which assesses the goodness of fit of the model and the second is the root mean square error (RMSE), which measures the overall error. They are defined as:

$$\begin{cases} R^2 = 1 - \dfrac{\sum_1^n (y_i - y_i^*)^2}{\sum_1^n (y_i - \bar{y})^2} \\ RMSE = \sqrt{\dfrac{1}{n} \sum_1^n (y_i - y_i^*)^2} \end{cases} \tag{2.13}$$

The results are presented in Table 2.1 for different irradiance and temperature conditions, the highlighted line is the result under STC. Overall, the RMSE values remain low and the R^2 values consistently exceed 0.997 for the crystalline technologies, indicating a very good agreement between the simulated and reference curves.

Table 2.1 comparison of the model vs PVsyst results

	LR7-72HGD-620M Bifacial		Poly160Wp36		FS-7540A-FT1	
Technology	Si – mono [Longi]		Si – poly [Generic]		CdTe [First Solar]	
G	RMSE [A]	R^2	RMSE [A]	R^2	RMSE [A]	R^2
1000 W/m^2	0.0449	0.9999	0.0323	0.9998	0.0258	0.9993
800 W/m^2	0.0498	0.9998	0.0178	0.9999	0.0073	0.9999
600 W/m^2	0.0576	0.9996	0.0120	0.9999	0.0245	0.9984
400 W/m^2	0.0615	0.9991	0.0147	0.9998	0.0411	0.9897
200 W/m^2	0. 0542	0.9971	0.0160	0.9993	0.0459	0.9480
T_{cell}	RMSE [A]	R^2	RMSE [A]	R^2	RMSE [A]	R^2
10°C	0.0491	0.9999	0.0394	0.9998	0.0297	0.9991
25°C	0.0397	0.9999	0.0293	0.9999	0.0245	0.9994
40°C	0.0404	0.9999	0.0292	0.9999	0.0243	0.9994
55°C	0.0642	0.9998	0.0449	0.9997	0.0315	0.9990
70°C	0.1183	0.9995	0.0798	0.9993	0.0464	0.9979

2.2.2 Maximum power output determination

2.2.2.1 Method

The value that will eventually need to be determined is the maximum power output of the PV panel. To calculate it at each timestep, three different approaches can be utilized:

- IV curve calculation: This method requires to solve the equation 2.1 for a predefined set of points and then use the resulting (I, V) pairs to determine (I_{mp}, V_{mp})
- Explicit model: Previously presented, this method is the simplest in terms of computational complexity.
- System resolution: Also introduced earlier, this approach offers the highest physical accuracy but requires solving a system of two equations at each timestep.

To evaluate the accuracy of each of those methods, two comparisons can be made: the first one against PVsyst model, and then a second one against measured data.

2.2.2.2 Comparison with PVsyst

The PV power output predicted by the different models can be compared against predicted data from PVsyst. Weather inputs are taken from PVsyst database and correspond to a typical meteorological year. The selected site is located in Australia (35.6675° South, 147.0387° East). As shown in Figure 2.7, all models exhibit a close match with PVsyst own model results.

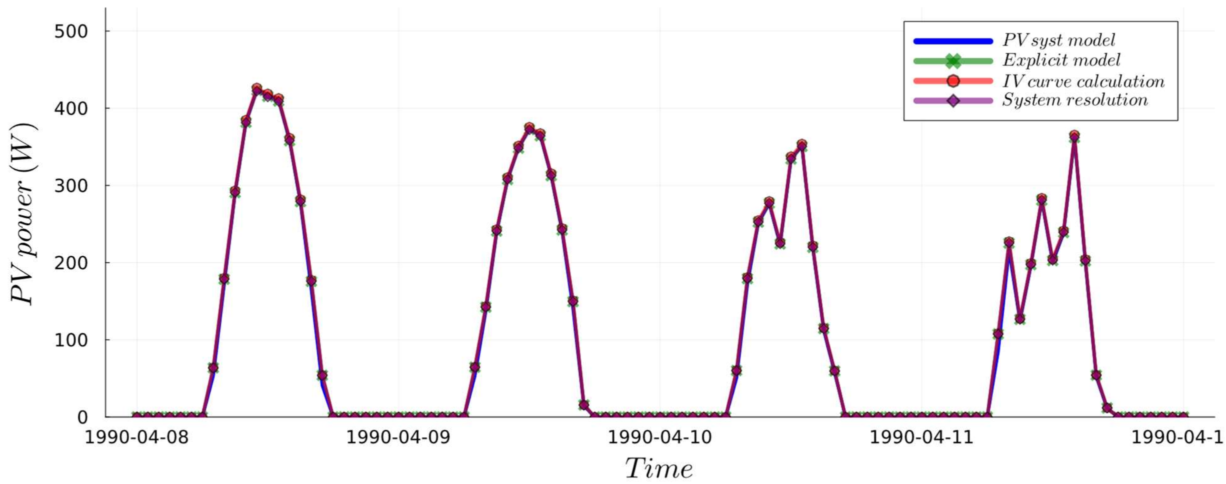

Figure 2.7 - Comparison between PVsyst and the proposed PV models

To quantify the accuracy of the three different methods, the same two performance indicators as previously can be used: RMSE and R^2. Additionally, the normalized mean average error (NMAE) can be calculated as defined in 2.14. The $\bar{y}$ here considered is the average PV production value of one solar panel, considering only the positive value.

$$NMAE = \frac{1}{n}\sum_{1}^{n}\frac{|y_i - y_i^*|}{\bar{y}} \tag{2.14}$$

Table 2.2 - PV power output model performance comparison with PVsyst model

	RMSE [W]	**NMAE [%]**	**R^2**
IV curve calculation	5.40	1.15 %	0.9989
Explicit model	4.85	0.88 %	0.9991
System resolution	4.78	0.87 %	0.9991

As expected, the system-resolution method has the highest accuracy. The explicit model, although being an approximation, achieves similarly low errors while being simpler to implement.

2.2.2.3 Application to measured data

To confirm the previously found results, the models can also be compared against measured data. The dataset used presents PV production data from an Australian solar farm situated in the region of Yulara (-25.242872, 130.98909). The PV panels used on this solar farm are the SPR-327NE-WHT-D PV panels. The dataset represents 5 years of data (between 2016 and 2021) and gives the power output of a 69 PV panels solar farm every half hour. It also gives the measured ambient temperature and the global horizontal irradiation (Desert Knowledge Australia Centre, 2016).

The figures below show that all three modeling approaches reproduce the measured power output with good overall agreement, although in summer the models tend to overestimate production while they underestimate it in winter.

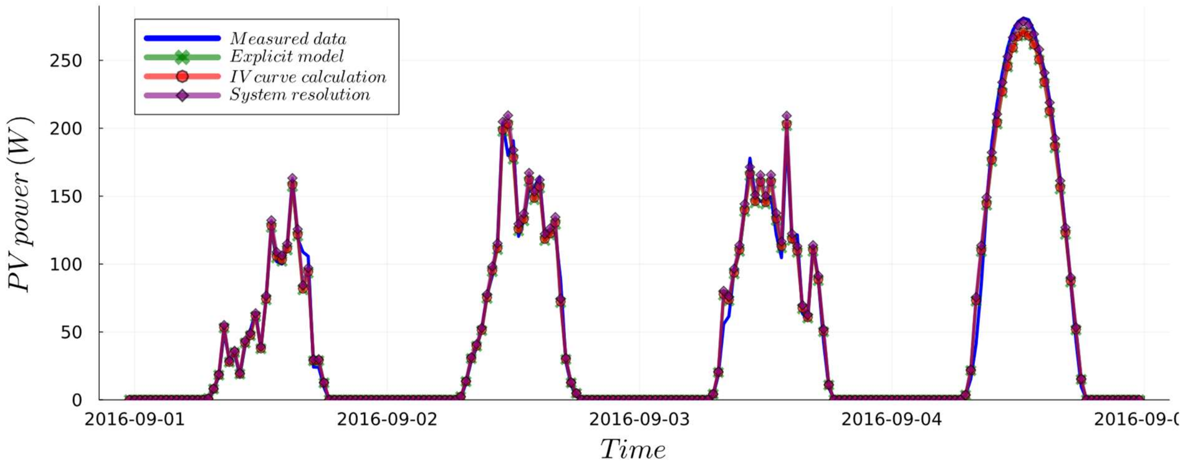

Figure 2.8 - Measured vs model PV power output - zoom in September 2016

As the degradation of the solar panels is not considered, the different performance indicators have been calculated for the first year of the data set and then the entire data set. The results are summarized in Table 2.3, using the same metrics as in last section.

Table 2.3-PV power output model performance comparison with measured data

		RMSE [W]	NMAE [%]	R^2
IV curve calculation				
1 year	300 pts	10.79	3.95 %	0.9872
	500 pts	10.79	3.95 %	0.9872
	10000 pts	10.79	3.95 %	0.9872
5 years	300 pts	12.19	4.54 %	0.9841
	500 pts	12.19	4.54 %	0.9841
	10000 pts	12.19	4.54 %	0.9841
Explicit model				
1 year		10.44	3.86%	0.9880
5 years		11.03	4.13%	0.9870
System resolution				
1 year		12.02	4.3%	0.9841
5 years		14.35	5.3%	0.9780

In this situation, we can see that the explicit model is both the easiest one to implement and the most accurate one. A mean average error of 5.49 W during the first year represents an error of 1.67 % compared to the maximum power output of the PV panel.

It is important to note here that in the measured data, for a given pair of irradiance (GHI) and ambient temperature (T_{amb}), the measured PV power output fluctuates over time, as illustrated on Figure 2.9 above (it is especially visible on the right side). As a result, the errors observed between measured and modeled power outputs are not solely attributable to the limitations of the PV models themselves but also to additional factors such as wind speed and the aging of PV modules for example. Because of this, the reported error should be interpreted as a combination of model approximation error and variability in the measured data.

In the next chapter, the PV model considered will be the explicit one, not because of its better results but because of its greater simplicity.

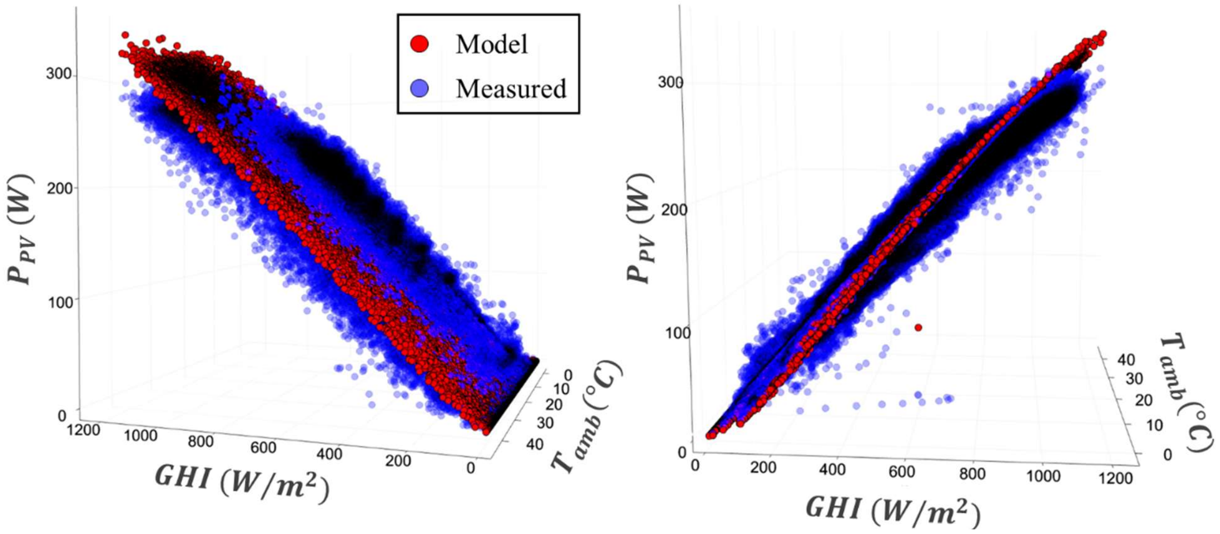

Figure 2.9 - Measured vs modeled PV power output

2.3 Minute-resolution downscaling algorithm for irradiance

Solar production forecasts are typically made on an hourly basis, which masks the intra-hour variability that can occur. (Omoyele et al., 2024). However, those variations are important to model in the context of battery management, where high fluctuation in solar production can lead to high charging currents and will increase the number of cycles that the batteries go through each day.

The idea is therefore to interpolate hourly data to 1-min one to get a PV production model more detailed.

2.3.1 1h vs 1min production comparison

To highlight the limitations of hourly solar forecasts, GHI measurements with different temporal resolutions are compared using data from Wilcox & Andreas (2010). Figure 2.10 illustrates 1-minute GHI measurements, along with their corresponding 15-minute and 60-minute averages

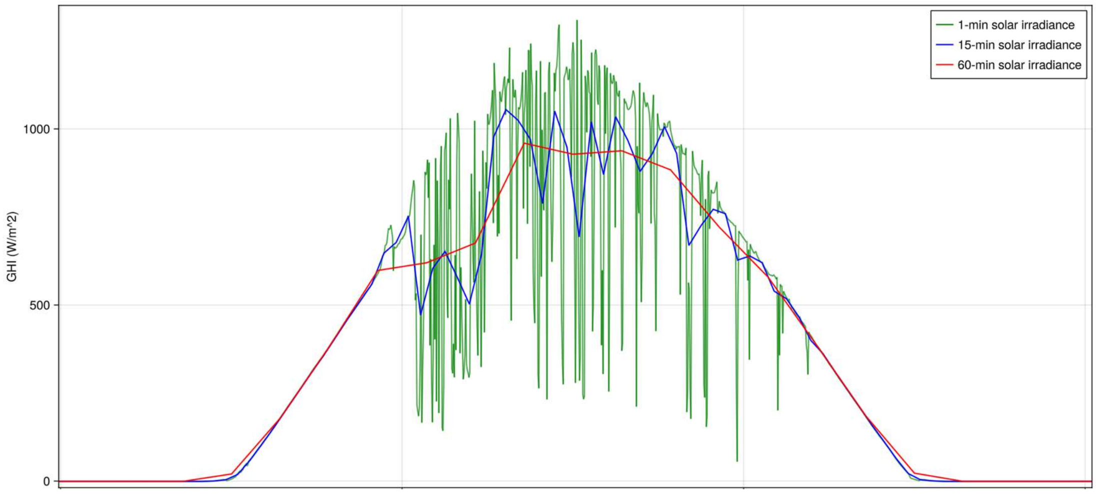

Figure 2.10 - Comparison between 1-minute GHI data and its 15-minute and 60-minute averages on May, 20th, 2013, data from (Wilcox & Andreas, 2010)

As shown on the figure, the 1-minute resolution reveals fluctuations in irradiance caused by changing weather. These variations are completely smoothed out in the hourly profile, which only captures the average trend.

To better analyze the differences between the three curves and the impact on the number of cycles completed by the battery, we consider a scenario that will be developed in Chapter 4 and that is illustrated in Figure 2.11 below. The goal here is to smooth the PV production throughout the day.

The number of cycles completed by the battery on a day will be proportional to the quantity evaluated in Eq. 2.5, named here “Cycle factor” (it is represented as the colored area in the figure below which illustrates when the battery needs to charge/discharge).

$$CF = \int \left| P_{PV} - P_{obj} \right| dt \tag{2.15}$$

This metric is useful to highlight how much short-term fluctuation information is lost when considering average data

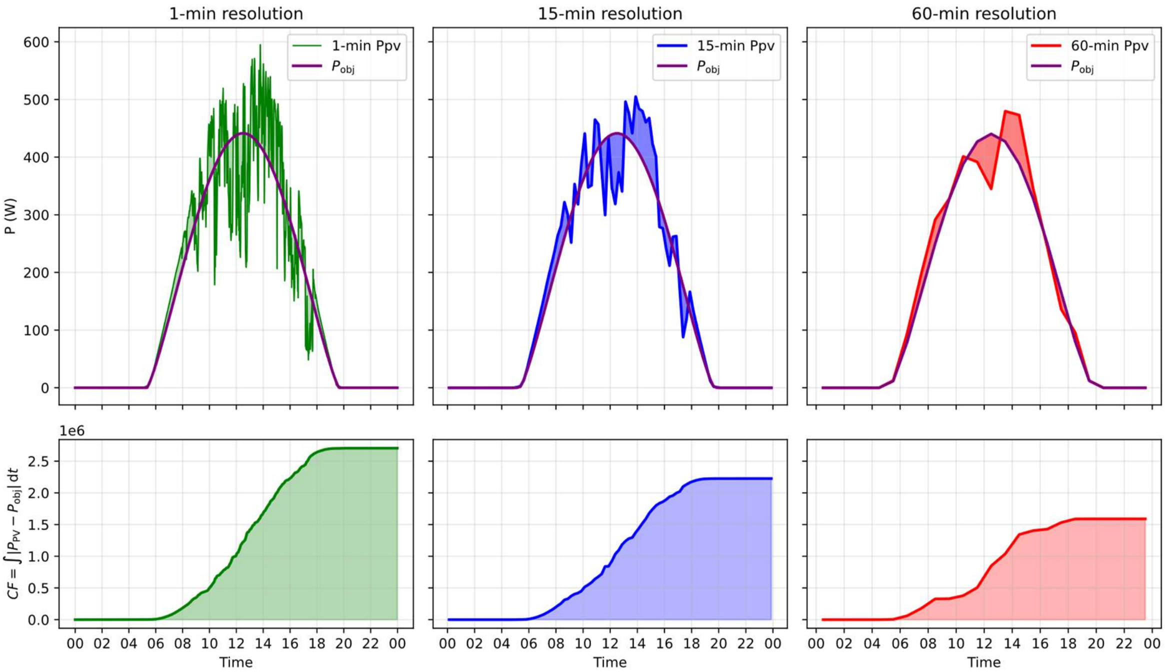

Figure 2.11 - Influence of temporal resolution on battery cycling demand

Using averaged data would therefore result in an important underestimation of the cycle completed by the battery through its lifetime, which justifies the need for a downscaling method.

Table 2.4 - Comparison between 1-minute data statistics and its 15-minute and 60-minute averages over a year

Metrics	1-min data	15-min data	60-min data
Maximum GHI [W/m^2]	1311.34	1056.41	960.96
CF [Wh]	546275	493310	450466
Cycle factor reduction compared to 1min data	[redacted]	-9.69%	-17.54%

Because PV power output is directly linked to solar irradiance, it exhibits the same short-term variability. If irradiance data are excessively averaged, peak values are reduced, which masks clipping events These clipping events come from the inverters, which are typically sized below the PV array peak power, often around 80 % of the nominal PV capacity, to operate closer to their optimal efficiency range. This can lead to underestimated peak power and an overestimation of annual PV energy production.

On Figure 2.12, the PV model presented in section 2.1.2.2 was applied to outline the variability of PV production on a 1min basis compared to an hourly one. For the day shown, only the 1-minute time series captures the clipping phenomena, which disappears in the hourly representation.

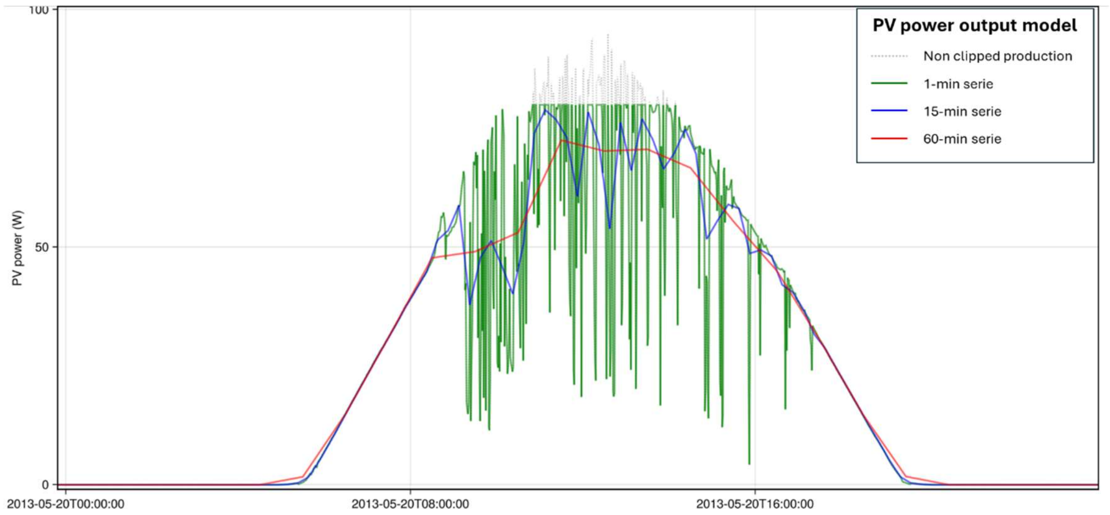

Figure 2.12 - Comparison between 1-minute, 15-minute and 60-minute averages PV production prediction

Overall, the yearly difference in production between the different samples is low (0.3 %), as presented in Table 2.5.

Table 2.5 – Total yearly PV production for different time steps resolution

1-min data	15-min data	60-min data
147.2 MWh	147.5 MWh	147. 7 MWh

However, someday, the difference can be higher. On the dataset considered, the maximum difference is obtained on the 8th of May, where the prediction on an hourly basis is 4 % higher than the one on a minute basis.

In conclusion, the need for a downscaling algorithm is here motivated by the battery management need and not the accurate PV production estimation. Indeed, considering hourly data instead of minute one has little impact on the final yearly PV production calculation whereas it could underestimate the number of battery cycles by more than 15 %.

2.3.2 Mathematical framework for downscaling

In their review, Omoyele et al. (2024) categorize five main methodological approaches for downscaling hourly solar irradiance data to 1-minute resolution:

- Deterministic methods, such as linear and cubic interpolation. These are computationally inexpensive solutions but often fail to capture intra-hour variability accurately.
- Stochastic methods introduce random variability by fitting statistical distributions.
- Markov chain models rely on the probabilistic transitions between classified sky conditions (via the clearness index) and are particularly useful for capturing temporal dependencies.
- Non-dimensional approaches use historical databases to reconstruct minute-level profiles.
- Machine learning techniques capture non-linear patterns effectively but require larger datasets and higher computational resources.

2.3.2.1 Mathematical model

A Markov chain model is a mathematical framework used to represent the dependence between successive observations in a time series, where the current state depends only on a limited number of preceding states. The model's order indicates how many past states are taken into account when predicting the next one, with higher-order models capturing more complex temporal dependencies. (Omoyele et al., 2024)

A Markov process $(X_t, t = 0,1,2 \ldots)$ with a set of m allowed states $(m_1, m_2, m_3 \ldots)$ is said to be in state j at time t if $X_t = j$. In a first order Markov model, the probability that it will be in state j at time t given it was in state i at $t-1$ is calculated using a fixed probability P_{ij} written mathematically as:

$$P_{ij} = (X_t = j | X_{t-1} = i) \quad 2.16$$

P_{ij} is known as the transition probability from state i to j and is dependent only from the state at $t-1.$ Given a set of observations, the transition probability from state i to state j can be estimated by dividing the number of times the sequence i to j occurs by the total number of occurrences of state i. This method provides a data-driven way to construct the Markov transition matrix, which captures the probabilistic behavior of the system. In the context of this work, this approach will be used to model the temporal evolution of the clearness index k_t, which reflects the cloudiness conditions affecting solar irradiance. By learning the transition dynamics of the clearness index from historical data, the model will be able to downscale hourly data to 1-min one.

A Markov chain model is presented in Hoffmann et al. (2014) and is applied to historical 1min clearness data to then generate 1-minute global irradiance time series from hourly averages.

2.3.2.2 Clearness index determination

The first step is to reconstruct the clearness index k_t from the historical GHI data. In this work, it is approximated using a simple formulation as presented in Eq 2.17. However more complex models such as the one from PVlib (F. Holmgren et al., 2018) or the ASHRAE (ASHRAE, 2025) also exists. These models consider atmospheric turbidity or air mass, which are here ignored.

$$k_t = \frac{G_{measured}}{G_{clear}} \qquad 2.17$$
$$G_{clear} = G_{ext} * \sin(\alpha)$$

Where $G_{measured}$ is the measured global irradiance at Earth's surface (GHI), G_{clear} is the irradiance calculated for the cloudless conditions, G_{ext} is the extraterrestrial irradiance and α is the elevation of the sun. The extraterrestrial irradiance can be calculated using the expression presented below. (Duffie & Beckman, 2013)

$$G_{ext} = G_{sc} * \left(1 + 0.033 * \cos\left(\frac{360}{365} * n\right)\right) \qquad 2.18$$

Where G_{sc} is the solar constant, with $G_{sc} = 1367\ W/m^2$.

The data presented in Figure 2.13 were obtained from the NASA Langley Research Center (LaRC) POWER Project funded through the NASA Earth Science/Applied Science Program. (Zhang et al., 2024)

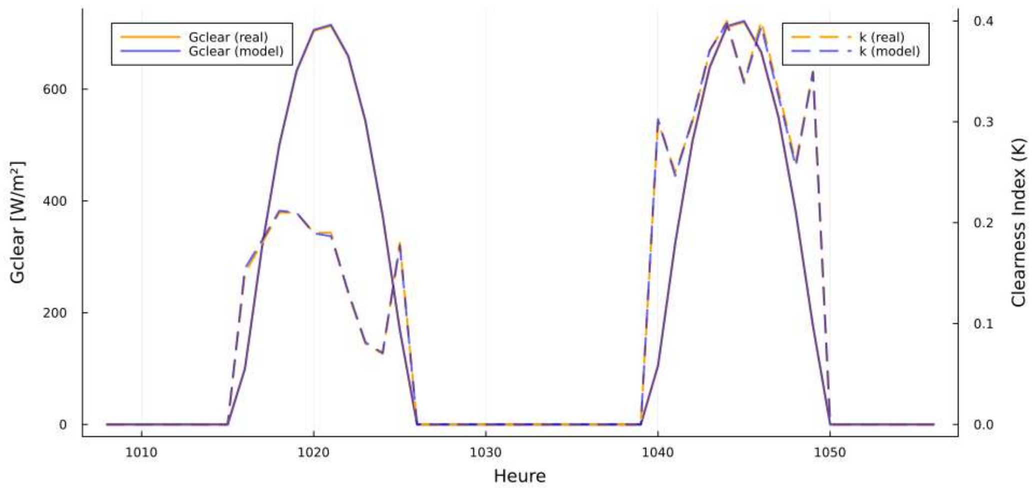

Figure 2.13 - Cloudless irradiance and clearness index comparison (model vs measured data from (NASA, 2025))

Overall, the model demonstrates excellent performance on the dataset as presented in Table 2.6.

Table 2.6 – External irradiance and clearness index model result

Data	R^2	RMSE
G_{clear}	1.000	1.013 W/m^2
k_t	0.9998	0.0018

On a clear day, the real maximum real value of k_t will be around 0.85 in the considered locations (Europe in (Hofmann et al., 2014) and North America in this work). In Hoffmann et al. (2014) model, k_t is divided by 0.78 to get a normalized value of it. The acceptable values of k are thus comprised between 0 and 2.

In the following section, k_t will refer to this normalized value with:

$$k_t = \frac{G_{measured}}{G_{clear}} * \frac{1}{0.78} \tag{2.19}$$

2.3.2.3 Data generation

To ensure that the data is not biased by any specific location, four datasets from diverse geographical sites have been aggregated, resulting in a total of nine years of distinct measurements. The data, originally published by Wilcox & Andreas (2010) were collected at the following locations and during the corresponding time periods:

1. ARM Radiometer Characterization System (RCS), data available from June 24, 2003 to June 25, 2004 [36.606° North, 97.486° West]
2. SOLRMAP Kalaeloa Oahu (RSR) data available from October 31, 2010 to October 31, 2011 [21.31347° North, 158.08257° West]
3. SOLRMAP Utah Geological Survey - State Energy Program (Milford), data available from September 18, 2012 to September 16, 2013 [38.41431° North, 113.02967° West]
4. Oak Ridge National Laboratory (RSR), data available from January 1st, 2015 to December 31st, 2016 [35.92996° North, 84.30952° West]
5. University of Oregon (SRML), data available from September 1, 2024 to May 27, 2025 [44.0467° North, 123.0743° West]

Using the model presented in the previous part, k_t value can be calculated at each time step.

The model is then constructed in three steps:

1. Categorize each day into one of the three possible weather conditions: cloudless, broken clouds and overcast. The weather conditions are determined by the calculation of the hourly clearness index
2. Process and transform 1-minute measurement datasets into transition probability matrices for each possible weather
3. Generate synthetic sequences for each hourly $\boldsymbol{k_t}$ through Markov chain to recreate 1-min series.

The predominant weather conditions on each day is based on the daily average $\overline{k_{day}}$ value and its variability $\widetilde{k_{day}}$ on that given day, expressed as:

$$\begin{cases} \overline{k_{day}} = \frac{1}{n}\sum k_t \\ \widetilde{k_{day}} = \frac{1}{n}\sum |k_t - k_{t-1}| \end{cases} \quad 2.20$$

Around sunrise and sunset, average GHI values are low, meaning that even small errors can significantly affect the calculated clearness index, resulting in high apparent variability for those hours. To eliminate these, we only consider hours where both GHI and G_{clear} exceed 10 W/m². n is the number of hours that respects this condition.

Table 2.7- Overview of the three weather classification

Weather class	Condition
Overcast	$0.6 - \overline{k_{day}} > \widetilde{k_{day}}$
Cloudless	$-0.72 + 0.8 * \overline{k_{day}} \geq \widetilde{k_{day}}$
Broken clouds	$Otherwise$

To better understand the classification rules presented in

Table 2.7, we can plot each day's conditions as a single point distributed according to its daily mean $\overline{k_{day}}$ and its daily variability $\widetilde{k_{day}}$. The result is presented on Figure 2.14.

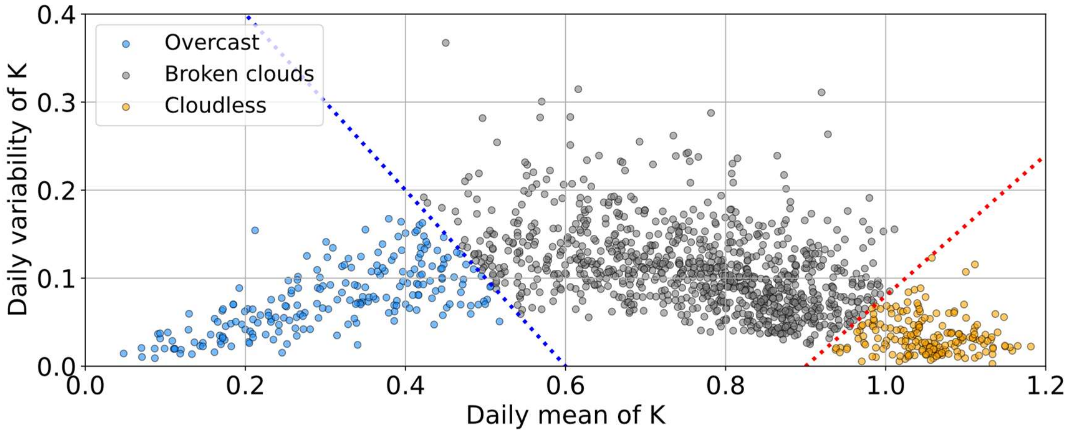

Figure 2.14 - Weather classification, data from (Wilcox & Andreas, 2010)

In Figure 2.15, four days are shown with different irradiance patterns and corresponding k_t profiles, which shows the difference between overcast, broken cloud, and cloudless conditions. Clear-sky days are characterized by a stable k_t near 1, overcast days exhibit lower k_t, and broken cloud days show high fluctuations.

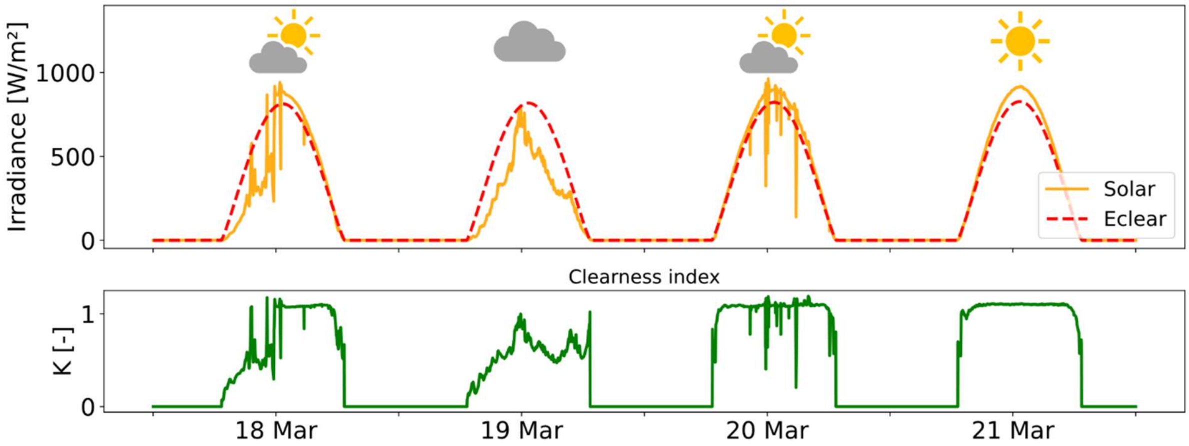

Figure 2.15 - Example of weather categorization, data from (Wilcox & Andreas, 2010)

As we can see, k_t behavior varies significantly between each weather category. This separation is reflected on Figure 2.16, which represents the distribution of k_t values for each weather conditions. By dividing the weather into those three classes, three normal distributions are found.

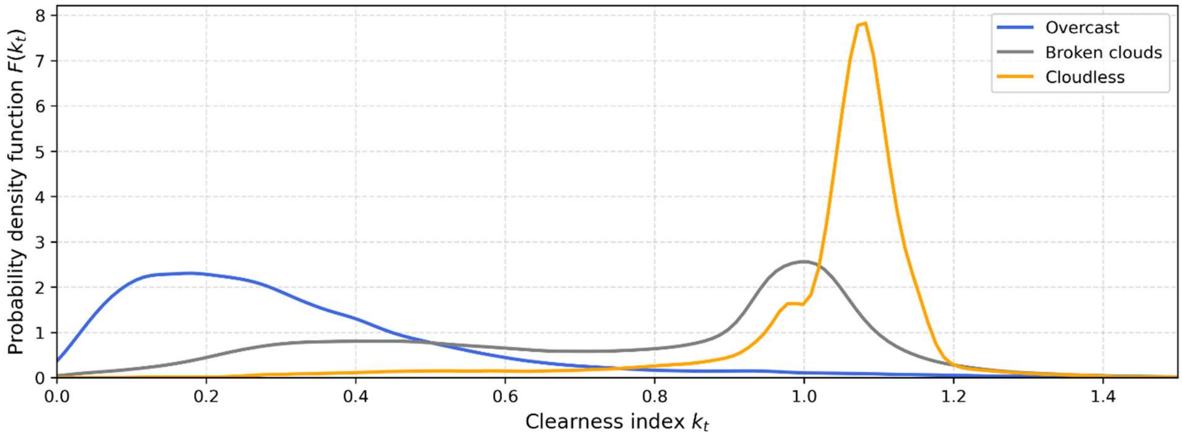

Figure 2.16 - Clearness index probability density function for different weather classification, data from (Wilcox & Andreas, 2010)

2.3.2.4 Transition matrix generation

The next step is to construct a transition probability matrix (TPM) for each weather class, to represent the likelihood of changes in the clearness index k_t over time. These matrices describe how likely it is for a given k_t value at time t to transition to another value at time t + 1. To build the TPMs, profiles of measured one-minute k_t values are analyzed and the resulting frequency distributions are normalized to form probability matrices. Each TPM therefore represents the minute-by-minute evolution of k_t under a specific weather condition.

Table 2.8 highlights the most probable transitions (in green), showing a strong diagonal dominance. This indicates that the clearness index tends to remain stable from one minute to the next.

Table 2.8 - Excerpt of the TPM, computed for overcast weather

$k_{t,i}$ \ $k_{t,i+1}$	0.0	0.01	0.02	0.03	0.04	0.05	…
0.0	0%	0%	0%	0%	0%	0%	
0.01	0%	76%	17%	3%	1%	1%	
0.02	0%	12%	67%	17%	2%	1%	
0.03	0%	2%	13%	64%	19%	1%	
0.04	0%	0%	1%	15%	61%	19%	
0.05	0%	0%	0%	1%	14%	62%	
…							

To highlight the overall dynamics of k_t behavior, all the TPM can be visualized in the form of heatmap for each type of weather.

- **Clear sky:** The heatmap shows a pronounced line along the diagonal centered at $k_t{\sim}1$. This indicates that when the sky is clear, the clearness index tends to stay close to 1 from one minute to the next.
- **Broken clouds:** Two distinct clusters emerge. One is around $k_t{\sim}0.2$, corresponding to a cloud covered sky, and another near $k_t{\sim}1$, when the sun breaks through. This pattern reflects switches between clear and clouded conditions.
- **Overcast:** The high probability values concentrate around low k_t, with most transitions occurring below $k_t{\sim}0.3$.

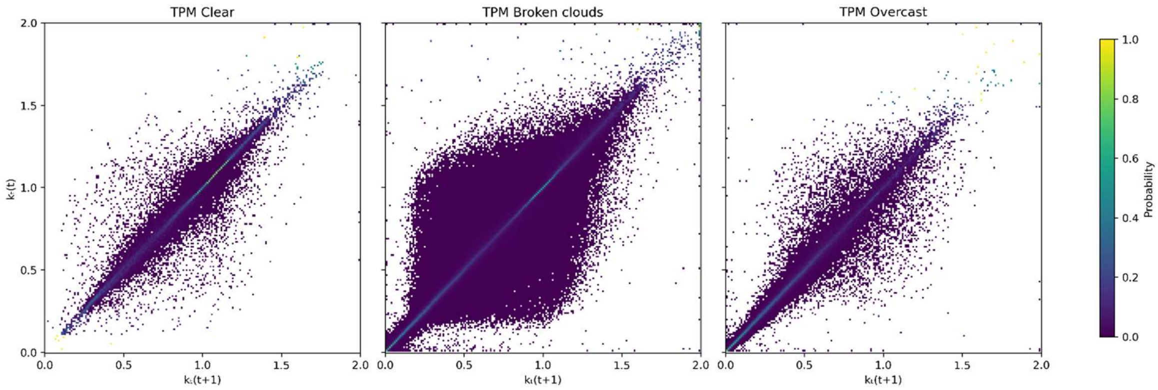

Figure 2.17 - TPM for the three different weather classes

2.3.2.1 1min data generation through Markov Chains

The purpose of the method is to generate a realistic set of 60 one-minute clearness index values from a given hourly average through a Markov process.

At each step, a random number between 0 and 1 is drawn. Based on the TPM corresponding to the correct weather condition, the row associated with the current k_t value is selected. This row represents the probabilities of transitioning to each possible k_{t+1}.The probabilities are accumulated into a cumulative distribution, and the next clearness index value is determined by finding the first bin where the cumulative probability exceeds the random number. This process is repeated 60 times to build a full 1-hour sequence.

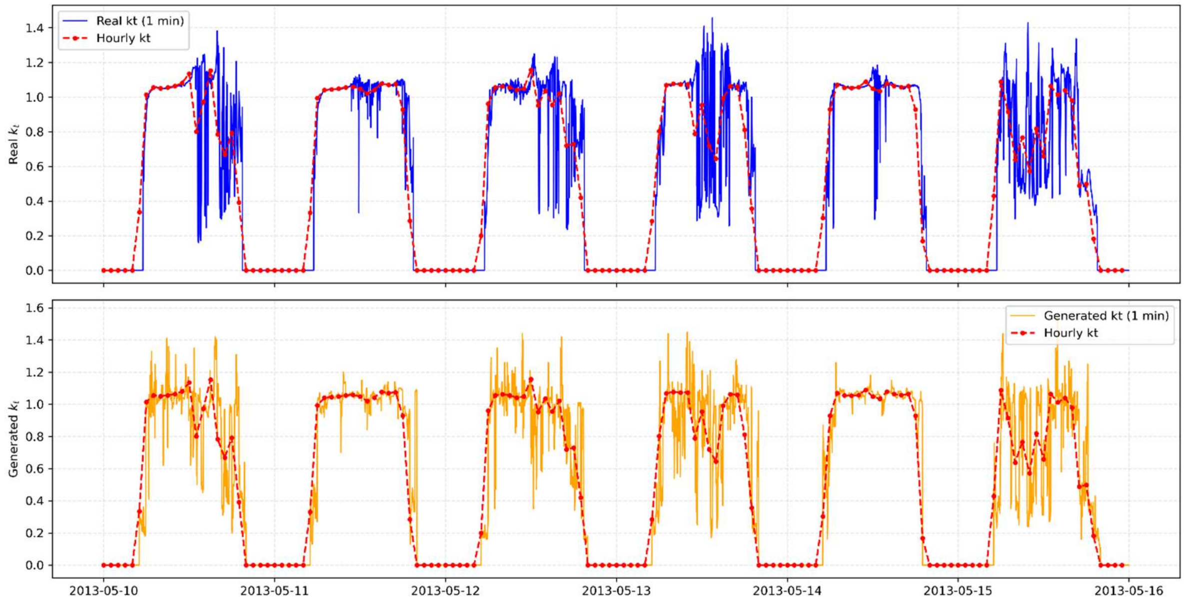

Figure 2.18 - Generated vs measured kt overtime, data from (Wilcox & Andreas, 2010)

If the mean of the generated 1-minute values does not match the original hourly average k_t within a specified tolerance (0.01 in Figure 2.18), the sequence is discarded and regenerated. The loop continues until the generated sequence is statistically consistent with the hourly input.

2.3.3 Results

2.3.3.1 Statistical validation

The aim of the 1min data generation is not to replicate the exact value of the initial sequence but rather to recreate a synthetic signal that preserves the statistical characteristics of the measured data. A first verification consists in comparing the probability distributions of the measured and generated series. As presented in Figure 2.19, the two distributions exhibit a very similar shape.

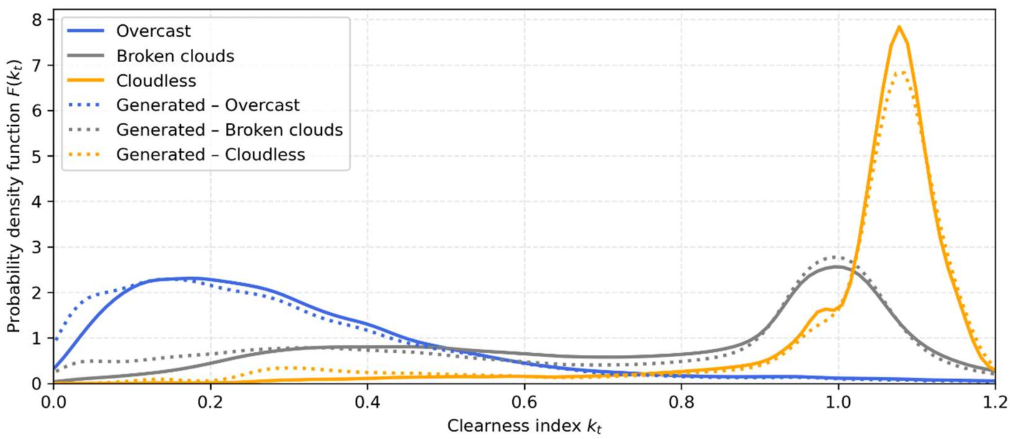

Figure 2.19 - PDF comparison between measured and generated 1min-data

In addition to the mean and the standard deviation, we can compare the Kurtosis coefficient proposed in (Forbes et al., 2010). It quantifies the variability of the distribution. High kurtosis (positive) suggests values tightly clustered around the mean with frequent extreme events, while low kurtosis (negative) implies a flatter, more uniform distribution. When the kurtosis is consistent between measured and generated data, it means the distribution of the data is well reflected. The results are presented in Table 2.9.

Table 2.9 - 1min generated data accurateness analysis

Statistic	Measured kt	Generated kt
Mean μ	0.3619	0.3653
Standard deviation σ	0.4385	0.4369
Kurtosis coefficient	-1.2424	-1.2437

These results confirm the strong similarity between the two distributions. The nearly identical mean and standard deviation indicate that the global statistical structure is well preserved. Moreover, the kurtosis coefficients values suggest that the generator realistically reproduces the level of intra-hour variability and the likelihood of extreme k_t values. However, we can see that the values during clear days are not concentrated enough, while the opposite happens for broken clouds day. This is an issue in the context of battery management, as the level of fluctuation that occurs daily has a direct impact on the numbers of cycles completed.

2.3.4 Model improvement

2.3.4.1 Variability

To further improve the model, we can refine how variability is captured when generating each 60-point time series. Until now, we've only ensured that the synthetic series is centered on the hourly mean of the clearness index k_t, but an additional criterion could be to fix its variability as well.

To do this, we must first verify the relationship between the hourly k_t and its intra-hour fluctuations Δk_t. In Eq. 2.21, $k_i$refers to minute values as Δk_t represents the intra-hourly variation.

$$\Delta k_t = \frac{1}{60}\sum |k_i - k_{i-1}| \qquad 2.21$$

Figure 2.20 shows the conditional probability P($\Delta k_t | k_t$): on the horizontal axis is the hourly k_t , and on the vertical axis the possible intra-hour fluctuation Δk_tEach colored "pixel" gives the likelihood of observing a particular Δk_t. once you know k_t. What is particularly interesting is that k_t values around 1 statistically have a very low variability. This is observed for k_t values below 0.4 as well.

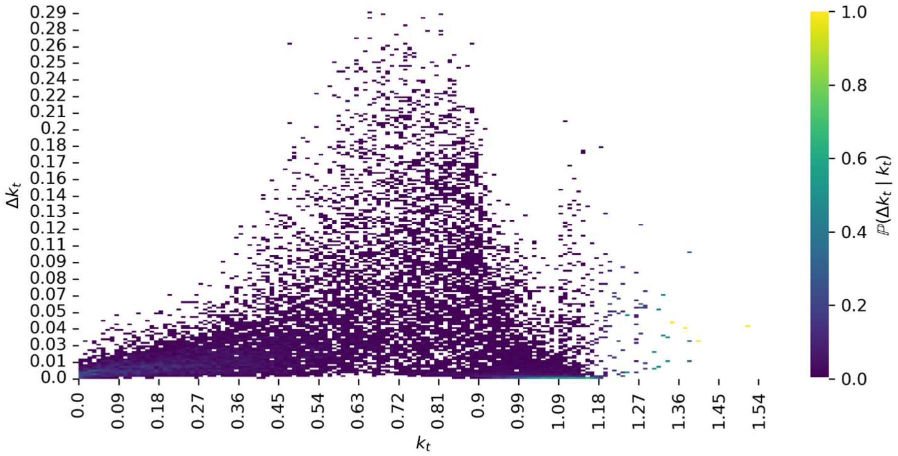

Figure 2.20 - Probability P(Δk|kt)

To generate 1min-series from the hourly average data additional step can be considered:

1. Find the relevant column in the heatmap.
2. Draw a uniform random number u ∈ [0,1].
3. Use this random number to select a Δk_t value according to the conditional distribution for that k_t.

By sampling Δk_t in this way, each synthetic 60-point series will not only be centered on the correct hourly average but should also reproduce the observed variability pattern.

To evaluate the accuracy of the generated series we introduce a score defined as:

$$score = |\mu_{generated} - k_t| + |\Delta_{generated} - \Delta k_{target}| \qquad 2.22$$

Where:

- $\mu_{generated}$ is the mean of the generated 1min series
- k_t is the observed hourly mean
- $\Delta_{generated}$ is the average variability of the generated 1min series
- Δk_{target} is the desired variability

By summing these two absolute errors, the score penalizes deviations in both mean and variability equally. A lower score therefore means the sequence more faithfully matches the target average and the target variability. The new algorithm can now be summarized with the flow chart presented in Figure 2.21.

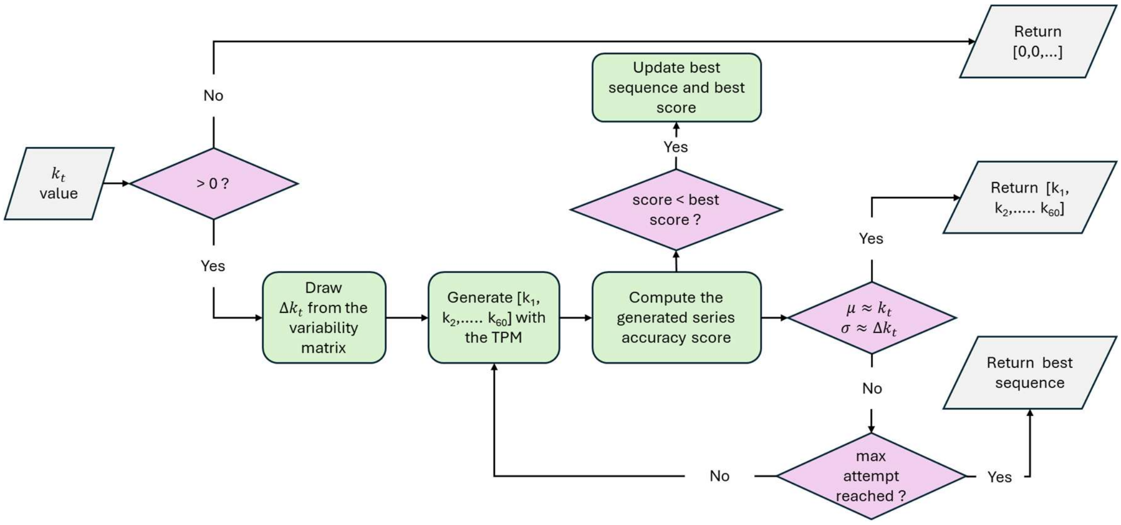

Figure 2.21 - 1min generated data algorithm flow chart

Overall, we can see that the distribution of the newly generated data follows more closely the measured one, as presented in Figure 2.22. In particular, the periods where k_t is close to 1 show less variability, which gives a better representation of reality. This indicates that the model successfully reproduces smoother irradiance patterns associated with stable, clear-sky conditions.

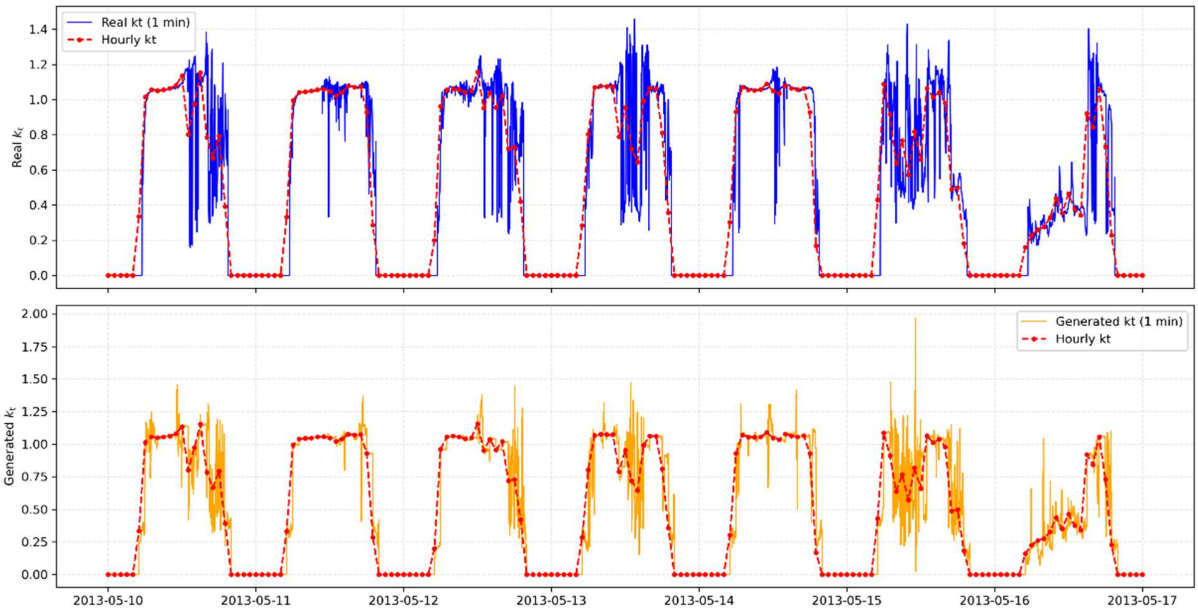

Figure 2.22 - Generated vs measured k_t overtime, data from (Wilcox & Andreas, 2010)

Overall, the distribution of k_t is better reflected with this new method (Figure 2.23)

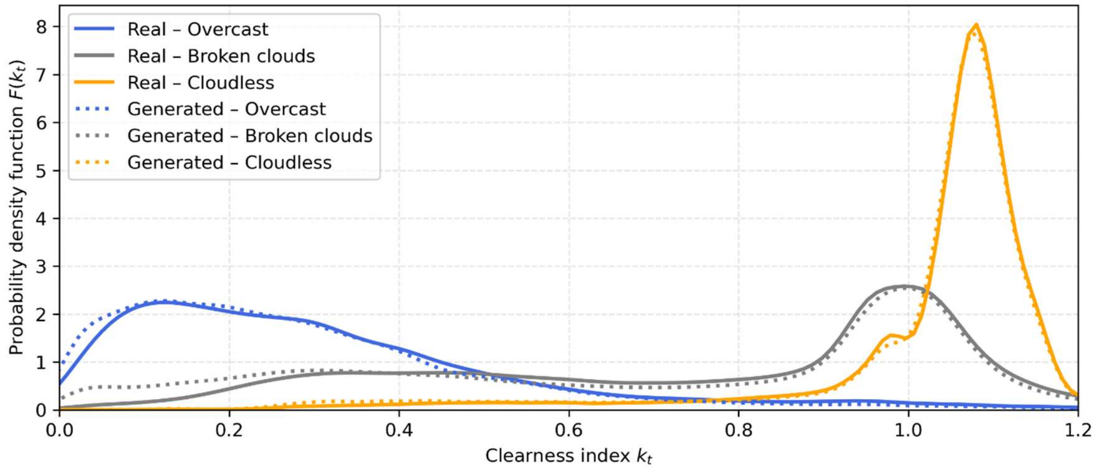

Figure 2.23 - PDF comparison between measured and generated data with the improved method

2.3.4.1 Geographical accuracy

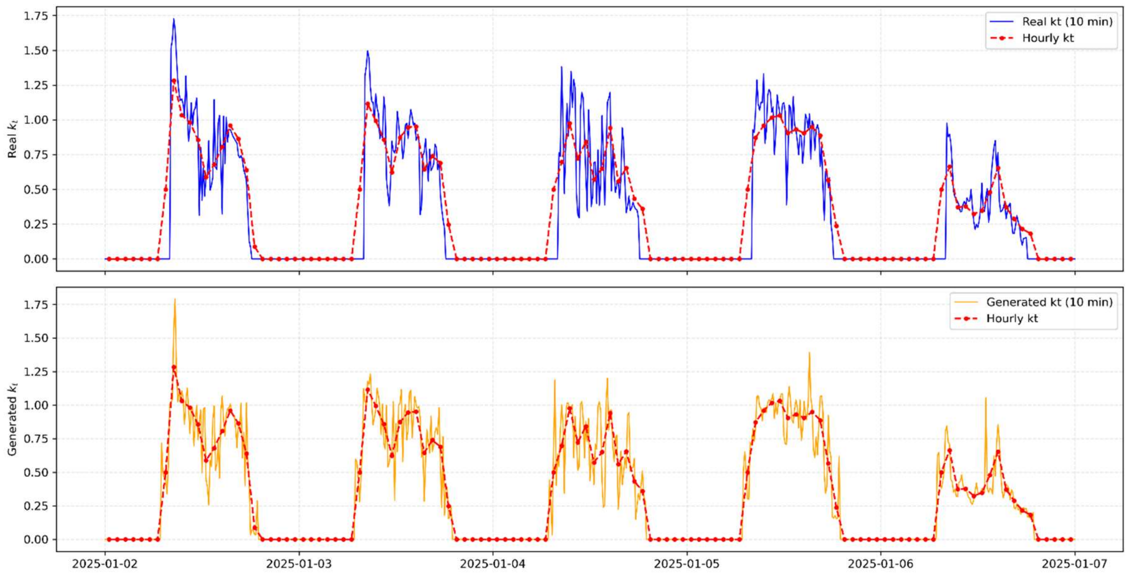

Figure 2.24 - Measured versus generated k_t value, data from (Equans, 2025)

To evaluate the robustness and generalizability of the downscaling process, it is essential to test its performance on data from a different geographic location than the one used for calibration. In this context, we applied the TPMs to a new dataset provided by Equans, originating from a solar farm located in the Dominican Republic. The dataset contains measured GHI, GTI and PV production values, recorded every 10 minutes over the month of January, 2025. (Equans, 2025)

The results of this comparison are shown in Figure 2.24, where the measured and generated kt series are plotted against the corresponding hourly values. As illustrated, the method demonstrates a good ability to reproduce intra-hour variability despite differences in location. In addition to good visual agreement between measured and generated series, statistical indicators are satisfying as well, the numerical results are presented in Table 2.10.

Table 2.10 – Downscaling process acurateness analysis on (Equans, 2025) data

Statistic	Measured kt	Generated kt
Mean μ	0.3582	0.3582
Standard deviation σ	0.4026	0.4188
Kurtosis	-1.5764	-1.5803

2.3.4.2 Application to solar data

The original goal of this section was to generate 1-minute PV data based on their hourly value to better reflect the stress the batteries will be under. Two different scenarios are presented below: the first one is when no PV data are provided, therefore they need to be generated directly using the 1-minute downscaled weather data, the second scenario is when hourly PV production data have been given and they now need to be downscaled as well.

PV model

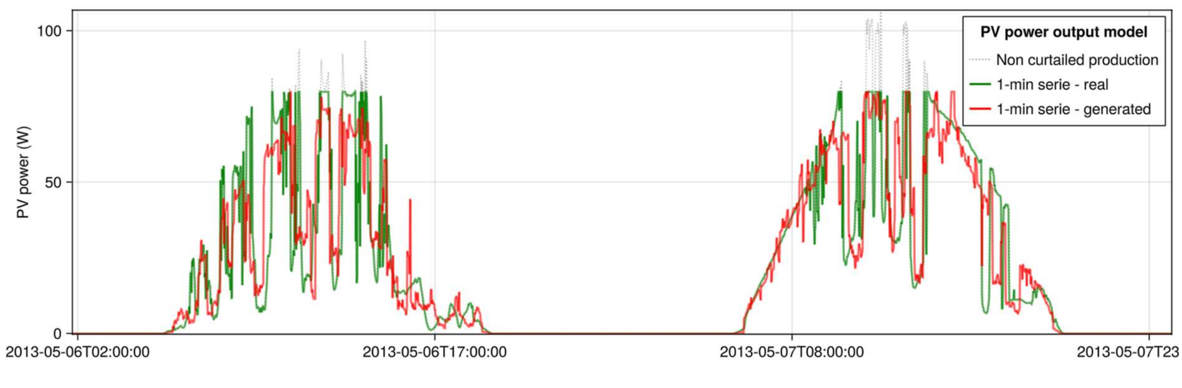

Figure 2.25 - 1min PV production generated data

The dataset used to create the TPM has been used here. Figure 2.25 has been produced using the PV model presented in section 2.1.2.2. The green line represents the PV production at 1-minute resolution, based on actual measured solar irradiance, while the red line corresponds to the series generated using the proposed model of data downscale. Overall, when summed over an entire year, the difference between measured and generated 1-minute PV energy is 0.3 %.

Measured data or PVsyst data

PV production depends on two main factors as seen in section 2.1.2.2: the GTI it receives and the temperature. Since 1-minute GTI measurements are not available, the approach adopted here consists of proportionally scaling the hourly PV production data, given by PVsyst or measured one, using the ratio between the measured global horizontal irradiance GHI_{hour} and the modeled 1-minute global horizontal irradiance GHI_{minute}:

$$PV_{min} = PV_{hour} * \frac{GHI_{minute}}{GHI_{hour}} \qquad 2.23$$

The same dataset from (Equans, 2025) has been used here. Overall, in a month, the difference between the measured PV production data and the 1-min one generated is 0.8 %. To reduce this difference to zero, an additional step could be to recenter the PV production value around their desired mean.

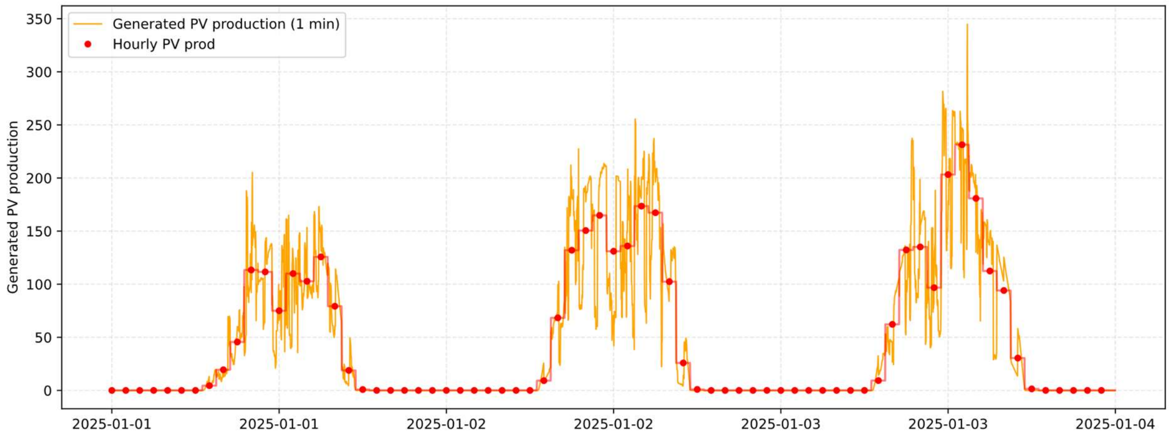

Figure 2.26 - Generated 1min PV production data from (Equans, 2025)

Additionally, it is important to note that the higher error rate obtained here is also due to the smaller dataset size (one month only compared to several years for the one from last part)

2.4 Conclusion

This chapter focused on the modeling of PV production with particular attention to the impact of temporal resolution. Such variations are essential to consider in BMS studies, as they directly influence charging power and cycling behavior in PV-coupled battery systems. A PV production model was developed and validated through comparison with PVsyst as well as measured data.

The main contribution of this chapter is the development of a minute-resolution method to downscale irradiance and PV production data. A stochastic model based on a Markov process, using the clearness index and daily weather classification, was reproduced from the literature and then improved to better capture irradiance variability, leading to a more realistic representation of its fluctuations.

Finally, the downscaling algorithm was validated in two ways (Figure 2.27). In the first approach, measured GHI data were downscaled then converted into PV production using the proposed PV model. The resulting minute-resolution PV production was then compared with PV production obtained by applying the same PV model directly to measured 1-minute GHI data, allowing the impact of the downscaling procedure to be isolated from the PV conversion model. This comparison resulted in a yearly difference of 0.3 %. In the second approach, the validation relied directly on measured PV production data. GHI data were downscaled and converted into PV production, which was then compared against measured PV output, leading to a difference of 0.8 %. This second validation step confirms that the proposed downscaling methodology preserves annual energy consistency, providing realistic results.

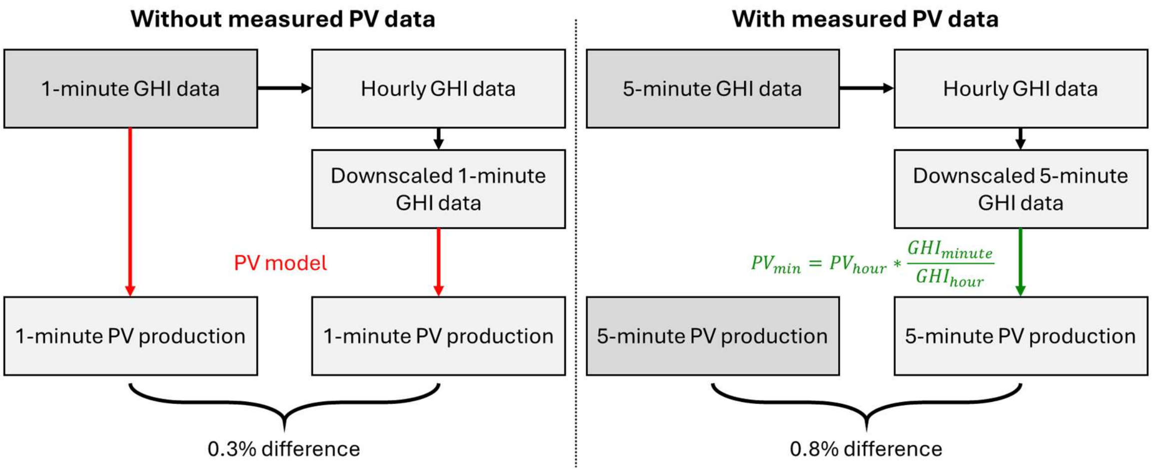

Figure 2.27 – Downscaling validation methods

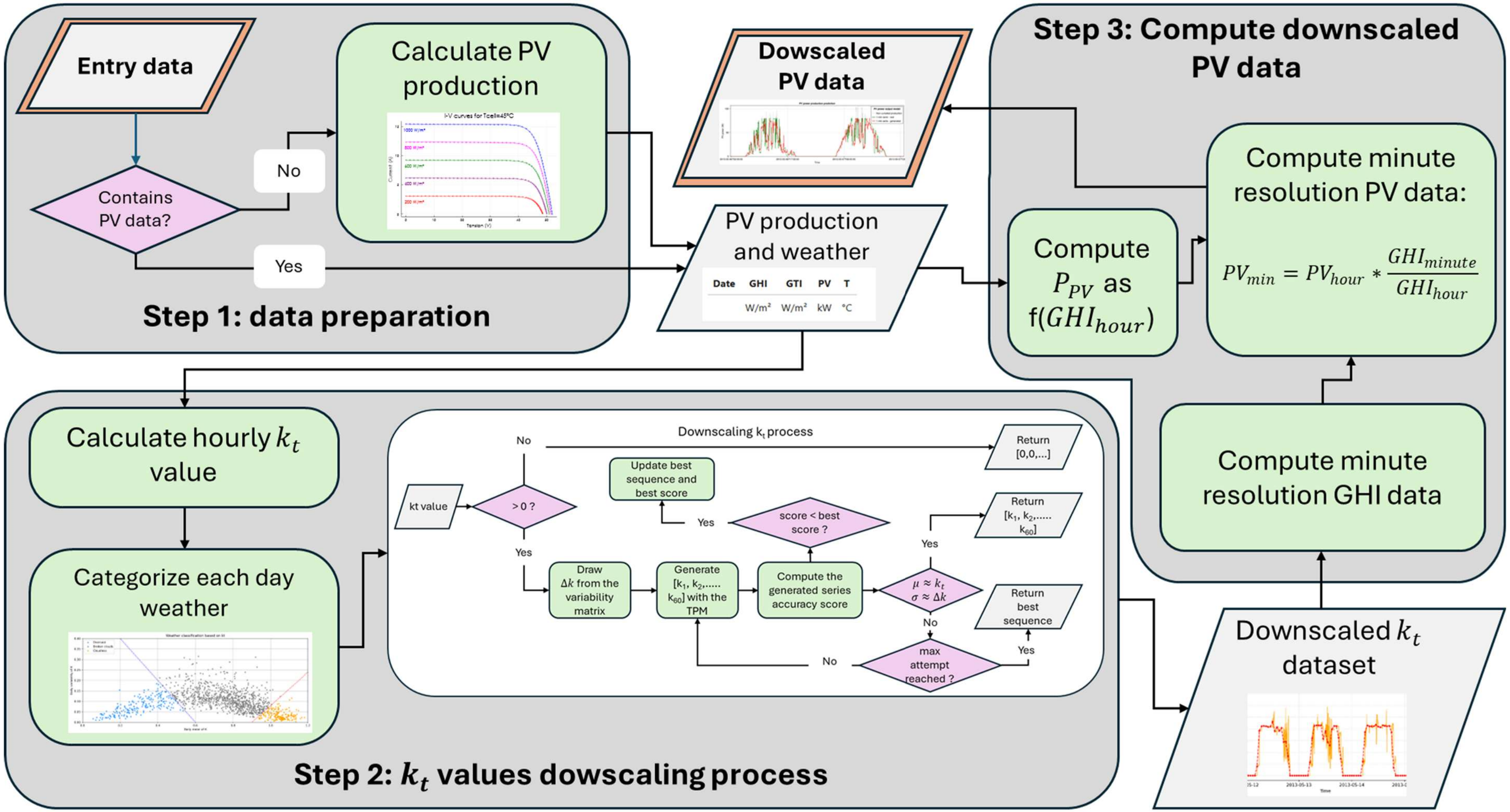

Figure 2.28 – Complete dowscaling process summerization

CHAPTER 3 BATTERY ENERGY STORAGE SYSTEM

The main objective of this chapter is to develop a complete dynamic battery model and to extend it with an aging model. The first part reviews relevant literature, then in the second one, a dynamic model based on a real lithium-ion cell (K218650E) is developed. It is followed by the definition of a generic cell model designed for early-stage simulations. Finally, the aging model is introduced for long-term performance analysis.

3.1 Literature review

3.1.1 Battery chemistry

The heart of a battery energy storage system (BESS) is the battery, which is a device that stores chemical energy and converts it to electricity, through an electrochemical oxidation-reduction reaction. Today, one of the modern energy storage technologies with the highest commercial demand is lithium-ion batteries (LIBs). It is a type of high energy density rechargeable battery that operates based on the movement of lithium ions between two electrodes (the anode and the cathode) during charging and discharging processes. (Chandler, 2014)

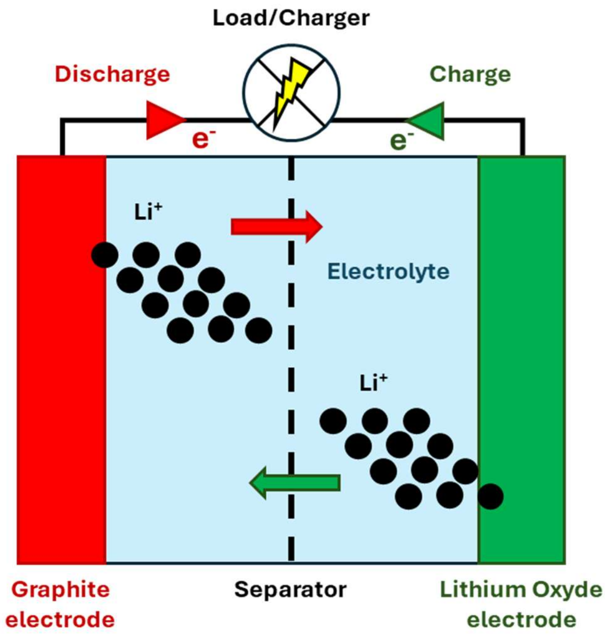

Figure 3.1 - Components and theoretical functioning of a LIB

A li-ion battery is composed of the following main elements (Boparai & Singh, 2020) as illustrated in Figure 3.1:

- The cathode: the positive electrode to which cations migrate, made of lithium oxide
- The anode: the negative electrode to which anions migrate, typically composed of graphite, a layered carbon material.
- The electrolyte: A medium made of lithium salt in organic solvent, placed between the electrodes to allow the lithium ions to move freely while carrying charge.
- The separator: A layer placed between two electrodes; its role is to prevent short circuiting.

During charging, lithium ions travel from the cathode through the separator to the anode, where they are stored within the graphite layers. While discharging, the ions move back to the cathode through the electrolyte, releasing energy

There are several different types of LIBs, primarily distinguished by the materials used in their cathodes (Sobianowska-Turek et al., 2021). Table 3.1 below provides an overview of the main characteristics for some of the important LIBs cathode materials:

Table 3.1 - Cathode material comparison, (Marie & Gifford, 2023) & (Apribowo et al., 2022)

Cathode material	**Battery technology acronym**	**Date**	**Cost range**	**Energy density [Wh/kg]**	**Cycle life[1]**	**Safety rating**
Cobalt oxide [$LiCoO_2$]	LCO	1990	High	150-200	500-1000	Low
Manganese oxide [$LiMn_2O_4$]	LMO	1983	Low	100-150	300-700	Low
Iron phosphate [$LiFePO_4$]	LFP	1996	Low	90-120	>2000	High
Lithium manganese cobalt [$LiNiMnCoO_2$]	NMC	1999	High	150-250	1000-2000	Low
Nickel cobalt aluminum [$LiNiCoAlO_2$]	NCA	1999	High	200-250	500	Low

[1] The cycle life of a battery represents the number of charge / discharge cycles that can be performed over its useful life.

LFP batteries have recently emerged as the best suited batteries type for BESS, where safety is extremely important, as they are less prone to overheating and thermal runaway. Additionally, they have long cycle life, which improve their suitability for long term use (Sobianowska-Turek et al., 2021).

The reaction mechanism in a LFP battery is described by the following equations (Arote, 2022):

$$\text{On the cathode side: } Li_{m-n}FePO_4 + nLi^+ + ne^- \xLeftrightarrow{charg\ \ /discharg} Li_mFePO_4$$

$$\text{On the anode side: } Li_nC_6 \xLeftrightarrow{charg\ \ /discharg} nLi^+ + ne^- + C_6$$

$$\text{Overall: } Li_mFePO_4 + C_6 \xLeftrightarrow{charg\ \ /discharge} Li_{m-n}FePO_4 + Li_nC_6$$

The battery voltage determines the driving force for the movement of electrons in an external circuit and is a critical parameter for the battery's performance. It is affected by the current load and the internal resistance and allows the monitoring of the useful power delivery (P) as it is directly linked to it:

$$P = IV - I^2R_{int} \tag{3.1}$$

where I is the current drawn from a battery, V is the battery voltage, and R_{int} is the internal resistance of the battery. Thus, to get the maximum useful power the internal resistance must be kept to a minimum.

Li-ion batteries offer several advantages (Arote, 2022):

- High energy density: Lithium's high reactivity allows significant energy to be stored in its atomic bonds, giving lithium-ion batteries their high energy density. This results in smaller size, reduced material usage, and easier installation.
- High cell voltage: A single lithium-ion battery cell delivers a working voltage of approximately 3.6 V, which is two to three times higher than that of Ni-Cd, NiMH, or lead-acid battery cells.
- No memory effect: There is no need for complete discharge before recharging.
- Low self-discharge rate: Lithium-ion batteries self-discharge minimally, losing about 5 % of the state of charge in the first four hours and 1–2% per month afterward.

- Long cycle life: Several factors influence a battery's cycle life, but under standard conditions, lithium-ion batteries typically achieve a longer cycle life of 1500-2000 charge/discharge cycles for the best one, compared to 300-500 for lead-acid batteries.

However, they also have drawbacks: they have a limited lifespan independently of the number of charge/discharge cycles, typically lasting a few years, and a high temperature sensitivity, which can reduce performance and safety.

3.1.2 Battery degradation process

LIBs aging is typically classified into three primary degradation mechanisms (Vermeer et al., 2022):

1. Loss of lithium inventory: This refers to the reduction of active lithium ions that are available for charge cycling. Loss of lithium inventory is primarily caused by parasitic side reactions, including surface film formation, electrolyte decomposition, and lithium plating. This aging mode directly contributes to capacity fade.
2. Loss of active material: This mode represents the structural degradation or loss of available electrode material (anode or cathode). Factors such as electrode surface layer growth, cycling-induced cracking, and exfoliation can lead to loss of active material. The resulting degradation impacts both capacity retention and power output of the battery.
3. Conductivity loss: Also referred to as contact loss, this degradation mechanism involves the deterioration of electrical components within the battery. Causes include current collector corrosion and binder decomposition, leading to increased internal resistance and impaired electrical conductivity.

Lithium-ion battery degradation is further categorized into two dominant aging modes (Vermeer et al., 2022):

- Calendar aging: it refers to the degradation of LIB over time when it is not actively cycled (i.e., during storage or idle periods). Factors influencing calendar aging include temperature, state of charge (SOC), and storage duration. The higher the storage temperature, the faster the calendar aging. Similarly, aging will generally be greater for a high SOC than for a low SOC.

- Cyclic aging: This type of aging results from repeated charge and discharge cycles. The depth of discharge, charge/discharge rate, and operating temperature are key factors influencing cyclic aging.

3.1.3 Challenges of BESS deployment

Deploying a high-performing BESS is inherently complex, as it involves balancing multiple considerations, including cost, reliability, environmental impact, and system degradation (Prakash et al., 2022).

3.1.3.1 Environmental impact

While BESS facilitate higher renewable energy penetration and reduces overall greenhouse gas emissions at the grid level, they also pose environmental challenges across their life cycle, from raw material extraction and manufacturing to operation and end-of-life. The production of materials and battery manufacturing represent the most carbon-intensive stages (up to 80% for nickel-based batteries). Overall global GHG emissions associated with battery manufacturing range from 55 $kgCO_2eq/kWh$ for LFP batteries to 82 $kgCO_2eq/kWh$ for NCA ones, as shown on Figure 3.2 (Llamas-Orozco et al., 2023).

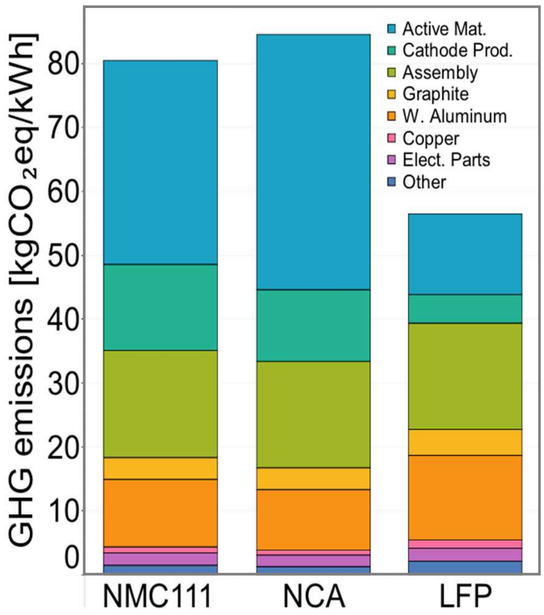

Figure 3.2 - GHG emissions of 1kWh of different LIB technologies (Llamas-Orozco et al., 2023)

Additionally, batteries' misutilization can also worsen environmental performance. For instance, in Texas, several large-scale BESS installations have been observed to increase net CO_2 emissions because their operators chose to focus on maximizing revenues by charging batteries with coal or gas power to engage in energy arbitrage later. (Plumer & Popovich, 2024)

Finally, batteries' end of life management is a key challenge to reduce their environmental impact. Indeed, LIBs contain hazardous materials such as lead, cadmium or lithium, which can contaminate soil and water if not properly disposed of. Additionally, it is necessary to improve recycling capabilities to minimize waste and reduce the demand for new raw materials (Gutsch & Leker, 2024).

3.1.3.2 Economic concerns

Despite the long-term decline in energy storage costs, illustrated by a 71 % drop in BESS prices between 2014 and 2022, as reported by IRENA, and further reductions anticipated, costs remain a significant concern for their deployment. In addition to high upfront investment, BESS incur recurring operational costs, covering maintenance, monitoring, and battery replacement. (NREL, 2024a)

In addition to manufacturing and installation expenses, BESS costs are influenced by fluctuations in raw material prices, supply chain constraints, and evolving trade policies. Indeed, BESS batteries, particularly those based on the lithium-ion technology, rely on raw materials such as lithium, cobalt, and nickel, that are subject to price volatility due to their country of origin (Thakur & Labanya Prakash, 2024).

3.1.3.3 Safety risks

Even under normal operating conditions, it is challenging to fully dissipate the heat generated by batteries, particularly on hot days or within large battery packs. Elevated battery temperatures can initiate undesirable parasitic reactions, potentially leading to thermal runaway - a condition where heat generation becomes uncontrollable. (Chen et al., 2021).

To mitigate these risks, LFP batteries are increasingly utilized due to their better thermal and chemical stability compared to other lithium-ion chemistries, such as NCM (Sobianowska-Turek et al., 2021).

3.1.3.4 Storage limitations

BESS are effective in managing daily fluctuations in energy supply and demand, as they can store excess energy generated during peak production hours for use during periods of high demand within the same day. However, seasonal storage remains beyond the practical and economic limits of current battery technologies. Typical BESS are designed to provide energy shifting over periods in the order of 4 hours (DOE, 2023), so even providing a week's worth of storage would require multiplying the storage capacity by over 40.

3.1.4 Battery models in literature

3.1.4.1 Parameters identified

The following section will present the definitions of parameters used in battery models (Arote, 2022).

Voltage and Current

The battery voltage, V_{bat}, represents the effective voltage difference across the battery terminals, while the battery current, I_{bat}, refers to the current flowing into or out of the battery.

The open-circuit voltage, V_{OC}, is the voltage between the positive and the negative electrodes when no external current flows.

Capacity

The battery capacity is the total amount of electrical charge a battery can store, typically expressed in ampere-hours (Ah). It represents the amount of current a battery can deliver over a specified period, reflecting its energy storage capability. For example, a battery with a capacity of 10 Ah can theoretically provide 1 ampere of current for 10 hours or 2 amperes for 5 hours, depending on its discharge characteristics and conditions. In reality, higher discharge currents reduce the usable capacity. This is expressed using the C-rate, which is the ratio of the discharge current to the theoretical current that would empty the battery in 1 hour. In the example above, a 10 Ah battery discharged with a 10 A current would be fully discharged in 1 h. This is called the "1C" value (i.e. the capacity for a full discharge in 1 hour). The same battery would probably have a lower usable capacity at higher currents; for example, if it was discharged with a current of 20 A, it would be empty in 0.45 h, so its "2C" capacity would be equal to 9 Ah only. Conversely, if it was discharged with a current of 1 A, it would be empty after 11 h, so its "0.1C" or "C/10" capacity would be 11 Ah

It should be noted that the battery capacity is not strictly equivalent to the energy storage capacity, which is the product of the capacity (in Ah) and the voltage (in V) – this voltage can vary with operating conditions and battery aging.

The capacity degradation rate of the battery depends on several factors, such as the temperature, the number of cycles or the speed of discharge (Apribowo et al., 2022). Several sub concepts of battery capacity can be defined and are illustrated in Figure 3.3.

- Nominal (rated) capacity: It is the capacity of battery at the beginning of life. It is usually provided in manufacturer datasheets at a 1C-rate.
- Available capacity: It is the available capacity of the battery at any given instant of battery lifetime. It is generally lower than the rated capacity due to battery aging, and the ratio between the reduced capacity and the rated capacity is called the state-of-health of the battery (SOH, see below)
- Dynamic capacity: The number of Ampere-hours which are stored in the battery at a given instant. The ratio between the dynamic capacity and the available capacity is the state-of-charge (SOC, see below) of the battery

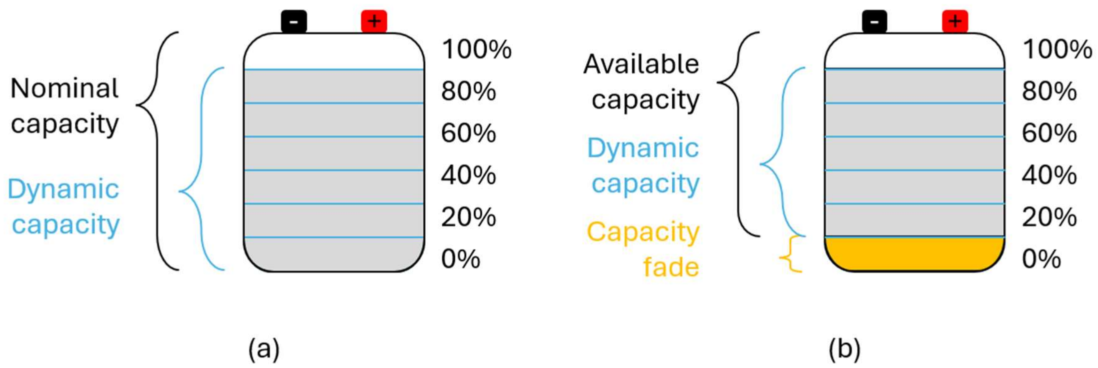

Figure 3.3 - Battery Capacity; (a) in the beginning & (b) end of life

State of charge

The state of charge (SOC) of a battery is a measure of the amount of energy (or more exactly Ampere hours) remaining in the battery relative to its available capacity. It is typically expressed as a percentage, where:

$$SOC = \frac{Dynamic\ capacity}{Available\ capacity} * 100\%$$

- 100% SOC indicates the battery is fully charged.
- 0% SOC means the battery is completely discharged.

These two limits must remain valid regardless of the battery's level of aging, which is why the available capacity is used and not the nominal one. The SOC provides a dynamic indicator of the battery's charge level during operation, helping to assess its availability and manage energy usage effectively.

Depth of discharge

The depth of discharge (DOD) of a battery is the percentage of the battery's total capacity that has been discharged relative to its maximum capacity. It indicates how much energy has been used from the battery. Usually, $DOD = 1 - SOC$.

State of health

The state of health (SOH) of a battery is a measure of its overall condition and ability to perform relative to its nominal capacity and specifications. It is typically expressed as a ratio between its current capacity and the initial one:

$$SOH = \frac{C_{bat}^{t}}{C_{bat}^{ini}} \qquad 3.2$$

When the SOH reaches a certain limit (usually around 80%), the battery needs to be replaced to maintain its acceptable minimum performance. The SOH of a battery is a ratio of two quantities in Ah, but it can also be calculated in terms of energy to account for both the loss of capacity and resistance degradation.

$$SOH_{energy} = \frac{\int_{SOC=1}^{SOC=0} V_{bat,ini} * I * dt}{\int_{SOC=1}^{SOC=0} V_{bat} * I * dt} \qquad 3.3$$

Other factors, such as internal resistance, self-discharge rate or voltage efficiency can be used.

3.1.4.2 Battery modeling methods for LIBs

Various approaches have been developed for modeling lithium-ion batteries, with the most widely accepted methods being the electrochemical models, data-driven models, and equivalent circuit models (Fan et al., 2025).

Electrochemical models use physics-based equations to simulate the internal chemical and physical processes of a battery, such as ion transport and reaction kinetics, providing highly detailed insights into its behavior.

Data-driven models rely on machine learning or statistical tools to learn from past data to predict battery behavior without requiring knowledge of its internal mechanisms.

Equivalent circuit models (ECM) represent the battery as an electrical circuit with components like resistors, capacitors, and voltage sources to mimic its external voltage and current behavior in a simplified way. The circuit is formed by a resistor which represents the internal resistance of the battery, and a series of n circuits representing the n chemical reactions occurring within the battery.

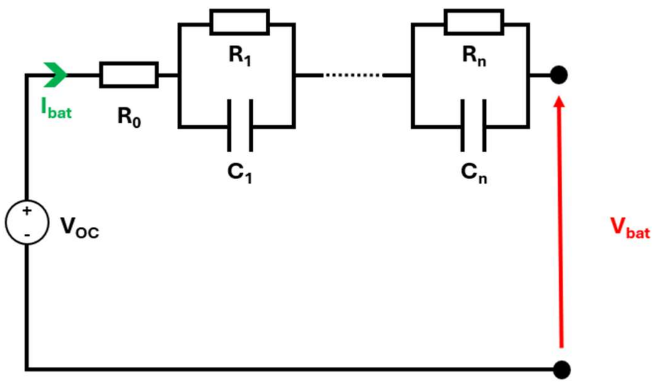

Figure 3.4 - n-th order ECM model

The first circuit represents the primary redox reaction, while the remaining *n-1* circuits account for parasitic reactions. These different models are compared in Table 3.2

Table 3.2 - Comparison between typical LIBs models

Aspect	Equivalent circuit models	Electrochemical mechanism models	Data – driven models
Mathematical framework	Ordinary differential equations using standard circuit elements (resistors, capacitors)	Partial differential equations derived from electrochemical principles	Statistical/machine learning frameworks (e.g., neural networks, regression models)
Accuracy	Good accuracy as it simplifies battery behavior	High accuracy, especially for studying the internal behavior	Depends on the dataset used for the training
Computational demand	Low: efficient for real-time application	High: suitable for simulation purpose	Medium: ML models require high computational effort during training but low computational cost during deployment.
Applicability	ECM integer-order is the most efficient approach that combines both good accuracy and low computational demand	The complexity of LIBs requires many partial differential equations, making this model difficult to apply, despite simplification efforts.	This approach relies on extensive historical data, making it impractical

3.1.4.3 Battery modeling methods review

The objective of the section is to present several models that have been identified in the literature.

(Navas et al., 2023) model

Navas et al. (2023) presents a model for a first-order ECM as presented on Figure 3.5.

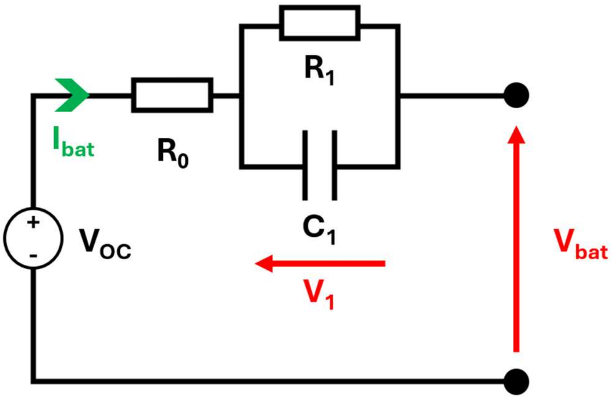

Figure 3.5 - 1st order ECM

This circuit can be modeled by the following equations:

$$\begin{cases} \frac{dV_1}{dt} = -\frac{1}{R_1C_1}V_1 + \frac{1}{C_1}I_{bat} \\ V_{bat} = V_{OC} - R_0I_{bat} - V_1 \end{cases} \quad 3.4$$

Where R_0 and R_1 are in Ω and C_1in F. The first equation in 3.4 can then be solved to obtain:

$$V_{1,t+\Delta t} = V_{1,t}.e^{\frac{-\Delta t}{R_1C_1}} + R_1.I_{bat}.\left(1 - e^{\frac{-\Delta t}{R_1C_1}}\right) \quad 3.5$$

The study has experimentally determined the following relationship between the ECM parameters and SOC:

For the discharge process:

$$\begin{cases} R_0 = 510.10^{-9} * SOC^2 - 153.10^{-6} * SOC + 0.0752 \\ R_1 = 104.10^{-6} * SOC^2 - 147.10^{-4} * SOC + 0.627 \\ C_1 = -2.580 * SOC^2 + 383.068 * SOC + 4057.595 \end{cases} \quad 3.6$$

And for the charging process:

$$\begin{cases} R_0 = 204.10^{-8} * SOC^2 - 495.10^{-6} * SOC + 0.0895 \\ R_1 = 476.10^{-7} * SOC^2 - 662.10^{-5} * SOC + 0.311 \\ C_1 = 0.784 * SOC^2 + 96.632 * SOC + 4664.594 \end{cases} \quad 3.7$$

The open circuit voltage is also directly related to the state of charge:

$$V_{oc} = 0.000019 * SOC^3 - 0.00396 * SOC^2 + 0.284 * SOC + 46.158 \quad 3.8$$

This model does not consider the dependence of the parameters on temperature or the ageing of batteries.

(Tremblay et al., 2007)

The model introduced by Tremblay et al. (2007) is a zero-order ECM, which has been widely adopted for LFP battery modeling, including in tools such as SAM (NREL, 2015) and Energy Plus (DOE, n.d.). It is based on the Shepherd model (Shepherd, 1965) whose formulation is particularly well-suited for LFP cells as it reproduces the characteristic flat discharge plateau between 20 % and 80 % SOC. In the model, the open circuit voltage $V_{OC}(t)$ is expressed as:

$$V_{OC}(t) = E_0 - K\frac{C_{bat}}{C_{bat} - q(t)}I_{bat}(t) - RI_{bat}(t) + A\exp^{-Bq(t)} \quad 3.9$$

where:

- E_0 is the constant open-circuit voltage at full charge,
- C_{bat} is the nominal capacity,
- $q(t) = \int_0^t I_{bat}(\tau)\, d\tau$ is the extracted charge,
- R is the internal resistance,
- K is the polarization constant,
- A and B describe the exponential voltage zone observed at the beginning of discharge.

3.2 Battery data

3.2.1 Stanford battery data (Chueh et al., 2024)

A research team at Stanford University has conducted a long-term (13-year) study on calendar aging in lithium-ion batteries. The experiment focused on eight commercially available cell types, which were stored under controlled conditions to isolate the effects of the SOC and temperature on battery degradation. Each cell type was stored at two SOC levels – 50% or 100% – and exposed to four different temperatures: 24 °C, 45 °C, 60 °C, and 85 °C. The dataset, which provides full open-access information on capacity fade and impedance growth over time, has been made publicly available (Chueh et al., 2024) and the results were summarized in a recent article (Lam et al., 2025).

The batteries were stored in open-circuit conditions and were regularly taken out (every week or month depending on the temperature storage) to conduct diagnostic cycles to monitor their state of health. The procedure consisted of the following steps:

- Three low-rate charge/discharge cycles (at C/5)
- Three high-rate cycles (between 1C and 3C, depending on the cell type)
- A capacity test at C/5
- A recharge to the designated storage SOC (either 50% or 100%)

Each cycle is done between a chosen low and high voltage cutoff.

In particular, the team studied the degradation of two types of LFP batteries over 8 years: the K2 Energy LFP18650E and K2 Energy LFP18650P, whose characteristics are presented in Table 3.3. The highlighted cell, K2E18650E is the one that will be used to calibrate the proposed battery model in the next sections, as its commercial datasheet (K2 Energy Solutions, Inc., n.d.-a) is available and provides additional information.

Table 3.3 - LFP cells information, (Lam et al., 2025)

Manufacturer	Cell name	Nominal capacity [Ah]	High-rate C-Rate	Low voltage Cutoff	High voltage Cutoff
K2 Energy	LFP18650E	1.50Ah	3C	2.00V	3.60V
K2 Energy	LFP18650P	1.10Ah	3C	2.00V	3.65V

The diagnostic cycles are subdivided into units, each consisting of a rest–charge–rest–discharge sequence. A complete diagnostic cycle is composed of eight consecutive units, as illustrated in Figure 3.6 below.

We can also see the pattern of the diagnostic cycle (three low-rate cycle, three high-rate cycle, one low-rate cycle and finally a cycle to reach the desired SOC, here 50%)

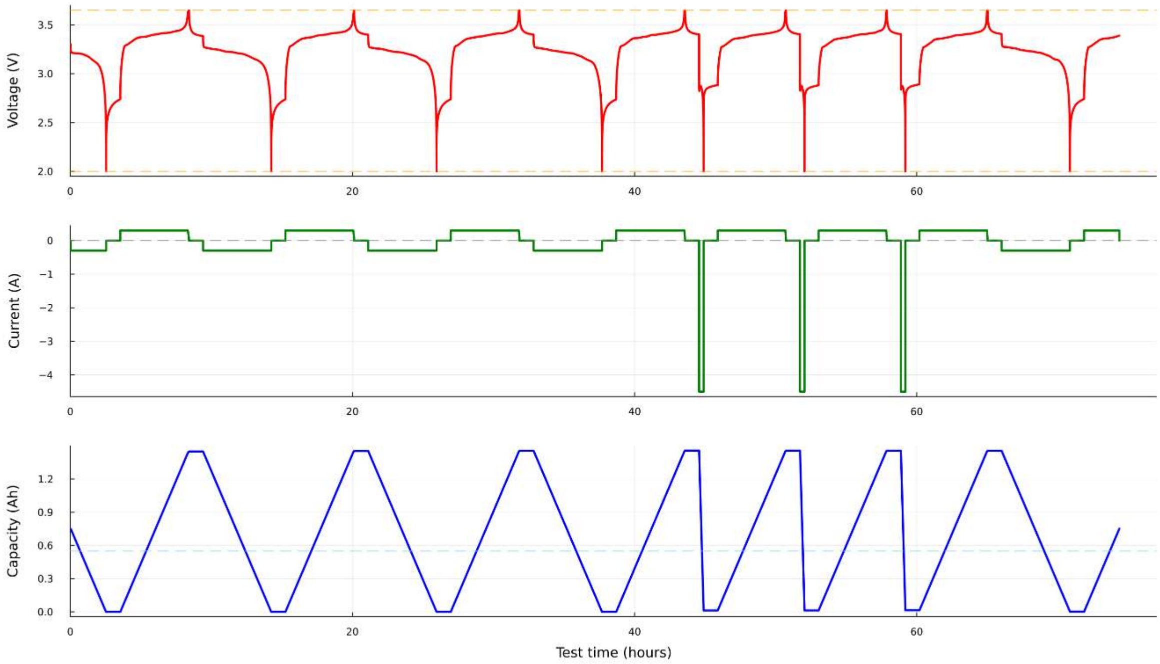

Figure 3.6 - Current, voltage and capacity monitoring of the LFP18650E on its first diagnostic cycle

This raw data has allowed the team from Stanford to measure the long-term evolution of the relative capacity and relative resistance of the cells defined as:

$$\begin{cases} Q_{rel}(t)[\%] = \dfrac{Q(t)}{Q_{non}} \\ R_{rel}(t)[\%] = \dfrac{R(t)}{R_{ini}} \end{cases} \tag{3.10}$$

The results are presented on Figure 3.7.

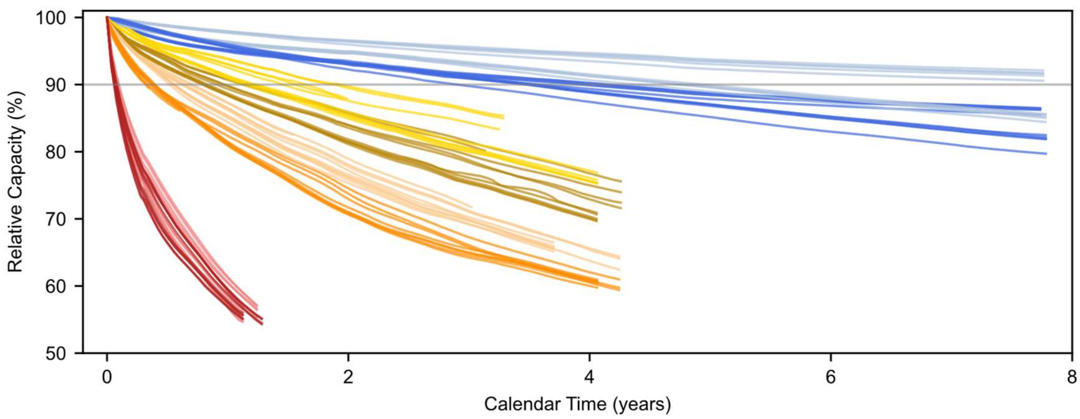

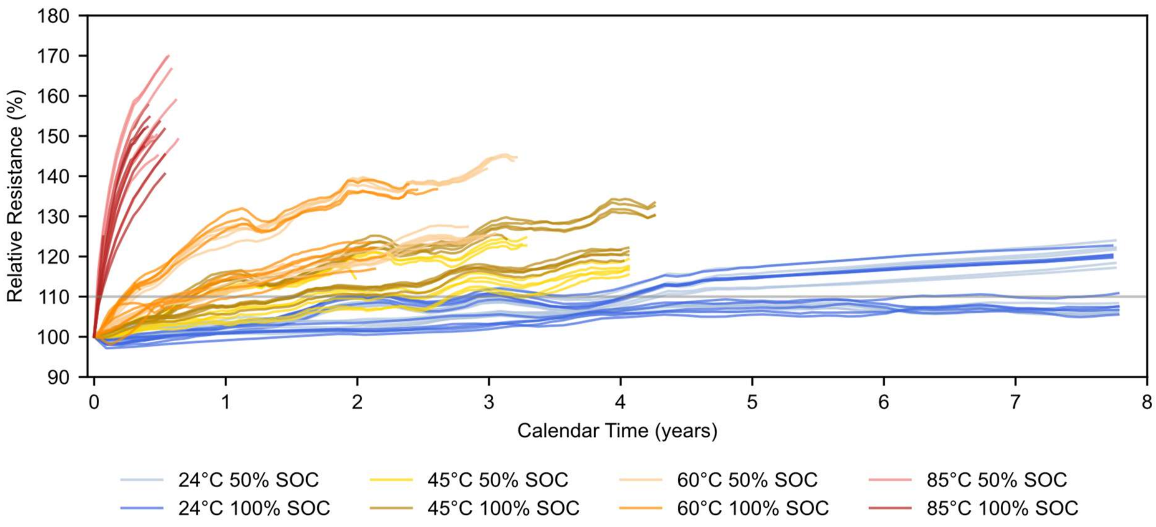

Figure 3.7 - Evolution of the relative resistance and capacity of the LFP cells

The resistance of the cell is defined to measure how much energy is lost by going to higher rates:

$$R = \frac{\overline{V_{high\ rate}} - \overline{V_{low\ rate}}}{3C - C/5} \qquad 3.11$$

3.2.2 Generic model

To address situations where detailed cell information is unavailable, a generic cell model will also be proposed for early-stage and system-level simulations. To that end, five additional commercial LFP cylindrical cells have been selected (cell 2 to 6). These data were obtained from publicly available manufacturers' datasheets and include complete discharge voltage curves under various current rates as well as R_0 value. The selected cells are in Table 3.4 and cover a range of capacities (1.2 Ah to 2.6 Ah) and C-rates (C/8 to 20C) representatives of the diversity in LFP cells. The cell n°1 is the one presented in the previous section, that will act as the reference cell.

Table 3.4 – Overview of the speficication of the selected commercial cells

N°	**1**	**2**	**3**	**4**	**5**	**6**
Manufacturer	K2 Energy	K2 Energy	K2 Energy	A123	LithiumWerks	LithiumWerks
Cell name	LFP18650E - 1500	LFP18650P - 1250	LFP18650P - 1350	ANR26650 – M1B	APR18650 – M1B	ANR26650 – M1B
Capacity [Ah]	1.50 Ah	1.25 Ah	1.35 Ah	2.6 Ah	1.2 Ah	2.6 Ah
R_0 [mΩ]	40	19	13	6	15	10
V_{nom} [V]	3.2	3.2	3.3	3.3	3.3	3.3

C-rate	C/5, C/2, C, 3.33C, 6.66C, 10C	0.96C, 4C, 8C, 12C	0.22C, 0.44C, 0.88C, 1.85C, 3.7C, 7.4C, 11.11C, 14.8C, 18.51C[2]	C/8, 2C, 4C, 7C, 10C	C, 2C, 4C, 6C, 8C, 10C, 12C	C, 2C, 4C, 6C, 10C, 14C, 20C
Reference	(K2 Energy Solutions, Inc., n.d.-a)	(K2 Energy Solutions, Inc., n.d.-b)	(K2 Energy Solutions, Inc., n.d.-c)	(A123, 2019)	(LithiumWerks, 2021)	(LithiumWerks, 2024)

3.3 Proposed dynamic battery model

3.3.1 Equivalent circuit model

To model the relationship between the current and the voltage in the battery, a first order ECM is used based on the work by Naves et al. (2023). The equivalent circuit can be modeled by the following equations:

$$\begin{cases} \dfrac{dV_1}{dt} = -\dfrac{1}{R_1 C_1} V_1 + \dfrac{1}{C_1} I_{bat} \\ V_{bat} = V_{OC} - R_0 I_{bat} - V_1 \end{cases} \tag{3.12}$$

Where the discrete-time solution of the derivative equation is:

$$V_{1,t+\Delta t} = V_{1,t}.e^{\frac{-\Delta t}{R_1 C_1}} - R_1.I_{bat}.\left(1 - e^{\frac{-\Delta t}{R_1 C_1}}\right) \tag{3.13}$$

The different parameters $R_0, R_1\ and\ C_1$ are constant parameters fitted to the data.

3.3.2 Capacity and SOC computation

To take into account the impact of the charge and discharge current on the available capacity of a Lithium-ion battery, Peukert's law (Peukert, 1897) is used:

$$C_{eff}(I_{bat}) = C_{ref} * \left(\frac{I_{ref}}{I_{bat}}\right)^{k-1} \tag{3.14}$$

Where $C_{eff}\ (I_{bat})$ is the effective available capacity at current I_{bat}, C_{ref} is the rated capacity measured at reference I_{ref} and k is the Peukert coefficient.

The SOC of the cell is then computed based on the Coulomb counting (Eq. 3.15).

$$SOC(t + dt) = SOC(t) + \frac{dt * I_{bat}(t)}{C_{eff}(I_{bat})} \tag{3.15}$$

[2] The original datasheet reported discharge currents directly in amperes (0.3, 0.6, 1.2, 2.5, 5, 10, 15, 20, 25 – A)

Finally, to calculate the state of charge and V_1 at each time steps, Eq. 3.12 and 3.13 can be written in a matrixial format as follows:

$$\begin{bmatrix} SOC_{t+1} \\ V_{1,t+1} \end{bmatrix} = \begin{bmatrix} 1 & 0 \\ 0 & e^{\frac{-\Delta t}{\tau}} \end{bmatrix} * \begin{bmatrix} SOC_t \\ V_{1,t} \end{bmatrix} + \begin{bmatrix} \Delta t / C_{eff} \\ -R_1 . \left(1 - e^{\frac{-\Delta t}{\tau}}\right) \end{bmatrix} * I_{bat,t} \qquad 3.16$$

3.3.3 V_{oc} model

The relationship between the open voltage circuit V_{oc} and SOC is modeled using Tremblay's formulation (Tremblay et al., 2007). However, to simplify its implementation, $q(t)$ is expressed as $SOC(t) * C_{nom}$ which allow Eq. 3.9 to be rewritten as:

$$V_{OC} = a_0 - \frac{a_1}{1 - SOC(t)} + a_2 * e^{-a_3 * SOC(t) * C_{nom}} \qquad 3.17$$

3.3.4 Dynamic model summary

In conclusion, there are seven coefficients to generalize in the proposed ECM model:

- The four coefficients a_0, a_1, a_2 and a_3 used in V_{oc} calculation
- The cell resistance R_1 and capacitance C_1
- The initial value of the voltage across the RC circuit, $V_{1,0}$

Each parameter influences the shape of the simulated discharge curve in a distinct way. Their individual effects are illustrated in Figure 3.8, where the impact of varying each a_i coefficient (while keeping others constant) is compared against a reference curve.

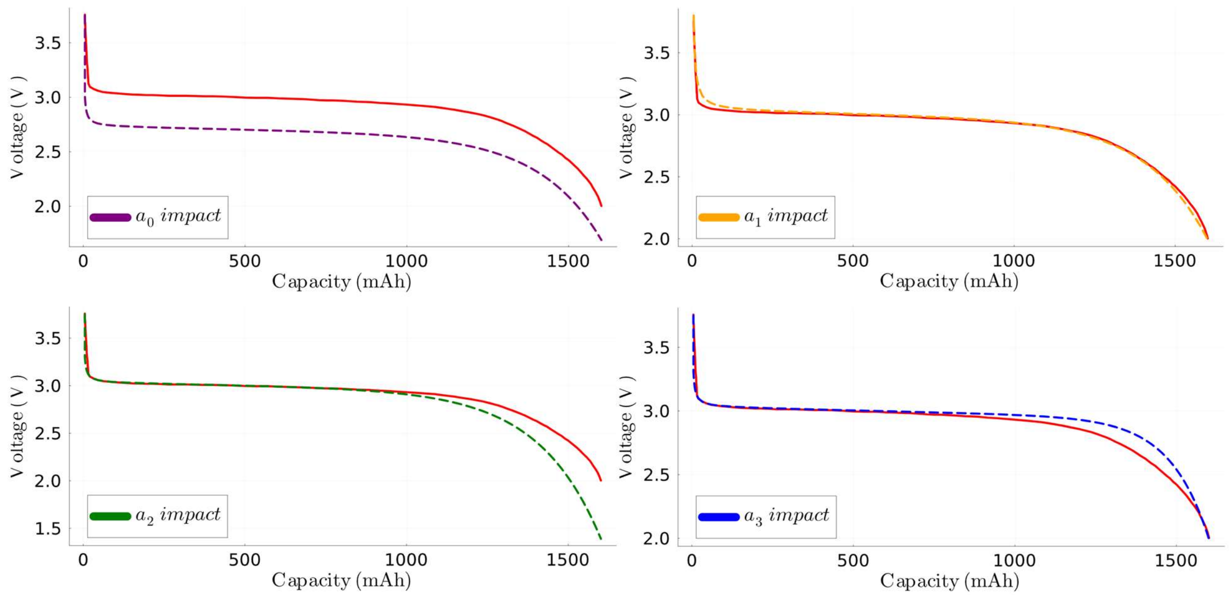

Figure 3.8 - Shepherd's model coefficient impact on the discharge curve. The red curve represents the reference curve, and one parameter is varied in each of the subfigures

The impact of each coefficient is presented in the table below.

Table 3.5 - Shepherd model coefficient impact description

Coefficient	Impact	Is constant in the model
a_0	Affects the overall vertical position of the curve, increasing a_0 shifts the curve upward	✗
a_1	Adjust the smoothness and curvature of the initial voltage drop. It fine-tunes how sharply or smoothly the curve bends just after the discharge begins.	✓
a_2	Shifts the final voltage point at the end of the discharge. A higher a_2 raises the voltage plateau near the end.	✗
a_3	Influences the curvature of the terminal region. Increasing a_3 results in a more pronounced concave bend at the end of the discharge.	✗
R_1 & C_1	Impact the slope of the of the mid-discharge region	✓
$V_{1,0}$	Has a similar impact than a_0 on the overall vertical position of the curve	✓

3.4 Battery cell model validation and generalization

3.4.1 Data preparation

The first step in generalizing the model consists of extracting reference discharge curves from the cell's datasheet. For this purpose, the software WebPlotDigitizer (Ankit, 2023) was used to digitize the voltage-capacity curves presented in the datasheet, with approximately 100 points extracted per curve. Each curve corresponds to a different constant current value (0.3 A, 0.75A, 1.5 A, 5 A,10 A and 15A), as we can see on Figure 3.9.

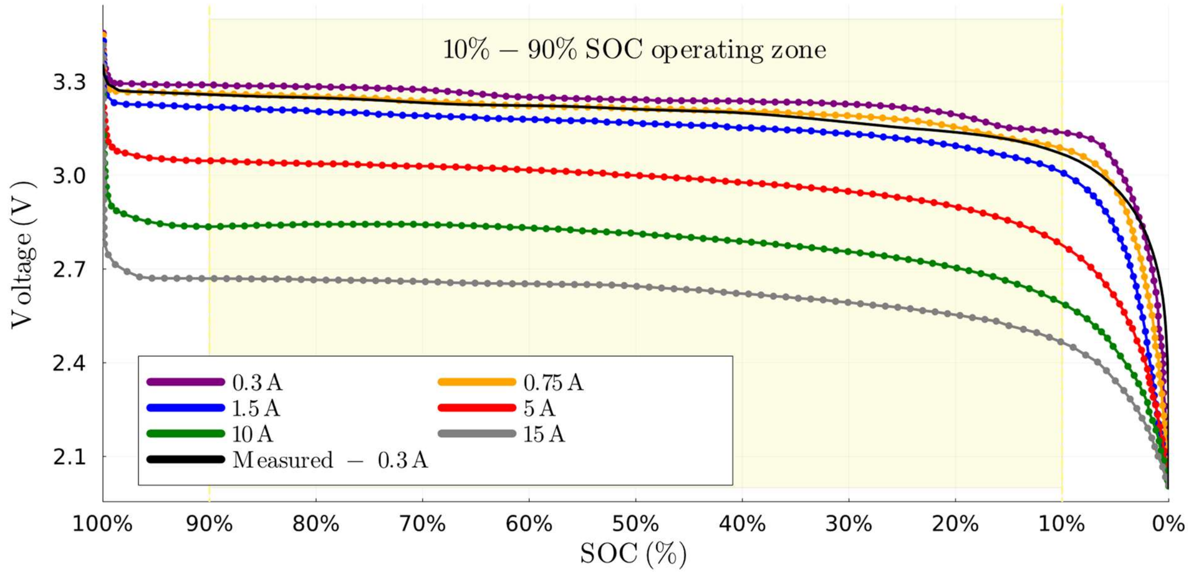

Figure 3.9 - Different discharge rates for K218650E

3.4.2 Model generalization – discharge

After optimization, the sets of coefficients presented in Table 3.6 provide the best fit for each discharge curve at the specified current levels.

Table 3.6 - Shepherd's model optimized coefficient

Current	a_0	a_1	a_2	a_3	R_1	C_1	$V_{1,0}$	R^2
0.3 A	4.277	-0.0004	-1.122	27	10	12	1	0.9875
0.75 A	4.234	-0.0004	-1.104	23	10	12	1	0.9935
1.5 A	4.165	-0.0004	-1.06	18	10	12	1	0.9912
5.0 A	3.863	-0.0004	-0.921	10	10	12	1	0.9653
10.0 A	3.471	-0.0004	-0.73	10	10	12	1	0.9794
15 .0 A	3.08	-0.0004	-0.527	10	10	12	1	0.9649

These values were obtained by minimizing the error between the simulated and measured voltage curves, as illustrated in Figure 3.10. The continuous lines represent datasheet data, while the dashed lines correspond to model predictions obtained from the first-order ECM described in section 3.2.2. The model reproduces accurately the voltage behavior of the battery across all the SOC range, both the flat voltage plateau characteristic of LFP chemistry and the steeper drop near end-of-discharge across all tested current levels. Within the 10–90 % SOC interval, which corresponds to the typical operating range of energy storage systems, the NMAE across all current rates is equal to 0.34 % and R^2 = 0.9803.

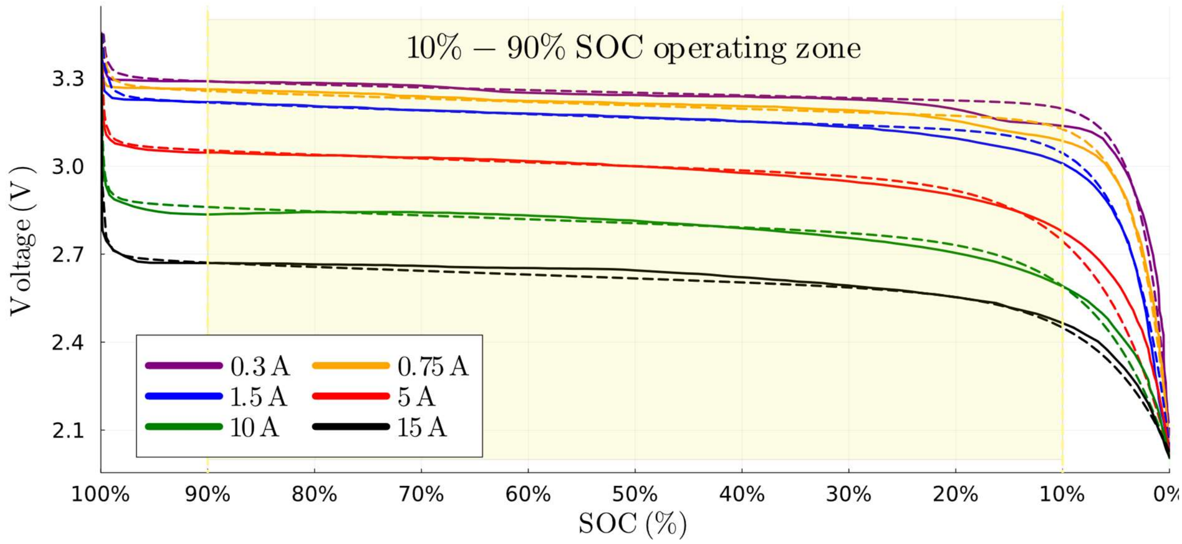

Figure 3.10 - Optimized coefficient for each current

To extend the model's applicability beyond a fixed set of discharge currents, the next step is to generalize the parameters as functions of current. As observed in the previous table, some coefficients (a_0, a_1, a_3) vary significantly with the discharge current, while others remain constant across all tests.

The objective is therefore to identify a mathematical relationship between the discharge current I and the non-constant coefficients. This would enable the model to dynamically adapt its parameters to any given current input. When plotting the different coefficients as a function of current, we can see on Figure 3.11 that a_0 and a_2 show a linear evolution while a_3 follows an exponential trend.

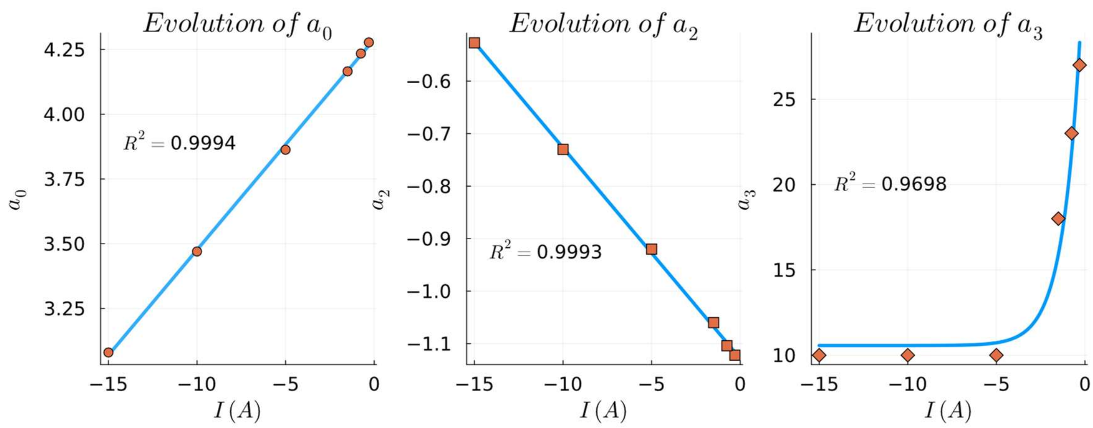

Figure 3.11 - Coefficient evolution as a function of current

The numerical values for each coefficient expression are:

$$\begin{cases} a_0(I) = 4.2896 + 0.0881 * \mathrm{I} \\ a_1(I) = -0.004 \\ a_2(I) = -1.1282 - 0.0401 * \mathrm{I} \\ a_3(I) = \mathrm{e}^{I+3.177} + 10.57 \end{cases} \quad 3.18$$

Finally, the voltage of the battery can be visualized as a function of both SOC and discharge current, as shown in Figure 3.12. The surface represents the model-predicted voltage, while the colored curves correspond to experimental voltage measurements at six different current levels (0.3 A, 0.75, 1.5 A, 5 A, 10 A and 15A).

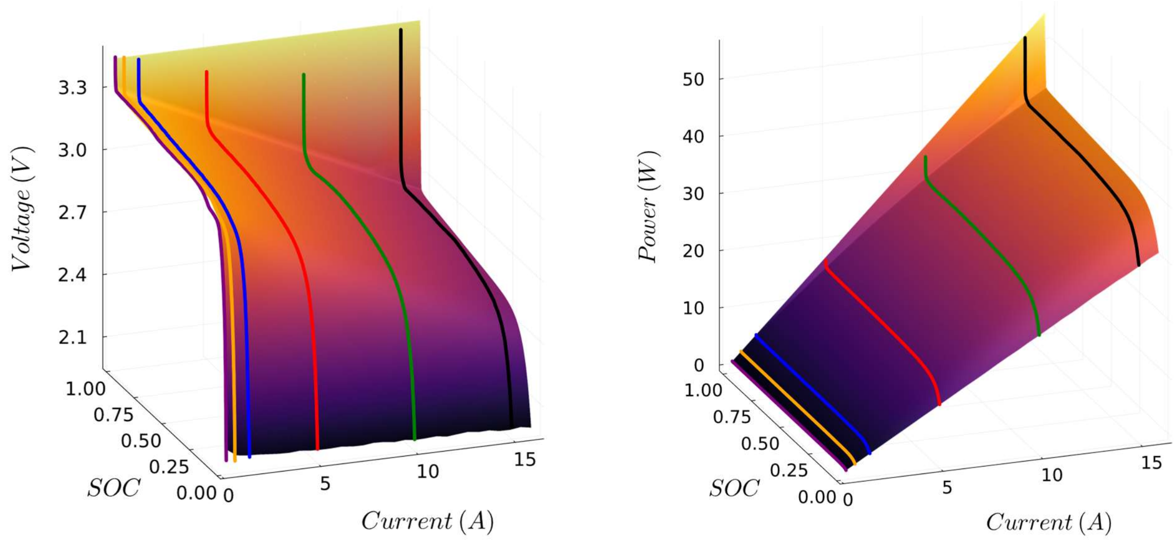

Figure 3.12 - Battery voltage and power as a function of SOC and I during the discharge phase

To validate the previously presented model, the datasheet of the LFP18650P-1350 battery (K2 Energy Solutions, Inc., s. d.a) can be used. A key advantage of this cell is that its datasheet includes measurements at very high C-rates (up to 18C). Those additional current values allow us to assess the model's behavior and the variation of its parameters under high C-rate conditions.

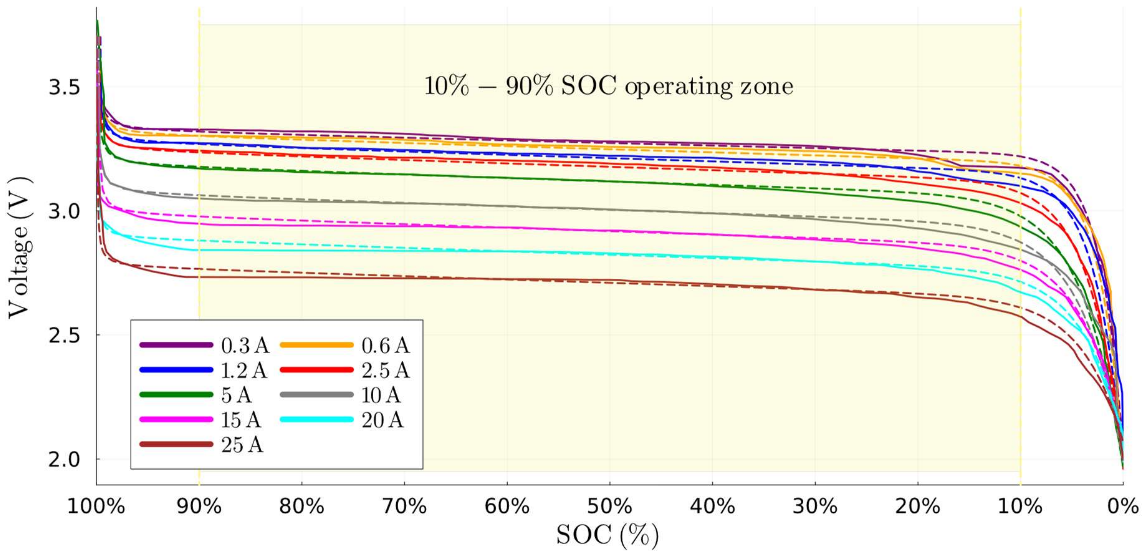

Figure 3.13 - LFP18650P-1350 battery discharging voltage model

When plotting the evolution of a_0, a_2, and a_3, we can see on Figure 3.14 that the linear and exponential trends remain valid, even for high C-rate discharge current.

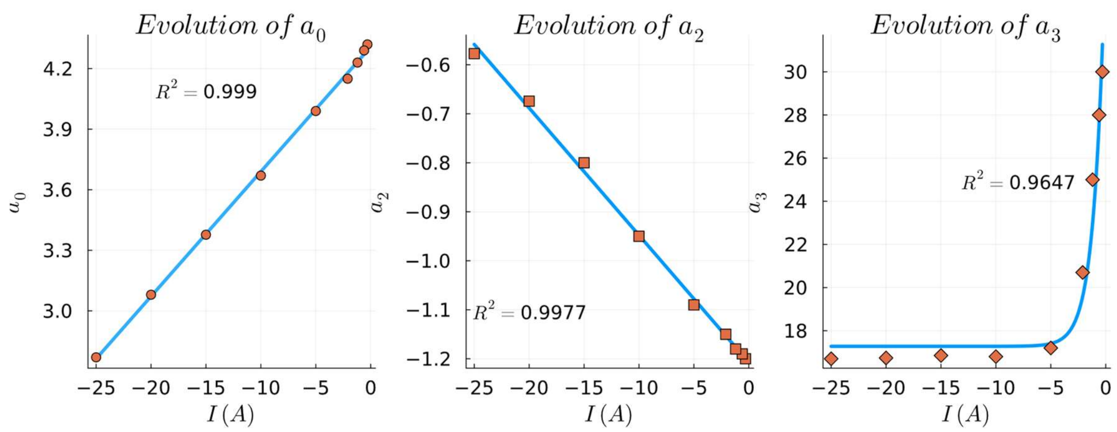

Figure 3.14 - LFP18650P-1350 battery model coefficient evolution

3.4.3 Link between charge and discharge

To assess the accuracy of the previously presented approach for the charging process, we apply the same Shepherd-based model to both charge and discharge processes using the dataset from H.Zhang et al. (2025), that was obtained from 0.7 Ah LFP cells.

The objective is to evaluate whether the model coefficients follow consistent trends across both operating modes and whether the same modeling structure can be extended to the charging process. Table 3.7 reports the model's coefficient R^2 for different currents during charge and discharge.

Table 3.7 - Charge & discharge model accuracy

Current	Charge	Discharge
0.7 A	0.9876	0.9914
1.05 A	0.9940	0.9951
1.4 A	0.9970	0.9976
2.1 A	0.9891	0.9960

The model fits both charge and discharge curves with high accuracy (R^2>0.98).

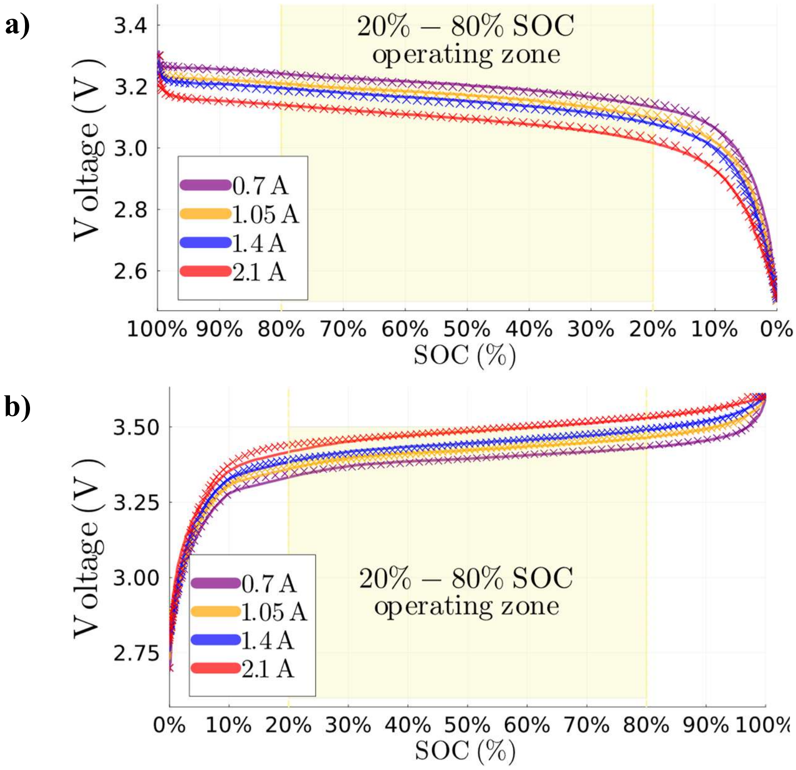

Figure 3.15 - Discharging (a) and charging (b) voltages model applied to (Zhang et al., 2025)

For both operating modes, R_1 remained identical, however the value of C_1 was higher during charging as the slope in the mid-SOC range was steadier. By plotting the optimized model coefficients as a function of the applied current, the profiles presented in Figure 3.16 are obtained.

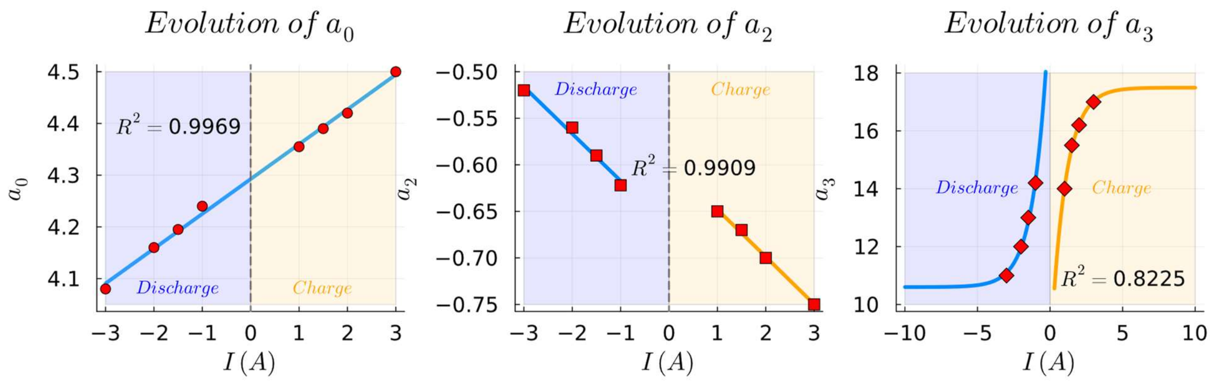

Figure 3.16 - Shepherd's model coefficient evolution for the charge and the discharge

The resulting trends reveal that the coefficients follow the following rules:

- $\boldsymbol{a_0}$ follows a linear trend, which can be extrapolated directly from the discharging coefficient fit
- $\boldsymbol{a_1}$ remains constant across both the charge and the discharge
- $\boldsymbol{a_2}$ evolves symmetrically during the charge and discharge. The vertical difference (i.e. the difference along the voltage axis) between the two linear profiles is equal to ΔV_{Cut-o} at SOC = 0 %. In Figure 3.15, $\Delta V_{Cut\text{-}off}$ = 2.7 – 2.55 = 0.15 V for example. Thus, the model used to adapt a_2 during charge can be deducted from the discharge model.
- $\boldsymbol{a_3}$ also shows a symmetric behavior, which may be interpreted as two asymptotic limits positioned symmetrically around the 1C value.

3.4.4 Model generalization – charge

The previously described methodology was applied to Stanford data, as charging curves at 0.3C are provided. The result presented in Figure 3.19 was optimized using the parameter set presented in Table 3.8.

Table 3.8 - charging paramaters at 0.3C

a_0	a_1	a_2	a_3	R_1	C_1
4.35	-0.0015	-0.51	22.5	10	16.5

In addition to the expected variations in the other parameters, C_1 parameter also increases.

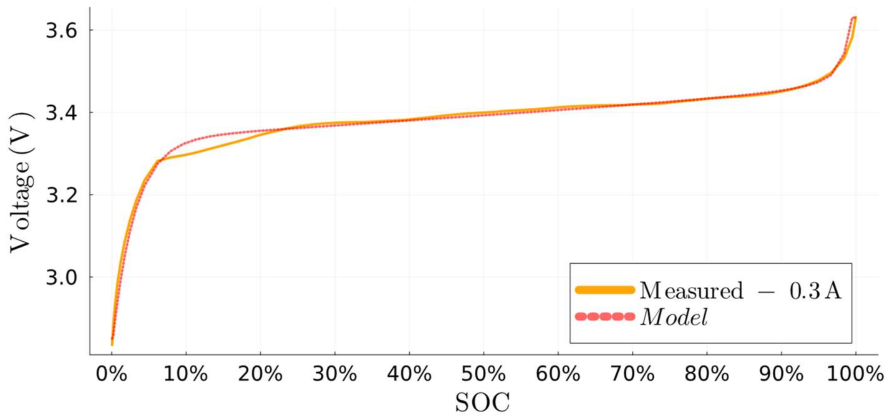

Figure 3.17 - Model fit for the charge

We can verify that the modeled a_0 fits with the linear trend:

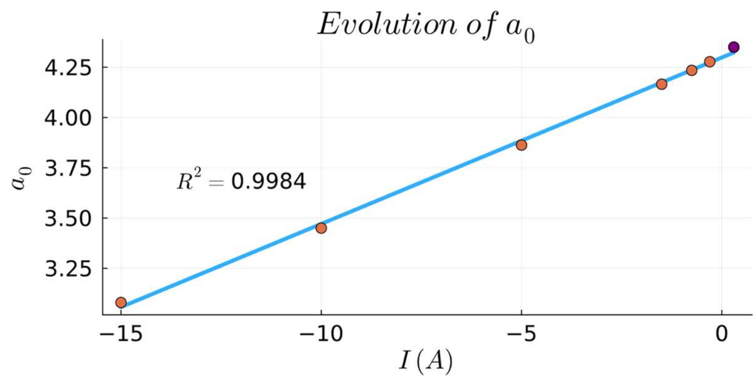

Figure 3.18 - a0 linear trend generalization

Using the model presented in the previous section, the evolution of the different coefficient for the charging process can be extrapolated as:

$$\begin{cases} a_0(I) = 4.2983 + 0.0827 * \mathrm{I} \\ a_1 = -0.0015 \\ a_2(I) = -0.4979 - 0.0401 * \mathrm{I} \\ a_{3(I)} = 26 - \mathrm{e}^{-I+1.553} \end{cases} \tag{3.19}$$

The model for different charging rates gives the following results (the charge cut-off is at 3.65V, as usual for an LFP battery):

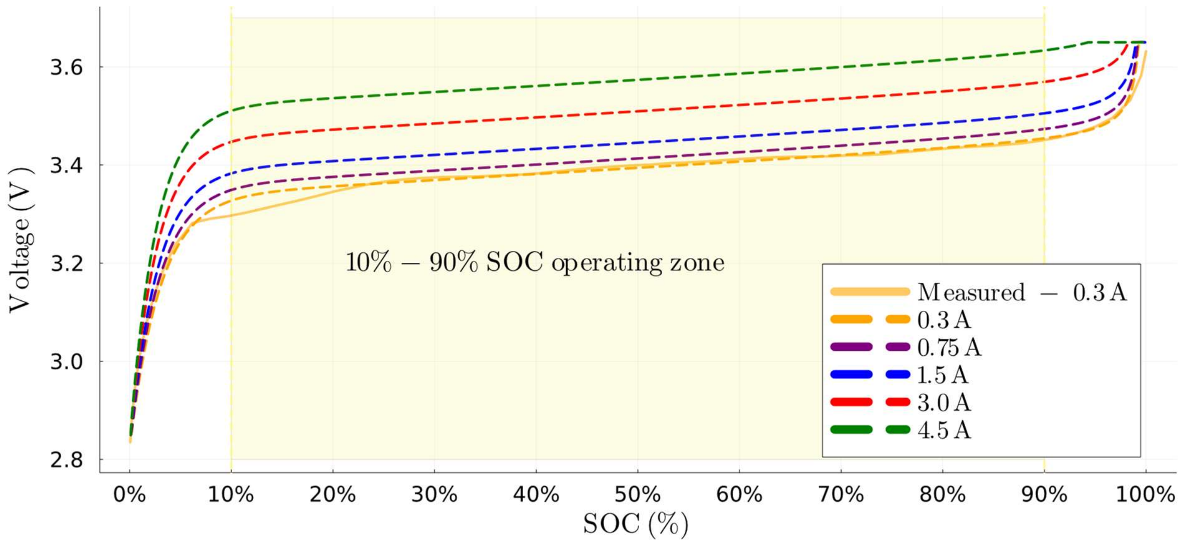

Figure 3.19 - Battery's model for different charging rates

It is important to note that the model is not valid for high charging currents. The overall evolution of the current can be represented here:

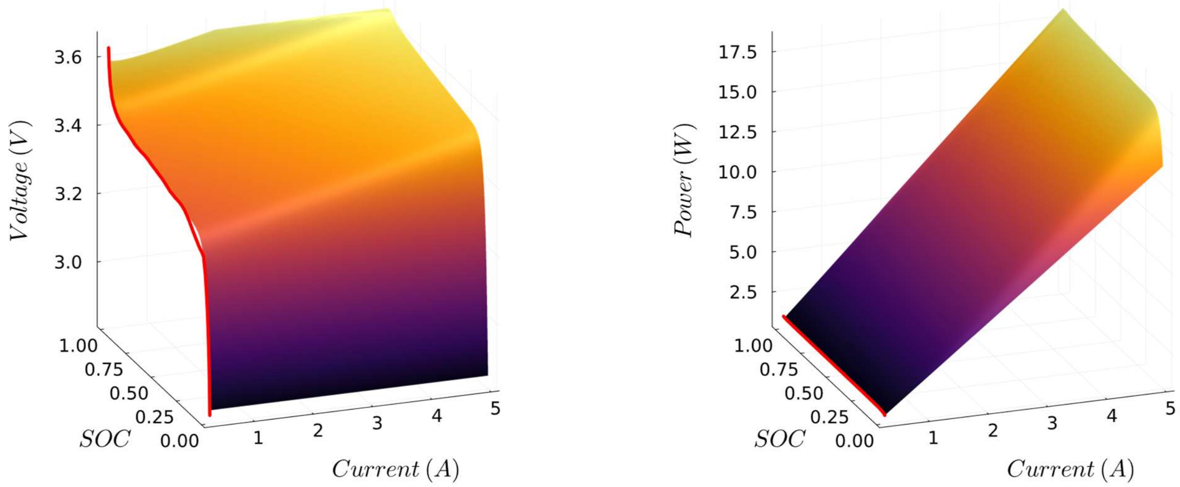

Figure 3.20 - Battery's voltage and power evolution as a function of SOC and current during the charging phase

3.4.5 Capacity evolution

From the experimental data, we obtain a reference capacity C_{ref}=1.57 Ah, which is consistent with the nominal capacity provided of 1.5 Ah. The fitted Peukert exponent is k=1.0163, which is consistent with the expected value.

The evolution of capacity during the charge and discharge phases is similar (Zhang et al., 2025).

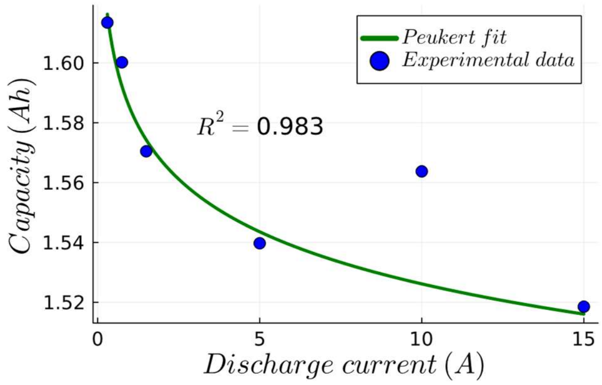

Figure 3.21- Peukert's law coefficient fitting

3.4.6 From steady state to dynamic behavior

To validate the dynamic behavior of the battery, we can first rely on experimental data made available by the University of Maryland from an LFP cylindrical 26650 cell with a rated capacity of 1.1Ah and nominal voltage of 3.3 V. (Xing et al., 2014). Figure 3.22 shows the behavior of the battery when exposed to different charging and discharging currents.

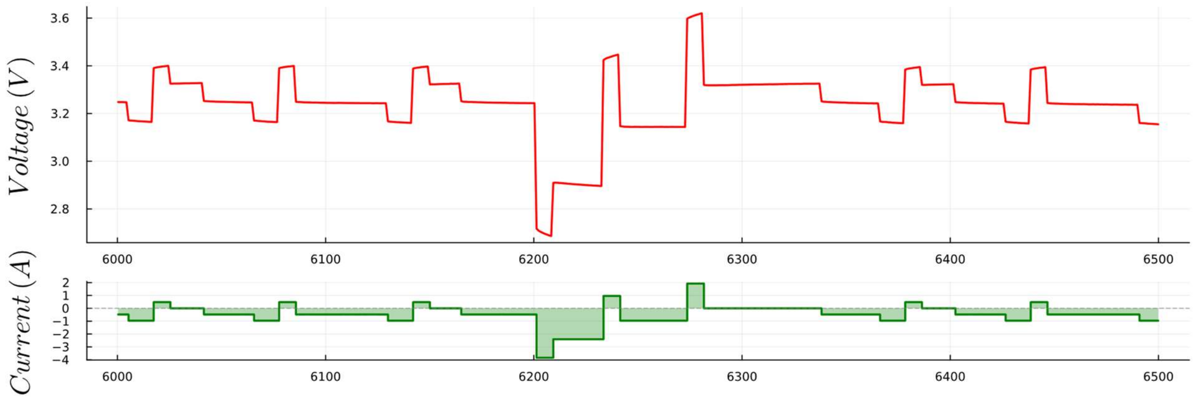

Figure 3.22 - Dynamic data

The different operating points from the dataset have been extracted and plotted in Figure 3.23. The resulting discharge and charge trajectories display a very similar shape to a typical datasheet curve. This means that curve from a datasheet can be turned into a dynamic model.

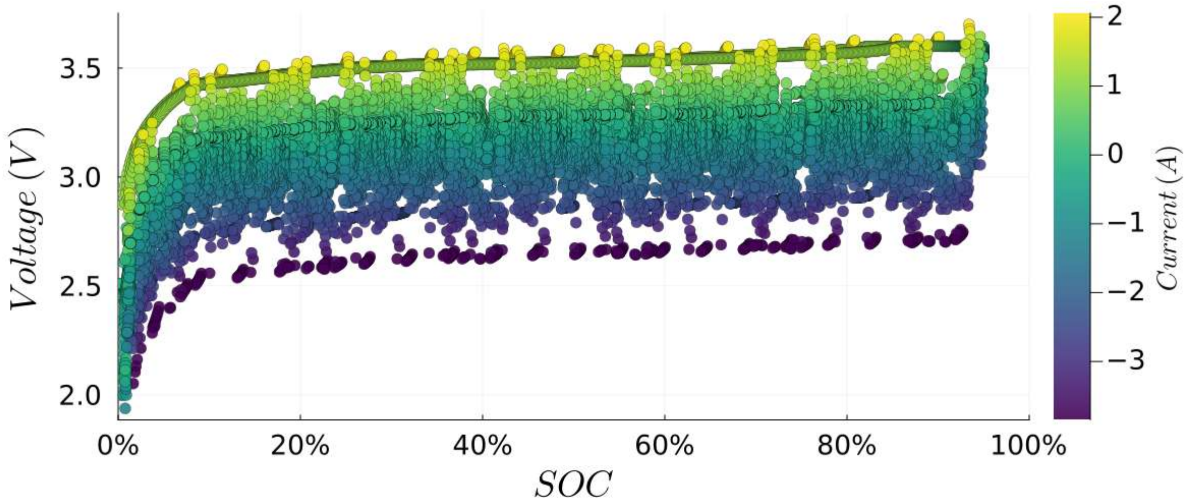

Figure 3.23 - Battery operating points

Additionally, data from the Haydarzadeh & Toivoila study (2024) are used to validate the exponential approach. This dataset provides experimental results from lithium-ion cells subjected to a randomized usage profile and periodically evaluated through diagnostic tests. The study involved eight cells from three different chemistries (NMC, NCA, LFP), which were tested over more than 660 full charge–discharge cycles. Health evaluation cycles were conducted regurlaly at 1C and 2C by using a series of constant current pulses as shown on Figure 3.24

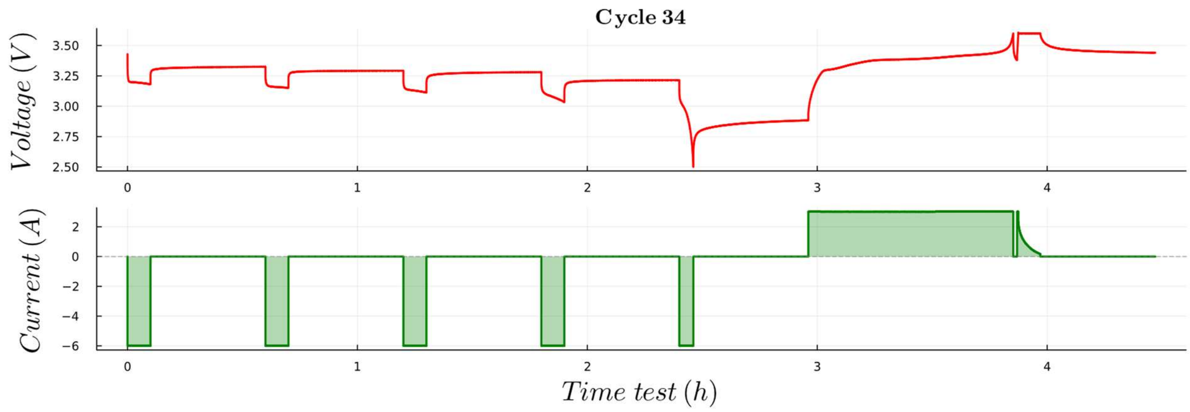

Figure 3.24 - Health evaluation cycle at 2C

To better visualize the exponential approach, we can concatenate the individual current pulses to reconstruct full discharge cycles. The color evolution represents the cycle number through time.

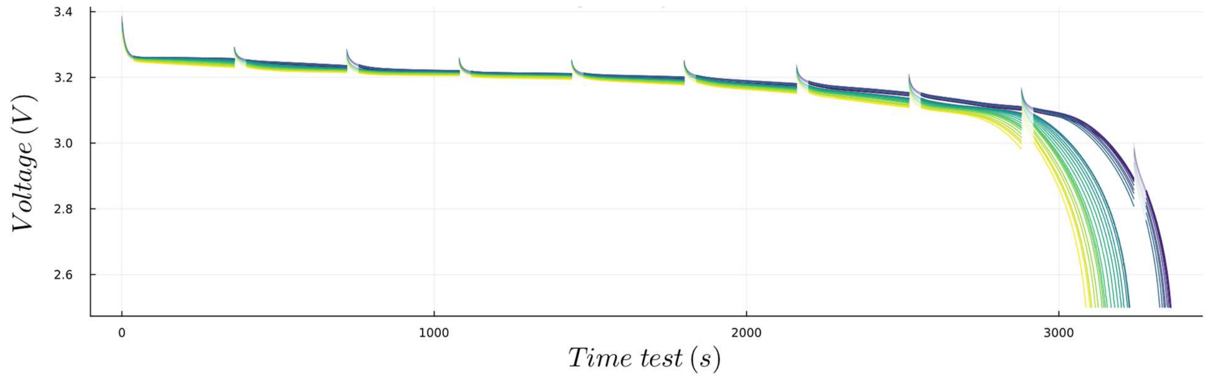

Figure 3.25 - Concatenetad 1C pulsation until discharge

This reconstruction highlights a transient response when the cell transitions from a resting state to an active operating one. The voltage response exhibits a characteristic exponential evolution, which can be modeled as presented in Eq. 3.20. This formulation ensures that the voltage starts at the correct initial value and converges smoothly to the final steady-state voltage as observed experimentally

$$V_{bat}(t) = V_{initial} + (V_{end} - V_{initial}) * (1 - e^{-t/\tau}) \tag{3.20}$$

3.5 Complete battery dynamic model

The work from sections 3.2.2 and 3.4 leads to the model summarized on Figure 3.26. It combines the information from the 3D charging and discharging map from section 3.4.2 and 3.4.4 with an exponential transit phase. The model operates through the following computational workflow:

1. For a given operating point, the target voltage V_{end} is retrieved from the 3D map as a function of the instantaneous SOC and the imposed current or power.
2. The effective battery capacity $C_{eff}(I)$ is evaluated using Peukert's law, relying on the fitted parameters identified in section 3.4.5.
3. The transition between operating points is modeled by a first-order exponential relaxation, as described in section 3.4.6, with a time constant fixed at $\tau = 10$ s.

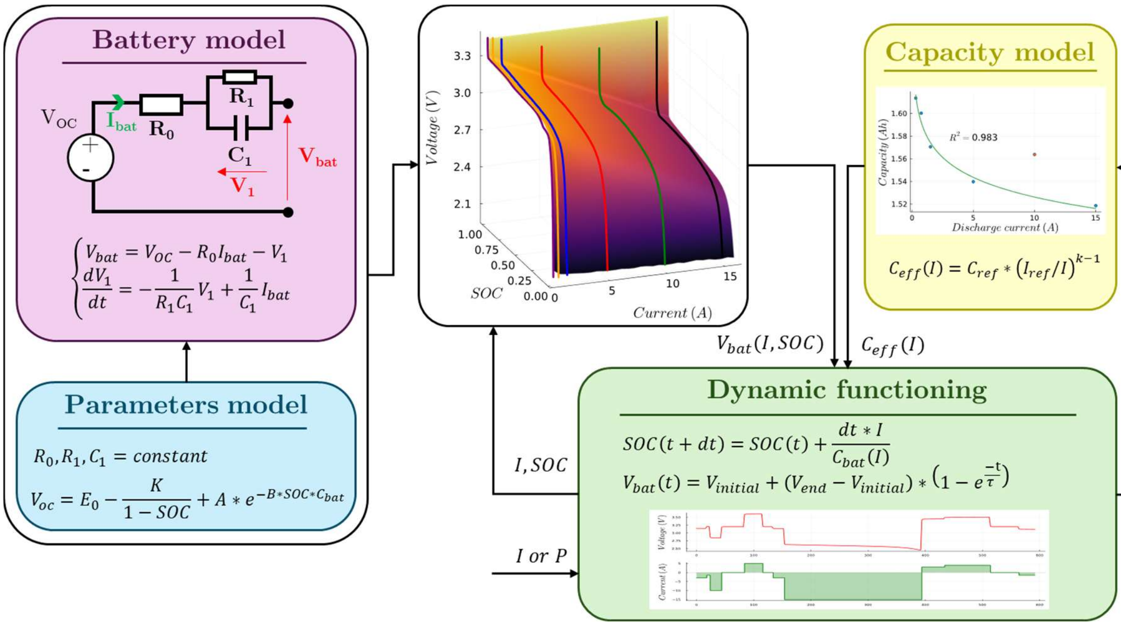

Figure 3.26 - Dynamic battery model presentation

Figure 3.27 presents an illustrative dynamic operating profile consisting of a sequence of charge and discharge phases with variable current levels.

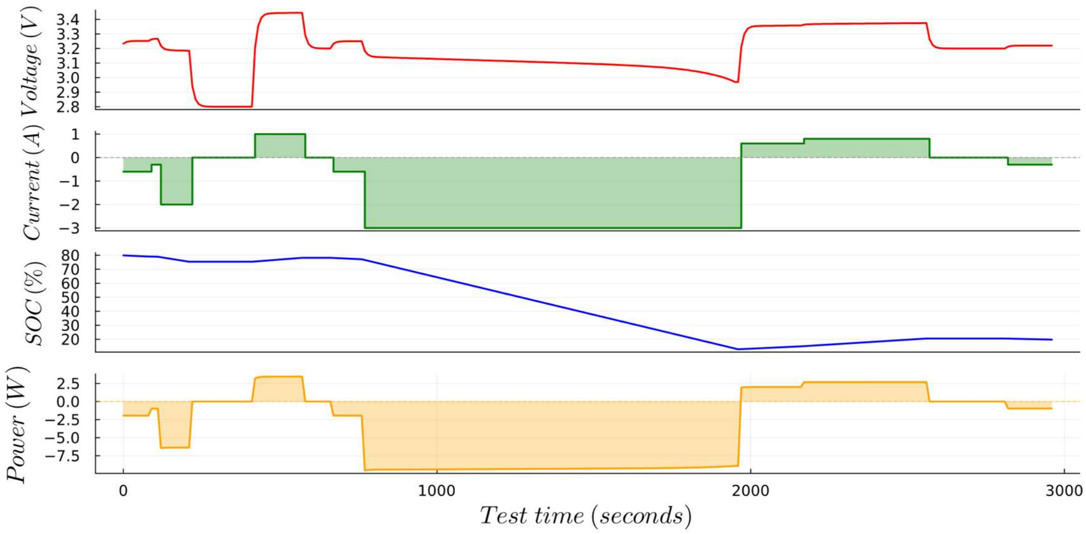

Figure 3.27 - Proposed dynamic battery model results

3.6 Generic model

3.6.1 Cross-cell validation

To assess the generalization capability of the proposed approach, the model was then applied to the additional selected commercial LFP cylindrical cells presented in section 3.2.2. For each cell, the Shepherd coefficients *a0*, *a1*, *a2*, and *a3*, and the dynamic branch elements R_0, R_1 and C_1 were fitted following the methodology described in Sections 3.4.2 and 3.4.3.

The evolution of the fitted Shepherd coefficients as a function of the C-rate is show in Figure 3.28, revealing that all six cells exhibit the same dependence on current, despite differences in capacity, design, and manufacturer origin. This confirms that while the numerical values of the parameters themselves may vary, the model structure remains valid.

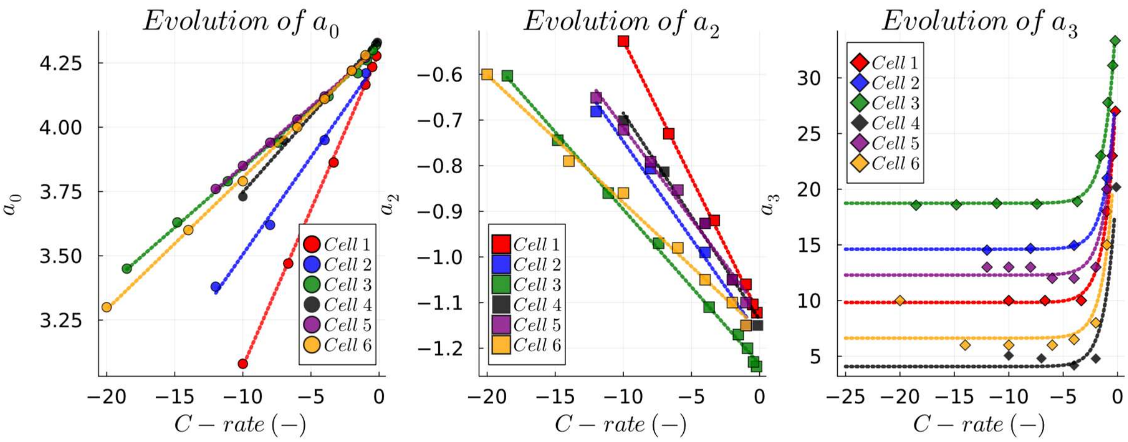

Figure 3.28 - a0, a2, and a3 evolution comparison across six commercial cells

The numerical parameters of the fitted models are summarized in Table 3.9, as well as the MAE between the modeled voltage response and the datasheet provided ones across all fitted C-rates. These results confirm that the method can be reliably applied to any commercial LFP cell.

Table 3.9 – numerical values of the model coefficients

Cell n°	a0	a1	a2	a3	R1	C1	MAE
1	4.289 + 0.122*C	-0.0004	-1.13 – 0.06*C	$e^{C+3.06} + 9.83$	10	12	24 mV
2	4.262 + 0.076*C	-0.0004	-1.17 – 0.042*C	$e^{C+2.81} + 14.61$	10	9	26.2 mV
3	4.304 + 0.046*C	-0.0006	-1.23 – 0.033*C	$e^{C+2.95} + 18.74$	10	10	35.1 mV
4	4.344 + 0.059*C	-0.0003	-1.13 – 0.045*C	$e^{C+2.89} + 4.08$	10	12	27.4 mV
5	4.311 + 0.046*C	-0.0003	-1.11 – 0.040*C	$e^{C+2.94} + 12.9$	10	5.5	22.6 mV
6	4.318 + 0.051*C	-0.0006	-1.16 – 0.028*C	$e^{C+3.05} + 6.63$	10	14	31.1 mV

3.6.2 Proposed reference cell for early-stage simulation

Based on the analysis conducted in the previous section, we propose a generic LFP cell model for early design and simulation tools based on average cell properties. The objective of this reference model is to provide a realistic but datasheet-independent voltage response representative of commercial LFP cells.

A model for an LFP cell is presented in Eq. 3.21 for the discharge and Eq. 3.22 for the charge.

$$\begin{cases} a_0(C) = 4.3 + 3.2 * \mathrm{R_0} * \mathrm{C} \\ a_1 = -\ 0.0005 \\ a_2(C) = -0.6 * \mathrm{a_0} + 1.4 \\ a_3(C) = \mathrm{e}^{C+3} + 21 - 6 * C_{nom} \end{cases} \quad 3.21$$

$$\begin{cases} a_0(C) = 4.3 + 3.2 * \mathrm{R_0} * \mathrm{C} \\ a_1 = -\ 0.0010 \\ a_2(C) = -0.6 * \mathrm{a_0} + 1.4 + \Delta V_{cut-off} \\ a_3(C) = \mathrm{e}^{-C+3} + 42 - 12 * C_{nom} \end{cases} \quad 3.22$$

As an illustrative example, the parameters presented in Table 3.10 may be used.

Table 3.10 -Example parameters

Capacity	C_1	R_0	R_1	$V_{cut-off,dis}$	$V_{cut-off,ch}$
1.5 Ah	10F	17 mΩ	10Ω	2.0 V	2.3 V

The resulting voltage profiles under several charge and discharge C-rates are illustrated in Figure 3.29. To adapt the model to the desired capacity, series of n cells can be considered. The resulting power is then n-times the nominal one.

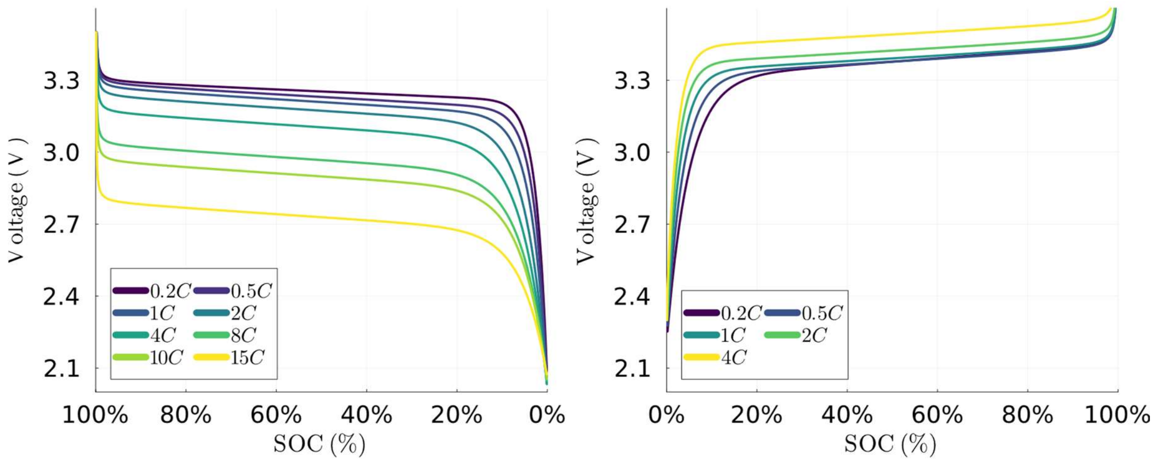

Figure 3.29 - Voltage response of the proposed generic LFP cell under various discharge (left) and charge (right) C-rates

3.7 Battery aging model

The dynamic battery model developed in the previous sections captures short-term electrical behavior but does not account for long-term degradation. This section introduces the battery aging model adopted in this work, with a focus on capacity fade. The aging model of the battery is divided into two sections: calendar and cyclic degradations. Additionally, two impacts of aging are considered in each case: the capacity and then the resistance degradation of the battery.

3.7.1 Calendar aging

Calendar aging refers to the degradation of a battery that occurs over time when it is not actively cycled. It is mainly driven by storage conditions, particularly temperature and SOC, and results in capacity loss and increased internal resistance. Those two aspects are addressed in the following sections.

3.7.1.1 Proposed model

Capacity degradation

To model the calendar degradation of the capacity, the model presented in Sarasketa-Zabala et al. work (2014) is used. It describes the capacity fade as a decreasing exponential function of time and SOC storage:

$$C_{remaining}(\%) = 100 - e^{a} * t^{b} \qquad 3.23$$

With t in years and $C_{remaining}$ in %. To generalize the model and extend it to any resting SOC, parameters a and b are modeled as linear function of SOC (Saldaña et al., 2022).

To dynamically evaluate the capacity fade induced by calendar aging, the time spent at constant SOC is discretized into segments during which the current and the state of charge can be assumed constant. For each interval of duration Δt, the incremental capacity loss ΔC (in %) is computed and added to the previously accumulated degradation (Sarasketa-Zabala et al., 2014).

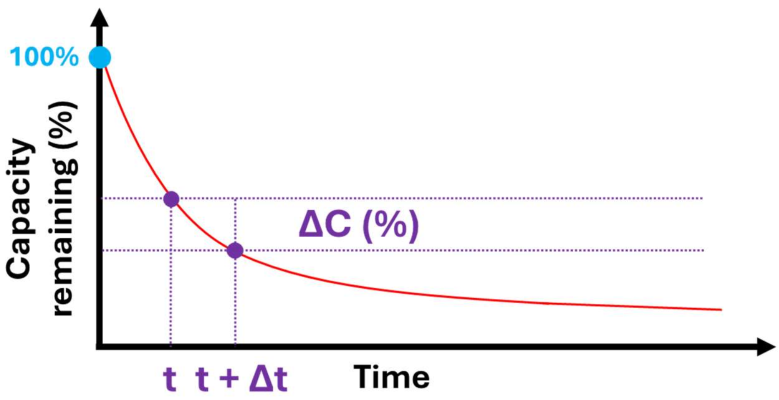

Figure 3.30 - Voltage degradation dynamic computing

ΔC can be calculated as:

$$\Delta C = a(SOC) * [(t + \Delta t)^{b(SOC)} - t^{b(SOC)})] \quad 3.24$$

Where t is the total amount of time spent resting at $I_{bat} = 0$. Finally:

$$C_{degradation}(t) = \sum_{\Delta t} \Delta C(\Delta t, SOC) \quad 3.25$$

Resistance degradation

Voltage degradation can also be observed as a consequence of calendar aging due to the resistance degradation (Saldaña et al., 2022). This effect becomes more pronounced at higher SOC storage and under elevated current conditions.

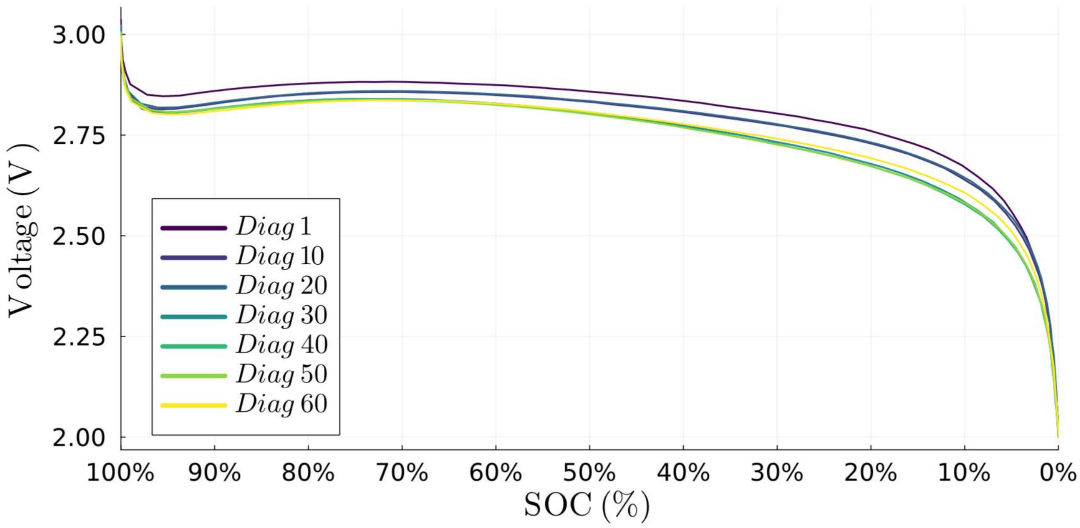

Figure 3.31 - Voltage degradation over time, $SOC_{storage}$= 100%, I = 3C

To capture this evolution, the degradation is modeled as a multiplicative factor $a^* < 1$ applied to the original voltage profile, coupled with a second factor reproducing the higher drop at lower SOC.

$$V(t) = a^*(\mathrm{t}) * V_{initial} - \frac{b^*(t)}{SOC} \quad 3.26$$

3.7.1.2 Data analysis and model fitting

Capacity degradation

The data from Lam et al. (2025) include a data set of LFP battery that were left idling for 8 years, only undergoing 67 cycles to assess calendar aging. The gradual degradation of the battery capacity can be observed on Figure 3.32. On the next figures, each dot represents a health checkup performed on the battery at regular intervals of times.

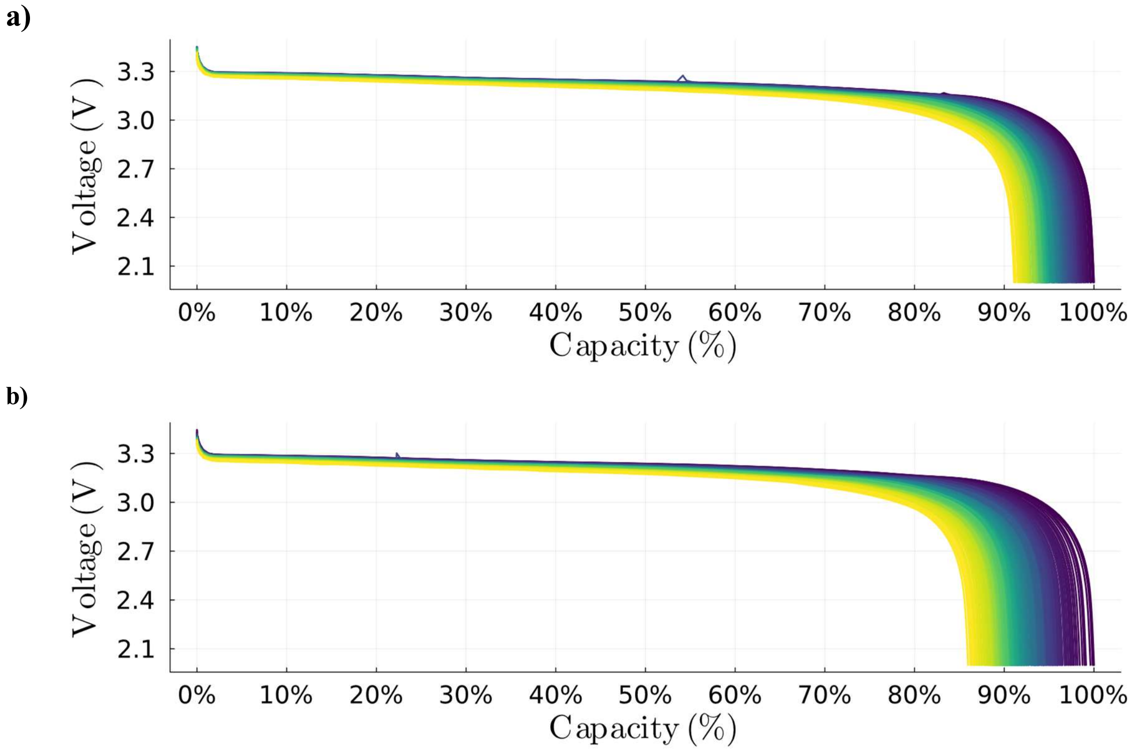

Figure 3.32 - LFP battery capacity degradation for different current and SOC storage: a) is $SOC_{storage} = 50\ \%, I_{dis} = 0.2C$ and b) is $SOC_{storage} = 100\ \%, I_{dis} = 0.2C$

The observed evolution, presented in Figure 3.33, shows that, for a given current rate, the capacity fade follows a very similar trend during both charging and discharging. This indicates that the degradation mechanism is primarily governed by the current intensity rather than the mode of operation.

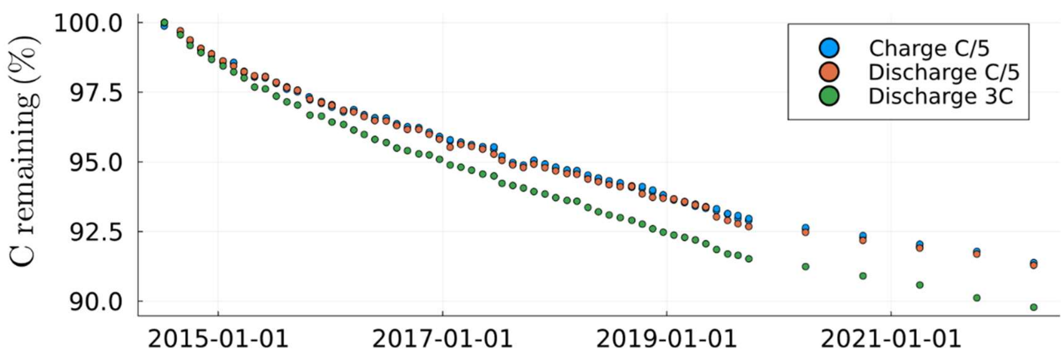

Figure 3.33 - Capacity degradation over time

We can also see that the degradation increases with the SOC and the current rates, as shown on Figure 3.34.

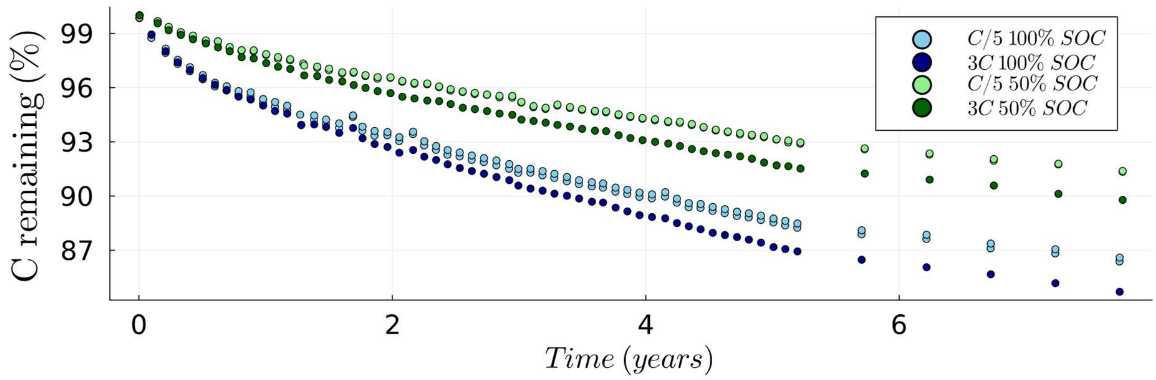

Figure 3.34 - Capacity degradation for different current rates and SOC

The fitted model results from last section are presented in Figure 3.35.

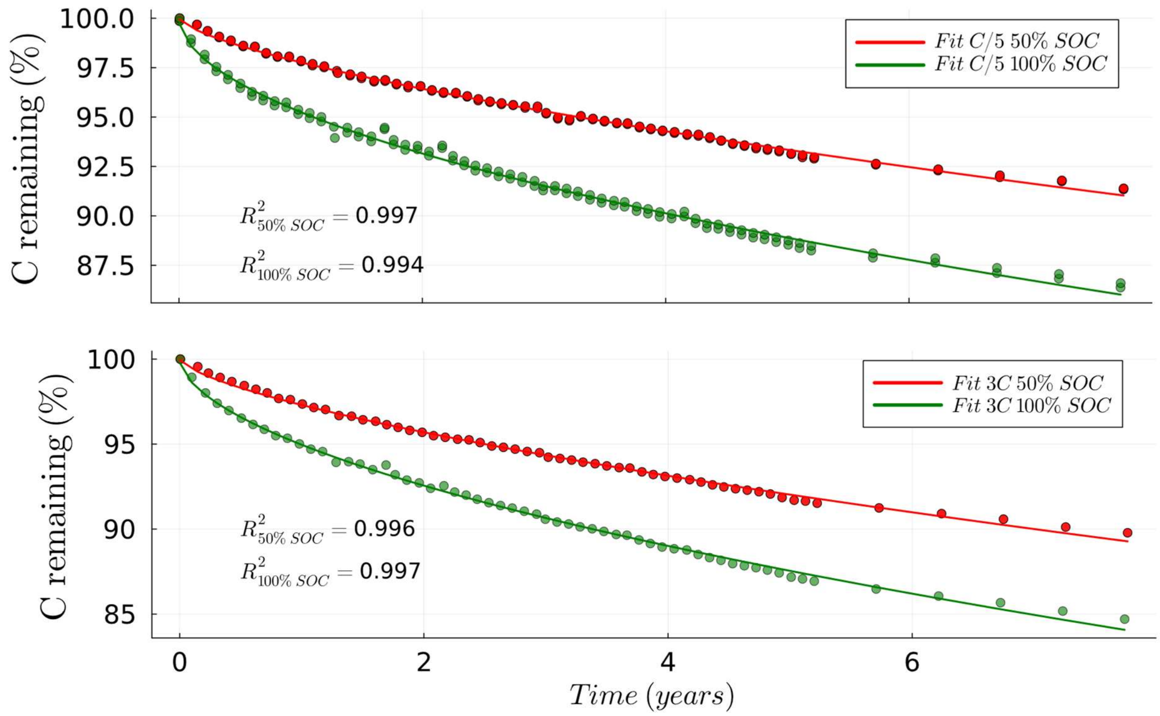

Figure 3.35 - Capacity degradation fitted model

The fitted parameters are summarized Table 3.11. We observe that the values of parameter a are similar for both current rates (C/5 and 3C), varying only with the SOC storage value. On the other hand, b evolves with both the applied current and the SOC.

Table 3.11 – Fitted parameters

		a	b	R^2
C/5	50% SOC	0.901	0.631	0.997
	100% SOC	1.557	0.504	0.994
3C	50% SOC	0.897	0.704	0.996
	100% SOC	1.587	0.571	0.997

With the two SOC models, a linear relationship can be estimated between a, b and SOC.

$$\begin{cases} a(SOC) = 0.2 + 1.5 * SOC \\ b(SOC) = 0.83 - 0.14 * SOC, \quad I = 3C \\ b(SOC) = 0.77 - 0.14 * SOC, \quad I = C/5 \end{cases} \tag{3.27}$$

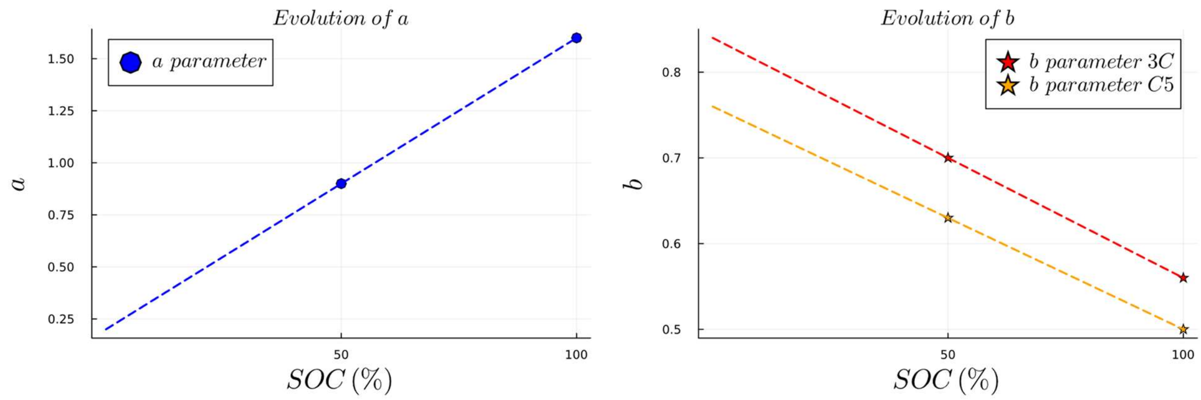

Figure 3.36 - Capacity calendar aging fitted coefficient

In conclusion, the calendar aging model is summarized as:

$$C_{degradation}(SOC, t)[\%] = e^{0.2+1.5*SOC} * t^{0.77-0.14*SOC} \tag{3.28}$$

Resistance degradation

To fit the resistance degradation model to the data, coefficients a^* and b^* are adjusted by fitting the first diagnostic to the 10th, … until the 60th. On Figure 3.37, only the adjusted 1st and the 60th cycle are illustrated.

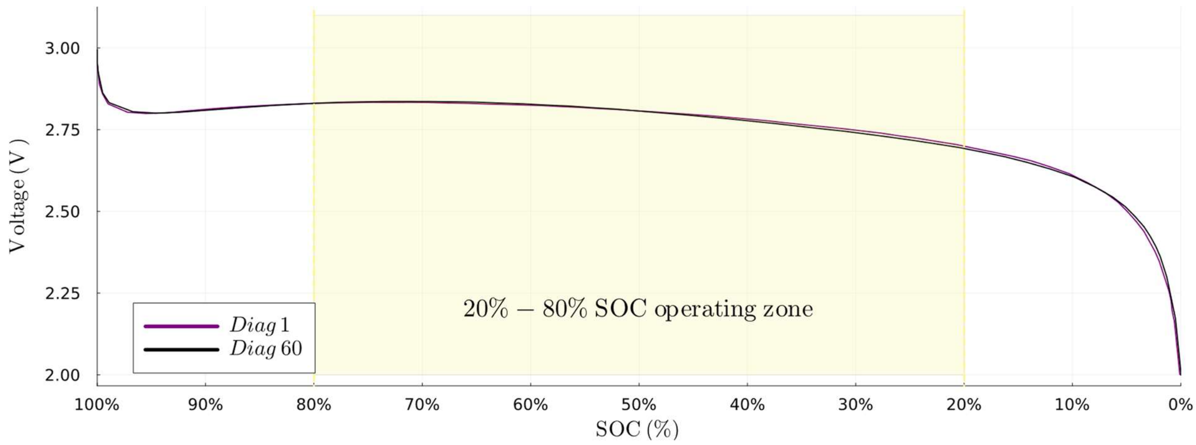

Figure 3.37 - Calendar aging model – comparison between diagnostic 60 and the applied model to diagnostic 1

As presented on Figure 3.37, the model reproduces both the global voltage shift and the accelerated drop at low SOC. The different parameters obtained by fitting diagnostics 1, 10, 20, … up to 60 are summarized in Table 3.12.

Table 3.12 - Calendar aging model parameters

Parameter		1	10	20	30	40	50	60
I=3C	a^*	1	0.991	0.989	0.988	0.988	0.988	0.988
SOC=100%	b^*	0	0.003	0.001	0.009	0.011	0.012	0.006
I=3C	a^*	1	1	1	1	0.999	0.998	0.997
SOC=50%	b^*	0	0.001	0.003	0.012	0.012	0.012	0.013
I=C/5	a^*	1	1	1	1	1	1	1
SOC=100%	b^*	1	0.001	0.001	0.003	0.003	0.004	0.004
I=C/5	a^*	1	1	1	1	1	1	1
SOC=50%	b^*	1	0.001	0.001	0.003	0.003	0.004	0.004

Overall, the evolution of the different coefficients is presented in Figure 3.38. We can see that coeffcient a^* (which represents the voltage drop degradation) follows the typical degradation in t^x, whereas coefficient b^* exhibits an S-shaped evolution.

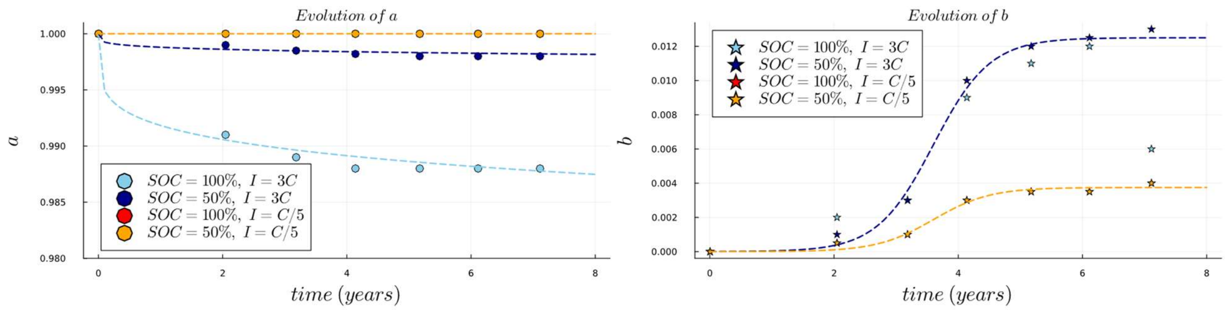

Figure 3.38 - Voltage calendar aging model coefficient

Each coefficient can be modeled with the following formula:

$$\begin{cases} a^* = 1 - \mathrm{a}_1 * t^{a_2} \\ b^* = \dfrac{b_1}{1 + e^{-\mathrm{b}_2(t-\mathrm{b}_3)}} \end{cases} \qquad 3.29$$

For coefficient b, we can see that the SOC storage level has no impact on the degradation, it is only dependent on the current imposed.

Additionally, the parameters b_2 and b_3 are constant as the turning point is around 3.5 years each time. Since the model is based on only two available data points, the evolution of coefficient b_1 can only be considered linear, with a clear correlation to the applied current. Consequently, the expression for parameter b is formulated as:

$$b^*(I,t) = \frac{0.00316 + 0.00212 * \mathrm{I}}{1 + e^{-2.2(t-3.5)}} \qquad 3.30$$

Where t is the cumulative time spent at I=0. The evolution of the parameters a depends on both the current and the SOC storage. The different model parameters are equal to:

Table 3.13 - Calendar aging model parameters

Conditions		a_1	a_2
I=3C	SOC=100%	$8.16*10^{-3}$	0.205
	SOC=50%	$1.11*10^{-3}$	0.205
I=C/5	SOC=100%	0	-
	SOC=50%	0	-

As we can see, y is not a function of the SOC whereas x depends on both the SOC and the current.

Parameter a_1 follows an exponential trend, and if we model it with αC^{β} we find that coefficient α for the SOC=100% curve is 8 times superior to the one for SOC=50%. This leads us to model parameters a with the following equation:

$$\mathrm{a}_1 = SOC_{rest}^3 * 5.3 * 10^{-5} * I^{3.35} \qquad 3.31$$

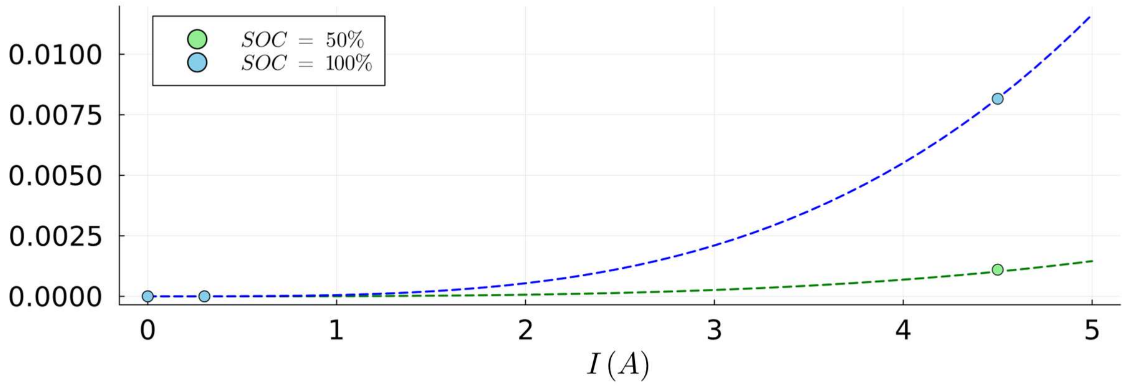

Figure 3.39 - a_1 model parameters

a_2 appears in an exponential term. It means that if its value is too large, the degradation will occur too rapidly. Thus, it is kept constant at 0.205. Finally:

$$a^* = 1 - SOC_{rest}^3 * 5.3 * 10^{-5} * t^{0.205} * I^{3.35} \quad 3.32$$

The dynamic computation of parameter a will be performed in the same way as ΔC, meaning that we update a on short interval of time dt where the SOC storage is constant such as:

$$a^*(I,t) = 1 - t * \Delta\alpha * I^{3.35} \quad 3.33$$

Where:

$$\Delta\alpha = SOC_{rest}^3 * 5.3 * 10^{-5} * [(t+dt)^{0.205} - t^{0.205}] \quad 3.34$$

To analyze the importance of modeling the resistance degradation, we can study the evolution of the state of health in terms of energy extracted from the cell over a complete cycle.

To that end we can compare two values in Figure 3.40:

$$SOH_{capacity} = \frac{C_{bat}^{t}}{C_{bat}^{ini}}$$
$$SOH_{energy} = \frac{\int_{SOC=1}^{SOC=0} V_{bat,ini} * I * dt}{\int_{SOC=1}^{SOC=0} V_{bat} * I * dt} \quad 3.35$$

The dark diamonds points correspond to SOH_{energy}, while the lighter circle ones represent a $SOH_{capacity}$.

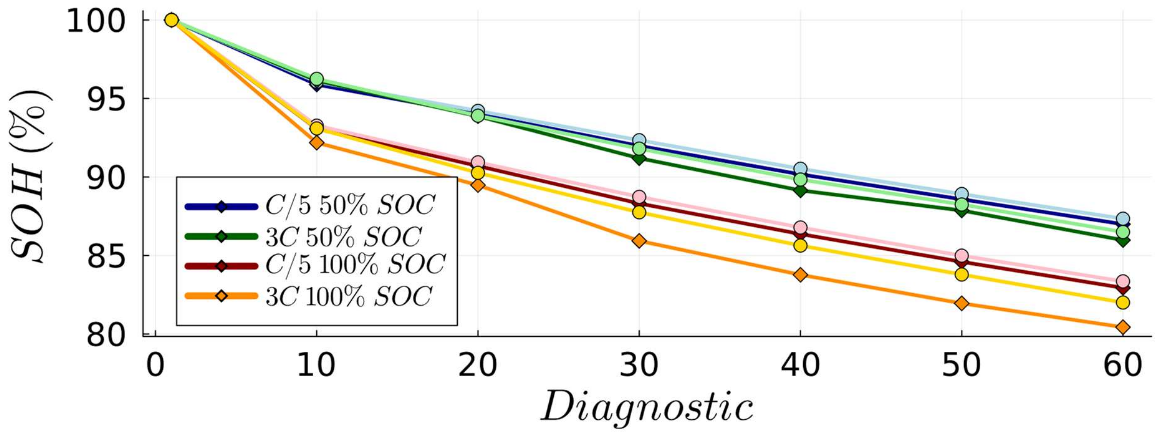

Figure 3.40 - SOH evolution due to calendar aging

The differences between the two models are for each dataset:

Table 3.14 – Absolute differences between SOH_{energy} and $SOH_{capacity}$

C/5, SOC = 50%	3C, SOC = 50%	C/5, SOC = 100%	3C, SOC = 50%
0.35 %	0.51 %	0.41 %	1.56 %

We can then see that the resistance degradation due to calendar aging has little effect on the total energy extracted over a cycle for the cells stored at 50% SOC and the one cycled a C/5, even stored at 100% SOC.

Modeling of the resistance degradation is thus important only for high current and high SOC storage level, where the difference cannot be ignored

3.7.2 Cyclic aging

Cyclic aging refers to the degradation of the battery caused by charge and discharge cycling. It is driven by the number of cycles and operating conditions, such as the current rate. Like calendar aging, it results in capacity fade and increased internal resistance.

3.7.2.1 Proposed model

Capacity degradation

The capacity degradation model used is from (Wang et al., 2011). It models the percentage of capacity loss as:

$$C^{*}_{degradation} = A * exp\left[-\frac{E_a}{RT}\right].(Ah)^{z} \quad 3.36$$

Where Ah is the total Ah charged/discharged calculated as $\int |I|.dt$, E_a is the activation energy in J.mol^{-1}, R the gas constant and T the temperature. A key result from this model is that the DOD has very limited influence on capacity fade and can be omitted from the model.

Recent work by Cugnet (2024) shows that A and E_a are respectively quadratic and linear functions of the C-rate.

Resistance degradation

Resistance degradation is also a consequence of cyclic aging. It results in a progressive loss of voltage. To evaluate the importance of resistance degradation due to cyclic degradation, the data from Preger et al. (2020) can be used. In their study, Preger et al. tested LFP battery cells with a capacity of 1.1 Ah. Their cycling protocol consisted of different steps:

- Charge: the cells were always charged at constant current at 0.5C, from 0 % to 100 % SOC
- Discharge: The cells had fixed rates of 0.5C, 1C, 2C, and 3C discharge current rates that remained constant though their different cycles.

Each cell went through at least 3000 cycles, and an example is presented in Figure 3.41.

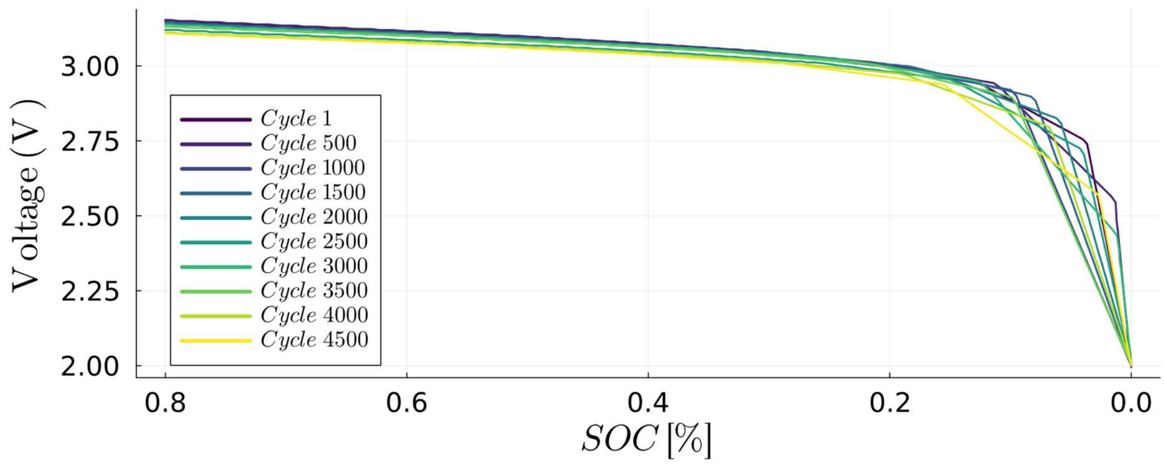

Figure 3.41 – Different cycle example for a discharge rates of 3C

Using the same SOH metrics as in section 3.7.1.2, we can compare the impact of resistance degradation on the SOH evaluation over time (Figure 3.42) . The dark diamonds points correspond to SOH_{energy}, while the lighter circle ones represent a $SOH_{capacity}$.

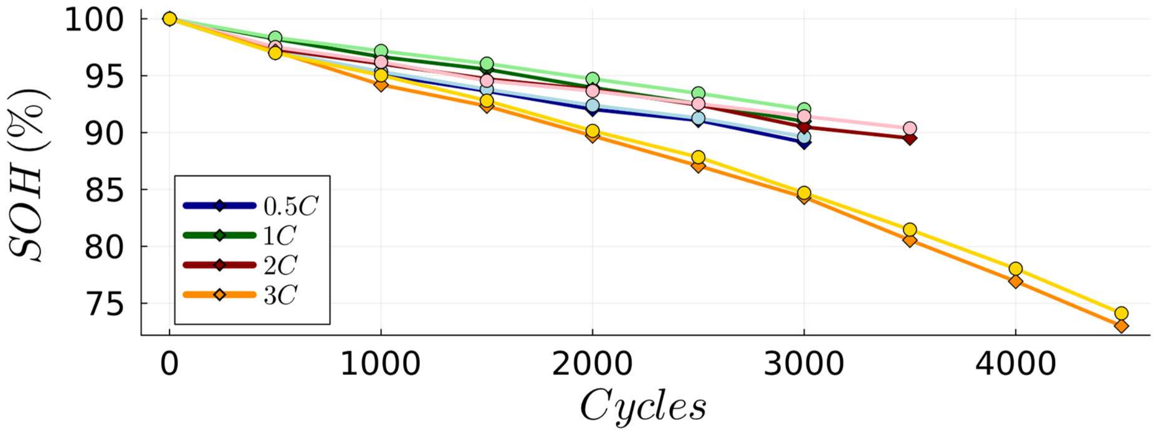

Figure 3.42 - SOH evolution

At the end of the performed cycles, the difference between the real and the approximated SOH is:

Table 3.15 - SOH_{energy} vs $SOH_{capacity}$ comparison

0.5C	1C	2C	3C
-0.47 %	-1.05 %	-0.86%	-1.11%

In the context of BMS for hybrid BESS-PV plants, batteries are rarely cycled at high C-rate. The impact of resistance degradation on SOH being low even after several thousand of cycles, it will therefore be ignored.

3.7.2.2 Data fitting

To fit the capacity degradation model to the cell considered, the datasheet (K2 Energy Solutions, Inc., s. d.b) provides information about the cell cyclic aging for complete 1.5A charge and 3A discharge cycle realized. However, typical BMSs and the selected model use Ah output and input to track cyclic degradation instead of actual cycles, these information were therefore converted in Ah in Figure 3.43.

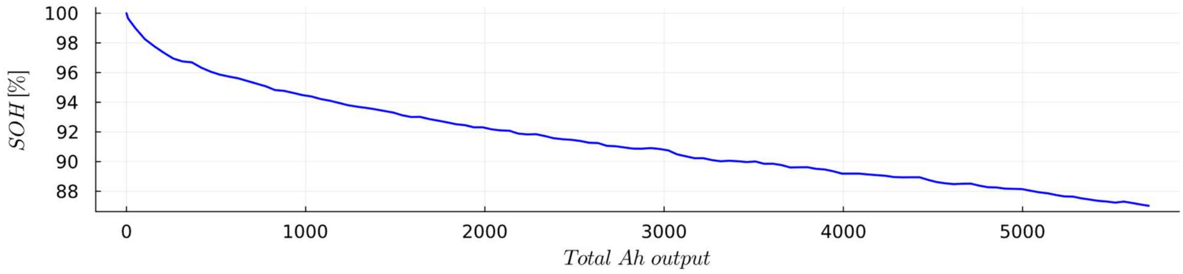

Figure 3.43 -SOH evolution for complete 1.5A charge and 3A discharge cycle, represented as the total Ah output

The activation energies from Wang et al. (2011) model at 1C and 2C were used, as they were obtained for LFP cells similar to the ones considered in this thesis. Additionally, the power law factor z is here equal to 0.5, which is coherent with the value commonly found in the literature.

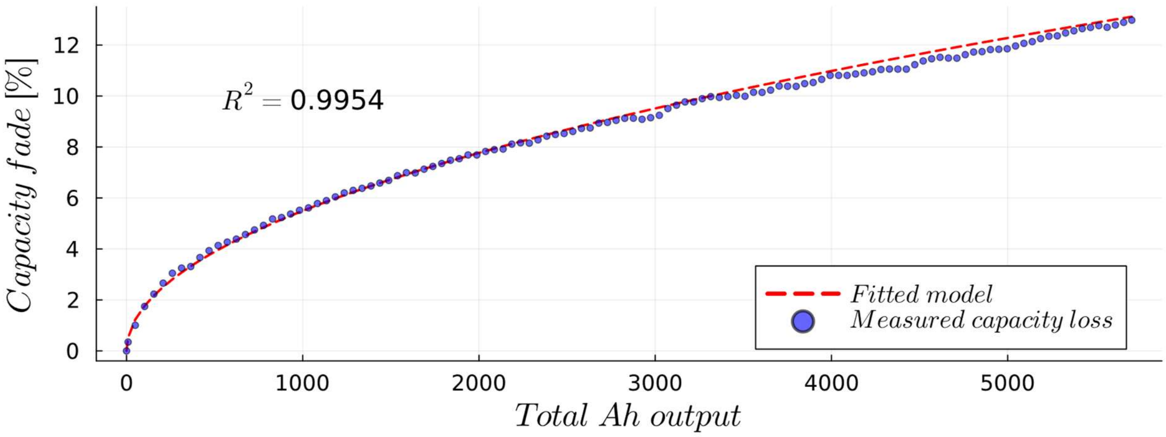

Figure 3.44 -(Wang et al., 2011) model fitted for K2Energy cell

The model can then be generalized with the method proposed by Cugnet (2024):

$$\begin{cases} E_a(C) = -31700 + 370 * C \\ A(C) = 62016 - 10548 * C + 745 * C^2 \end{cases} \quad 3.37$$

The incremental losses obtained for all cycles are then accumulated to determine the total lost capacity, as presented for the calendar aging dynamic computation in 3.7.1.1.

3.8 Conclusion

This chapter presented the development of a battery modeling framework adapted for PV-coupled BESS simulations. A dynamic model based on the commercial lithium-ion cell K218650E was developed and parameterized using experimental data, to ensure realistic voltage response and SOC evolution. Additionally, to address situations where detailed cell information is unavailable, a generic cell model was then proposed for early-stage and system-level simulations.

A complete aging model, separated into calendar and cyclic contributions was integrated into the framework. It was then developed and fitted using experimental data from the same commercial cell. The model addresses the degradation of capacity and resistance due to aging. In the remainder of this work, only capacity degradation is considered. Indeed, in the context of BESS operation, batteries are typically operated at low C-rates (generally below 1C), for which resistance degradation remains limited. As shown by the results presented in the previous sections, the impact of resistance degradation on the SOH evolution under such operating conditions is negligible, remaining below 1 % even after several years of operation. The complete modeling framework is presented on Figure 3.45.

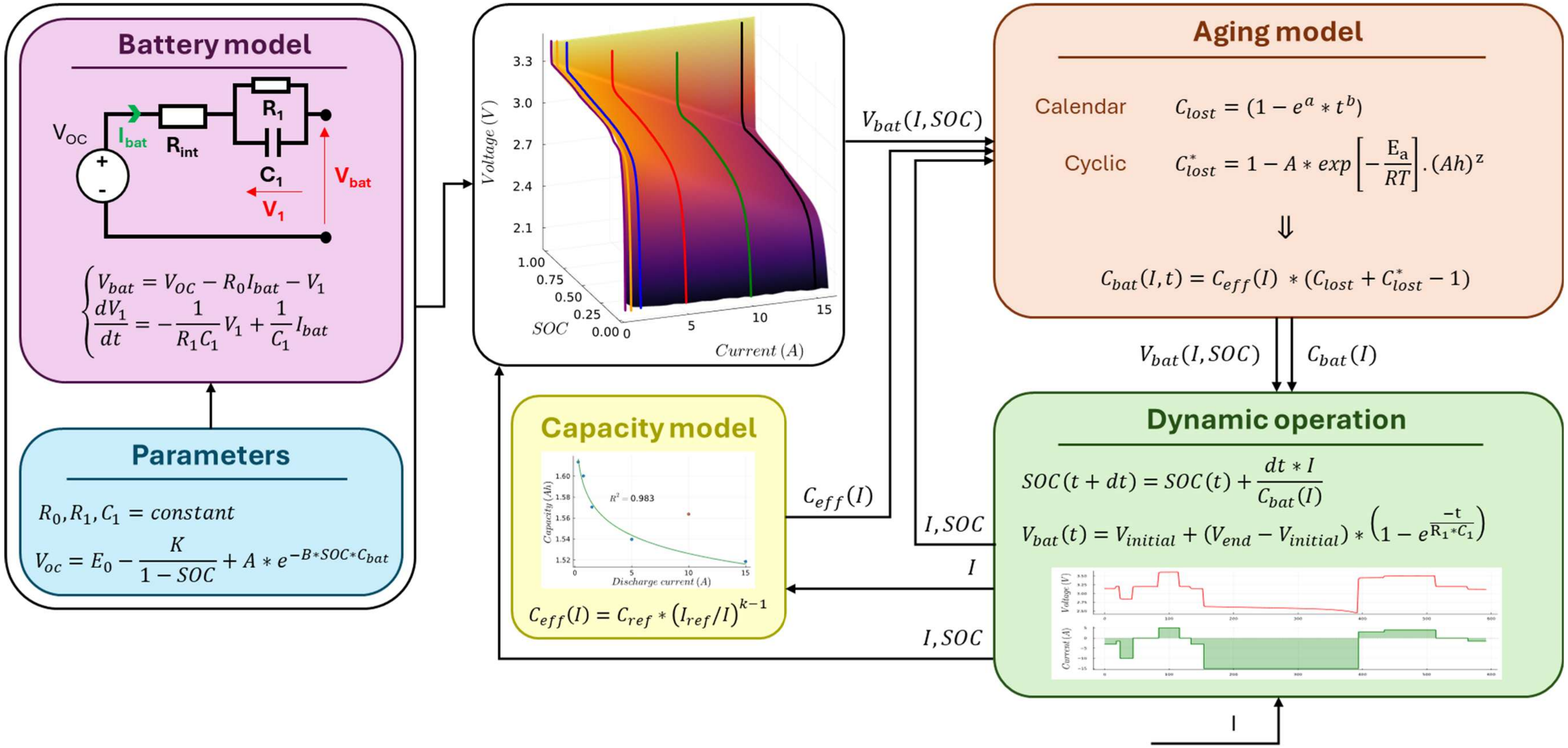

Figure 3.45 -Complete battery model in the context of PV-BESS

CHAPTER 4 GRID INTERACTION

This chapter presents the complete model of the solar power plant with battery energy storage and the assessment of different operational scenarios.

4.1 Literature review

4.1.1 Benefits of battery integration

As renewable energy penetration rates continue to rise, large-scale batteries are becoming indispensable components of photovoltaic systems. Integrating batteries with PV installations enhances grid resilience and power supply reliability by enabling energy storage (Gifford, 2020).

One of the main challenges is the locational mismatch, defined by the IEA as “areas with an abundance of solar and wind resources that are typically far from those where electricity consumption is concentrated, requiring connection through the grid”. Such spatial disparities between generation and consumption centers make the design of efficient grid interconnections and energy storage systems essential (IEA, 2024a).

Studies have shown that flexible PV plants (PV systems augmented with batteries) can be optimally sized to achieve production costs within or below national energy price ranges. For instance, in Italy, such systems could facilitate a renewable energy mix exceeding 90 % by 2060 if implemented correctly (Pierro et al., 2021).

The trend toward decarbonization by integration of renewable energy and storage is being adopted worldwide. In California, policymakers aim to source 100 % of electricity from carbon-free sources by 2045, with grid-scale batteries playing a pivotal role enabling the transition (Plumer & Popovich, 2024). Beyond scientific and policy support, government financial incentives further accelerate battery installations in the United States. The Inflation Reduction Act has encouraged approximately $70 billion in investments in the battery supply chain by offering investment and production tax credits to developers (Medhi & Moherenhout, 2023).

Combining storage and PV systems has three main objectives (Meng et al., 2022):

- Stabilizing the grid by performing peak shaving and displacing the PV production to improve the match with high-demand periods
- Firming solar production by smoothing the generation curve of solar power plants

- Improving financial performance by engaging in energy markets

4.1.2 Grid stabilization

With the increasing integration of renewable energy into the grid, a phenomenon known as the “duck curve” has emerged. The duck curve illustrates the mismatch between solar energy production and electricity demand throughout the day. More specifically, it represents the net load - defined by CAISO as the difference between total electricity demand (the load) and the portion supplied by photovoltaic power and wind energy - on days with high solar energy generation. During midday, when solar production peaks and grid demand is low, the net load drops significantly, only to rise sharply in the evening as solar generation declines and electricity demand increases. When plotted, the resulting curve resembles the shape of a duck (Figure 4.1). (Pitra & Musti, 2021).

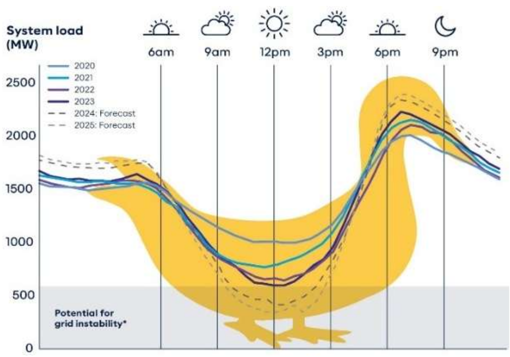

Figure 4.1 - Graphical representation of the 'Duck Curve' in western Australia - (Synergy, 2023)

This phenomenon poses challenges for grid stability. One major concern is the risk of blackouts in the evening when electricity demand rapidly increases, but solar generation is no longer available.

Battery systems are a promising solution to reshape this curve by flattening the PV production. Nguyen Quoc Minh et al. (2023) showed that by adding battery capacity in California, where the solar production is very high, the ramping slope of the net demand in the late afternoon (i.e. the duck curve slope when PV production decreases and demand rises) could be reduced by 60 %. This study is already backed by real data: between 2018 and 2024, California added 13 GW of battery storage capacity (Plumer & Popovich, 2024), which led to a 12 % reduction in the slope of the duck curve in the evening (*Grid Status*, 2025) as illustrated in Figure 4.2.

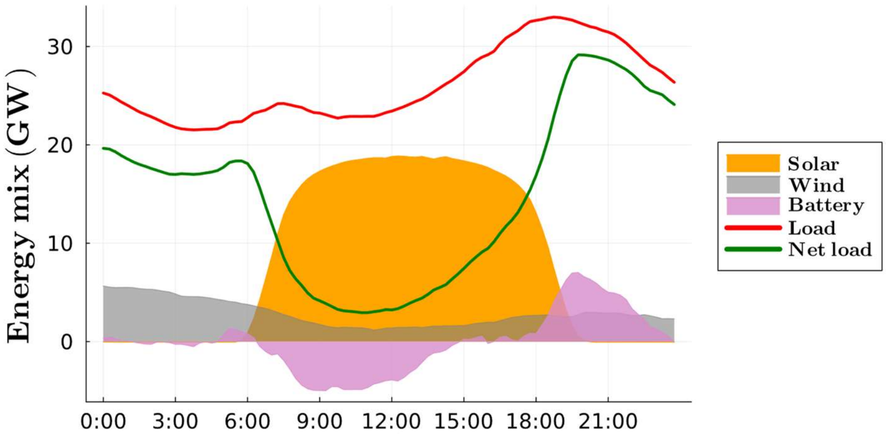

Figure 4.2 - California Independent System Operator energy mix, data from (Grid Status, 2025)[3]

4.1.3 Firming solar production

One of the key challenges of utility-scale solar power plants is their inability to guarantee consistent energy output due to variability in sunlight. Grid-connected PV plants rely on power electronic converters to synchronize with grid frequency and phase. Unlike traditional synchronous generators, these converters lack rotational inertia. When disturbance occurs, it means that PV plants cannot store or release kinetic energy to quickly react and maintain grid stability (Islam et al., 2024).

BESS can firm the solar generation by maintaining a steady energy output regardless of solar irradiation conditions. This increases their reliability and allows PV power plants to meet contractual obligations for energy delivery, making them more attractive to utilities and grid operators (Lo Franco et al., 2021).

4.1.4 Improving financial performance

The integration of BESS can significantly improve the financial performance of solar power plants by enabling them to engage in energy arbitrage and reducing curtailment losses.

Energy arbitrage involves using batteries to store electricity during periods of low prices and selling it during periods of high prices, thereby maximizing revenue. According to the U.S. Energy

[3] Net load in the CAISO region is the total electricity demand minus the generation from variable renewable sources, specifically wind and solar. It represents the demand that dispatchable power must meet.

Information Administration, energy arbitrage was reported as the primary use case for battery storage systems in 2023 (EIA, 2024).

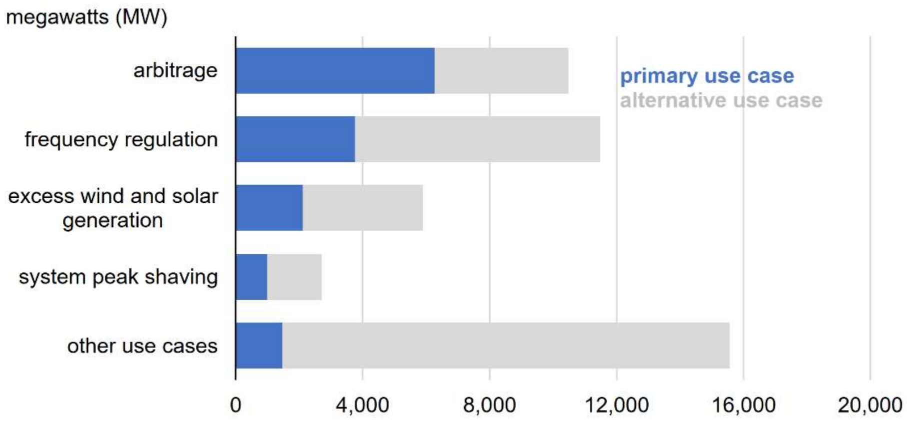

Figure 4.3 - US battery power capacity with reported primary use case in 2023, (EIA, 2024)

The importance of arbitrage is reinforced by the increasing volatility of electricity prices observed over the past decade. As illustrated in Figure 4.4, the probability density functions of electricity prices in California progressively flatten over time, indicating a broader distribution of price outcomes and more frequent extreme values.

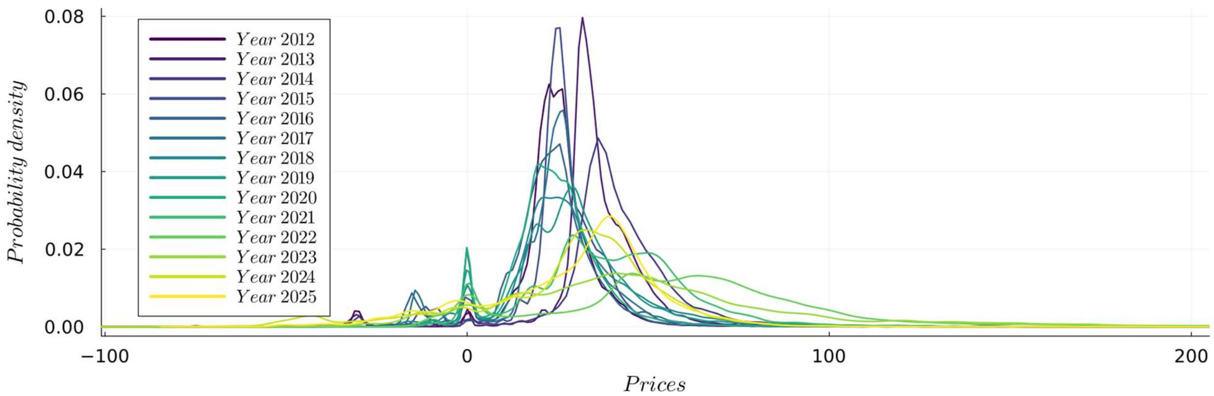

Figure 4.4 – Probability density function of the electricity price over the years in California (EnergyOnline, 2024)

Beyond arbitrage, BESS also plays a critical role in reducing curtailment losses. Curtailment is a common practice in renewable energy production that refers to the shedding of generated energy that cannot be delivered to the grid or consumed due to constraints or limitations in the system. This can represent a significant financial loss for energy producers as solar curtailment is high for most of the year. For example, it represented up to 33 % per week in 2023 for the Western Interconnect - one of the two major power grids in the North American power transmission grid

(Staadecker et al., 2024). Integrating BESS into PV power plants can mitigate curtailment by storing the excess energy instead of discarding it.

4.2 Selected data

4.2.1 Weather and PV data

The meteorological data used to evaluate the solar farm annual production were measured in Las Vegas (36.16909° N, 115.140579° W, UTC–8) (Wilcox & Andreas, 2007).

To determine the optimal geometrical configuration of the PV array, the incident radiation GTI was evaluated for a range of panel tilt angles between 0° and 40°, with a fixed azimuth of 180° (towards south).

As presented in Figure 4.5, the optimal tilted angle for the panel is 30° as it maximizes the irradiation received by the PV panels, and thus their annual production.

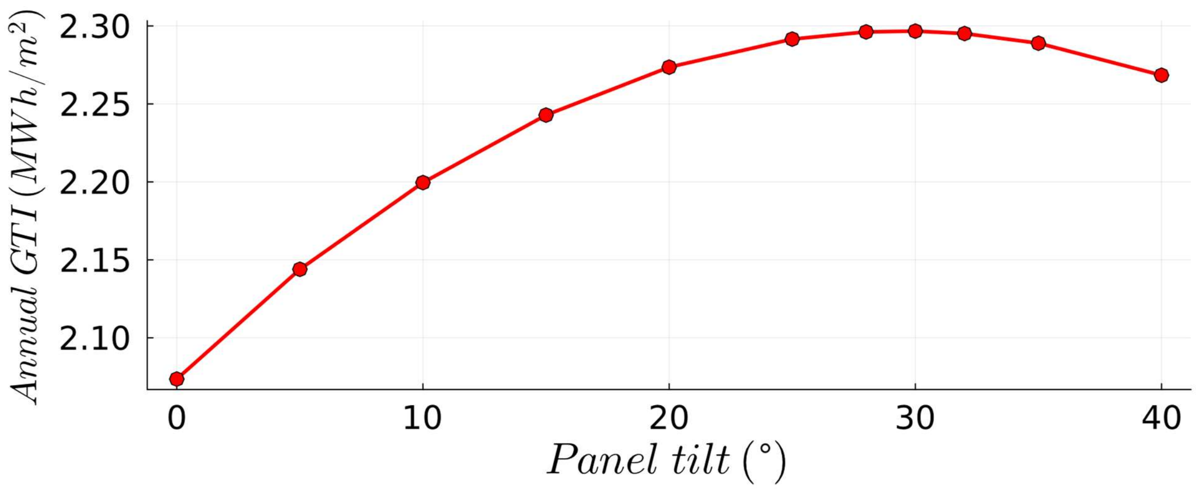

Figure 4.5 - Annual GTI as a function of panel tilt angle at the chosen site

The PV model used to calculate the annual production of the PV panels is then the one previously presented in section 2.1.2.2.

4.2.2 Economic data

The economic analysis relies on electricity market data provided by EnergyOnline (2024). The year 2024 was selected as the reference year, as it is both recent and representative of average market conditions, over the last decades: median price, as well as the extremes ones ($Q_{10\%}$ and $Q_{90\%}$, that are respectively the 10th and 90th quartiles) are aligned with past data (Figure 4.6).

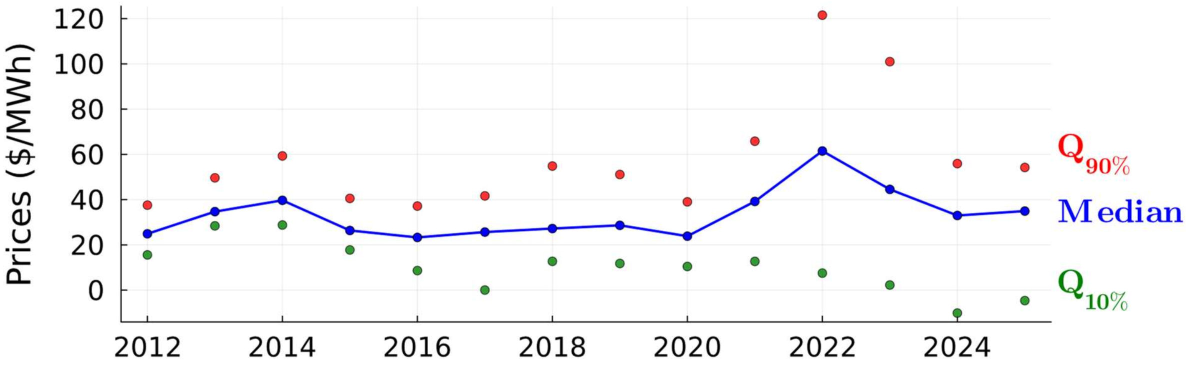

Figure 4.6 – Price distribution over the years in the CAISO market

CAISO is divided into three zones (North, Central and South). The majority of utility-scale solar power plants are located in the South zone, which has a strong influence on local electricity prices due to the high penetration of PV generation. This spatial concentration is reflected in the zonal price profiles, as illustrated in Figure 4.7. In the next sections, South zone data are used.

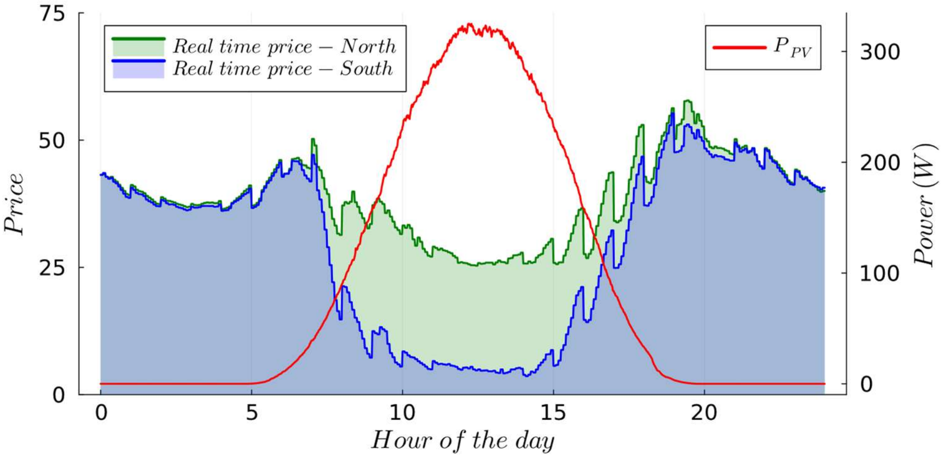

Figure 4.7 - Average electricity prices and PV production in 2024

Figure 4.8 illustrates the electricity price evolution over a four-day period in June 2024. A correlation between PV generation and electricity prices can be observed. During periods of high solar production, prices decrease significantly and may even become negative, while higher prices occur during periods of reduced PV output.

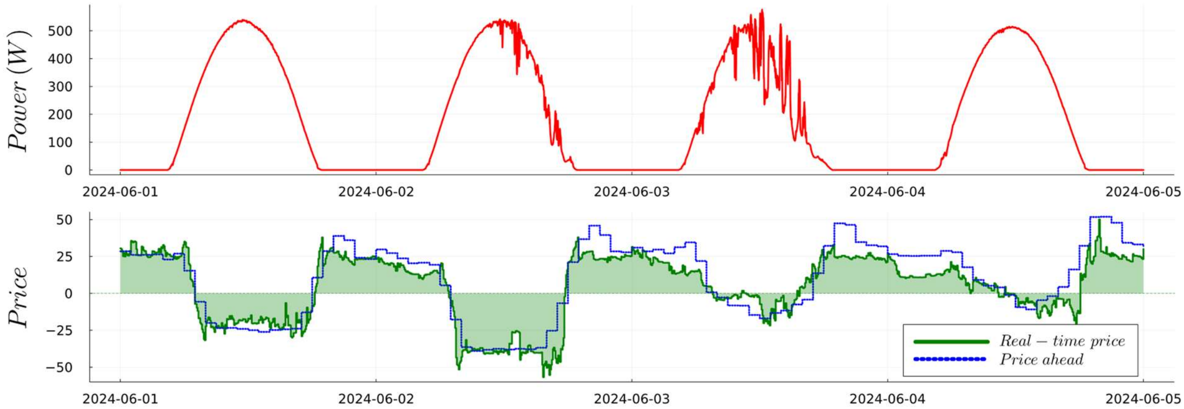

Figure 4.8 - Electricity price evolution, data from (EnergyOnline, 2024)

The baseline revenue considered in the next section is 1.09 M$/year if the solar farm operated only in RTM in the south zone. In the north one it would be 3.05 M$/year.

4.3 Battery integration strategies

4.3.1 Selected scenarios

As seen in the literature review, combining storage and PV systems has three main objectives (Meng et al., 2022):

- Stabilizing the production curve of solar energy
- Firming solar generation to increase resilience
- Engaging in energy arbitrage based off the price in real time and day ahead markets

To assess the impact of battery integration on the interaction between the photovoltaic system and the grid, these three strategies will be studied. They are schematiccaly represented in Figure 4.9.

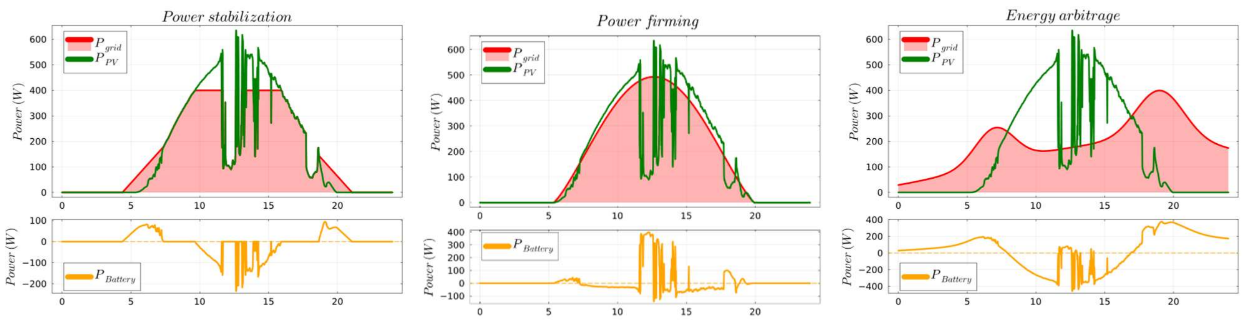

Figure 4.9 - Battery integration strategy scenario

4.3.2 Energy trading market rules (CAISO)

4.3.2.1 Day-ahead market & real-time market

Two main energy markets coexist: the day-ahead market (DAM) and the real-time market (RTM).

DAM is cleared one day before delivery, typically on an hourly basis. Market participants submit offers to sell or buy electricity for each hour of the next day. Once accepted, these bids become binding financial commitments: the buyer must buy, and the seller must sell. It allows participants to protect themselves against price uncertainty and schedule their operations efficiently.

RTM, also called the spot market, operates close to actual delivery, typically every five minutes, to balance supply and demand deviations from day-ahead schedules. Prices in the RTM reflect real-time system conditions, such as unexpected load variations or renewable generation fluctuations.

Overall, the total revenue for the day can be calculated as:

$$\Pi_{gain} = \Pi_{DA} * P_{DA} + \Pi_{RT} * (P_{RT} - P_{DA}) \qquad 4.1$$

where Π_{DA} and Π_{RT} are the day-ahead and real-time prices, and P_{DA} and P_{RT} are the scheduled and actually delivered energy quantity.

4.3.2.2 Additional revenue sources

Beyond energy arbitrage, BESS operators can generate revenue by participating in capacity markets. These mechanisms compensate operators for maintaining available power capacity that can be dispatched when needed to ensure system reliability.

In California, this mechanism is known as the Resource Adequacy Market (RAM). For each unit of committed capacity in the RA program, the average price on the 2023-2027 period was 11.11 $/(kW month) (CPUC, 2025). This payment compensates the resource for being available. The rule for this commitment is to be able to dispatch the committed power for four hours (CAISO, 2025). Additionally, RA resources must be committed every day at a bidding price fixed by the BESS operator (with a limit of 1000$/MWh). If the RTM electricity prices exceed it, the BESS is then dispatched and the operator is paid at bidding price for the energy delivered. (CAISO, 2025).

To represent cyclic degradation associated with RA participation, we assume that the committed RA capacity is dispatched every time the RTM price exceeds the day-ahead price by 35 $/MWh. This threshold was chosen from (CAISO, 2025) which reports that on 24th July 2024 a real-time price spike coincided with RA dispatch (Figure 4.10). As shown in Figure 4.11, RA capacity was dispatched precisely during the hours when real-time prices exceeded day-ahead prices by several hundred dollars per megawatt-hour. Additionally, 35 \$/MWh represented the median electricity price in 2024.

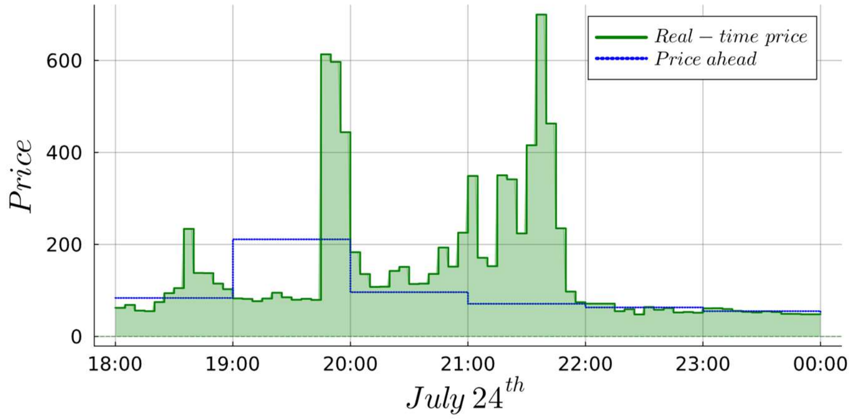

Figure 4.10 - DAM and RTM prices on the 24th July 2024

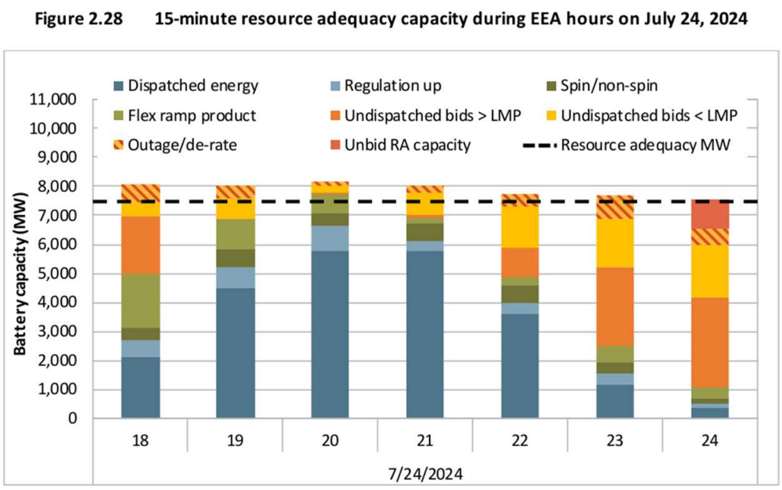

Figure 4.11 - RA dispatched energy on the 24th July 2024

Finally, BESS can also participate in ancillary service markets, providing fast-response support such as frequency regulation. However, those services often represent a small portion of BESS revenue (<4%) (Hotz & Berini, 2025) and will thus not be considered in our work.

In practice, BESS operators often pursue a revenue stacking strategy, combining energy arbitrage, capacity payments, and ancillary services. This multi-market participation maximizes asset utilization, mitigates exposure to price volatility, and supports overall grid reliability.

4.3.3 Perfect forecast vs uncertainty

In a first phase, all simulations will be performed under the assumption of a perfect knowledge of all data (PV production, RTM prices, battery behavior). The goal is to obtain the performance of best-case scenarios and establish reference points for comparisons with more realistic cases.

In a second phase, optimization will be performed while considering uncertainty for future conditions. Unlike the deterministic case, where all future variables such as solar generation, or electricity prices were assumed to be perfectly known, this second approach will integrate uncertainty by relying on forecasted or estimated values.

The parameter determination will be informed by educated guesses gained from the perfect forecast results. This will give a more realistic control strategy, where decisions are based on imperfect information while still looking for optimal performance. To guide the operational control of BESS, these educated guesses will be derived from day-ahead weather forecasts. In order to remain realistic, the meteorological information will be limited to classifying the day as clear, broken clouds, or overcast (with the definition presented in Chapter 2). This approach reflects the level of information typically available to operators.

One of the main decision variables is $\overline{P_{PV}}$ the average PV production of one PV panel for the day. It is directly linked to the type of weather and the time of the year. We can model the evolution of the average daily PV production as a sinusoidal function of the time such as:

$$\overline{PV_{day}} = \alpha \sin\left(\frac{2\pi}{365} * n + \beta\right) + \gamma \qquad 4.2$$

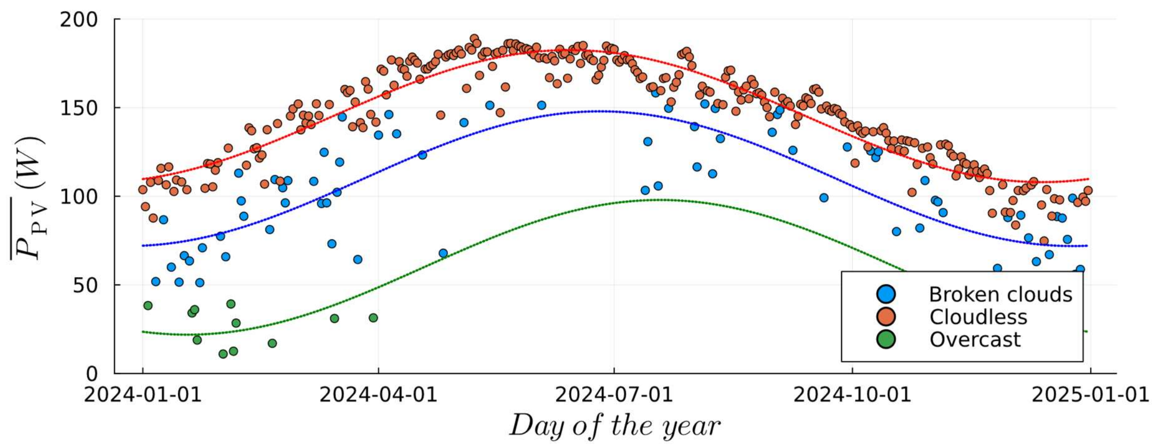

Figure 4.12 - Average daily PV production over the course of the year for one PV panel

Table 4.1 Average daily PV production model coefficient

	α	β	γ	R^2
Cloudless	37.250	-1.282	145.225	0.901
Broken clouds	38.001	-1.484	109.903	0.782
Overcast	38.021	-1.884	59.915	0.471

4.4 Solar farm architecture

4.4.1 Battery connection architecture

In utility-scale PV power plants, BESS can be integrated using two main coupling methods: AC and DC coupling, as illustrated on Figure 4.13. In AC coupling, the battery is connected to the AC side of the system through a dedicated inverter, allowing flexibility in system design but involving multiple energy conversion steps that reduce efficiency. In contrast, DC coupling connects the battery directly to the DC side of the PV system, eliminating the need for an additional inverter and therefore reducing the cost. This setup reduces conversion losses as DC/DC conversion is more efficient and because the energy charged to the battery and then injected into the grid goes through only four conversions and not six. However, DC coupling imposes stricter design and operational constraints and requires more complex battery management, since the shared inverter cannot operate bidirectionally simultaneously. As a result, grid charging is generally not available, and the presence of a single inverter limits the ability to simultaneously export maximum PV and battery power (Lo Franco et al., 2021).

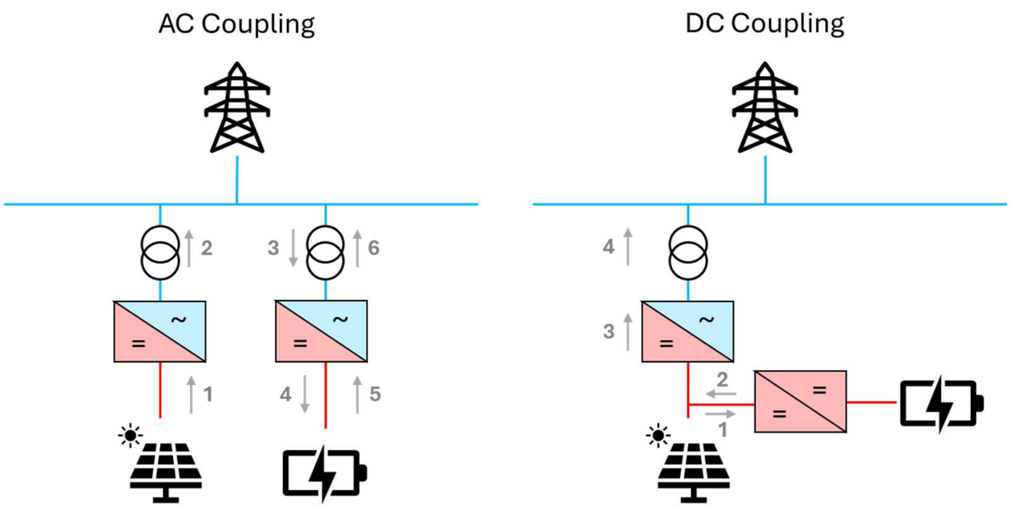

Figure 4.13 - AC vs. DC coupling architecture

The advantages and disadvantages of each architecture can be summarized from Durvasulu and Lo Franco's work (2021; 2021) in Table 4.2.

Table 4.2 – AC vs. DC architecture comparison

	AC coupling	DC coupling
Round trip efficiency	~ 91%	~ 95%
Advantages	- **Easier integration**: Can be retrofitted into existing AC systems. - **Flexibility**: PV and BESS operate independently with separate inverters. -**Modularity:** BESS can be located remotely from the PV array. - **Standardization**: Uses common inverters, making it compatible with various grid configurations.	- **Higher efficiency**: Fewer conversion stages reduce energy losses. - **Lower cost**: Eliminates the need for an extra inverter, reducing CAPEX & OPEX. - **Clipping recapture**: Excess DC power during PV inverter saturation can be stored in the battery instead of being clipped. - **Low voltage harvesting:** Captures energy at low voltages (morning/evening/cloudy) that are under the inverter threshold
Disadvantages	**- Higher cost**: Requires an additional inverter and transformer, increasing hardware and installation costs. - **Lower efficiency**: Multiple conversion stages lead to more energy losses.	**- Complex integration**: Requires compatible DC voltage levels and specific battery management. - **Less flexible**: PV and BESS share a single inverter, limiting simultaneous full-power operation and grid charging - **More challenging retrofitting**: Difficult to add storage to existing PV systems.

4.4.2 System configuration

The complete system general configuration is presented on Figure 4.14 with the different variable name for the AC coupling configuration.

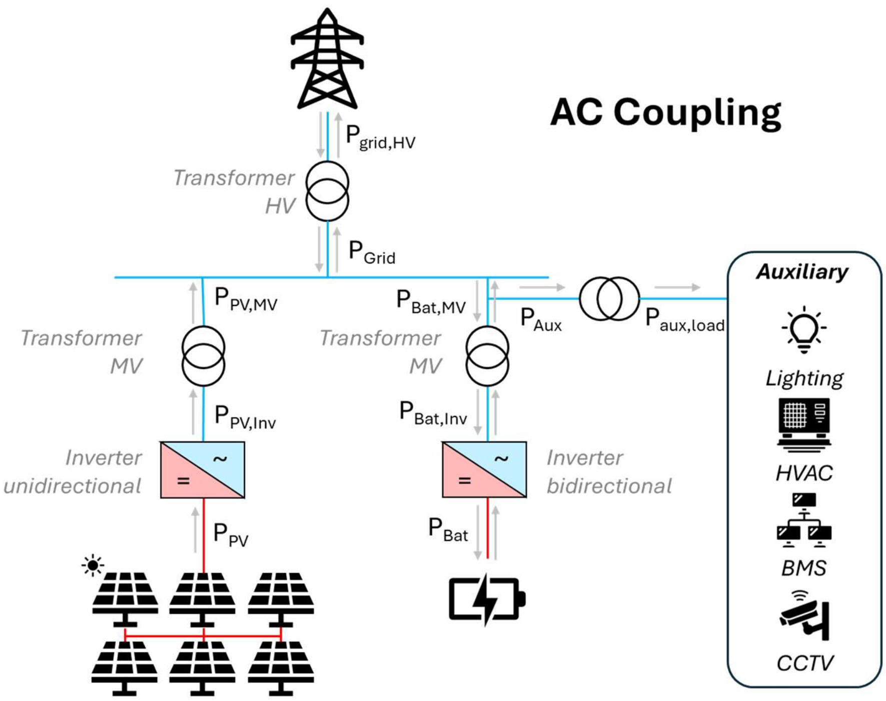

Figure 4.14 - Complete BESS + PV system

In reality, PV panels are organized into different sections, each connected to an inverter. The output of these inverters are then aggregated into medium-voltage (MV) transformers. Finally, all blocks are combined into a single high-voltage (HV) transformer that interfaces with the grid. The system sizing parameters are presented on Figure 4.15 below.

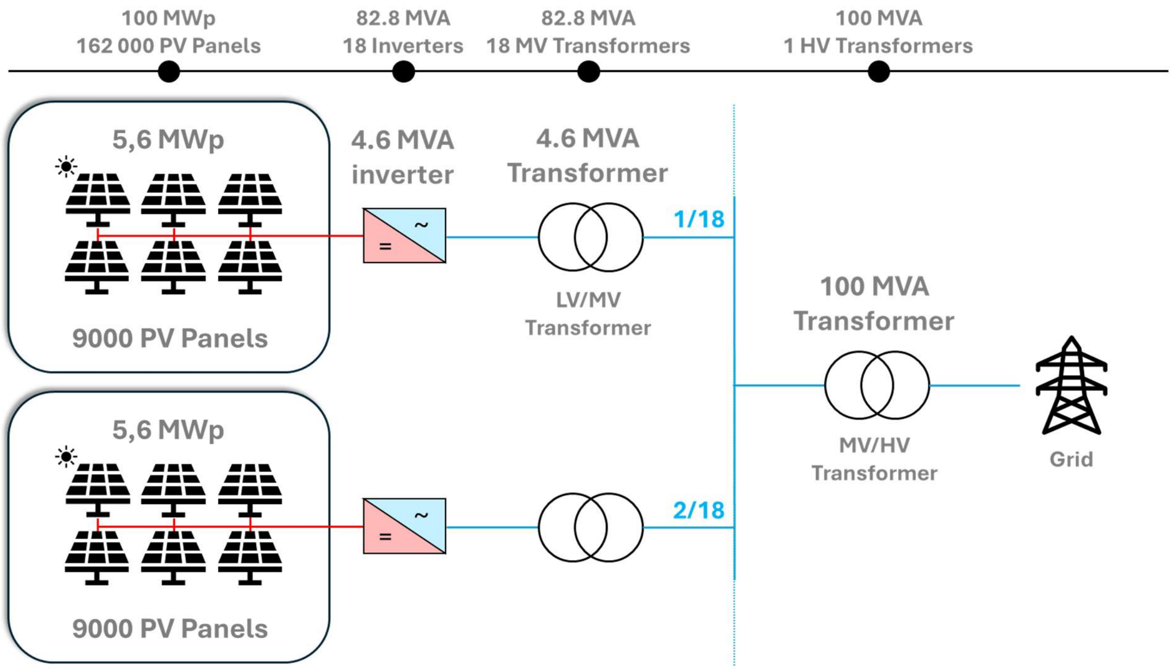

Figure 4.15 - System specification and dimensions

Each quantity is summarized in the table below:

Table 4.3 - Solar power plant sizing parameters

Elements	$P_{nominal}$	Quantity	Total Power
PV Panels	620 W	9000 * 18 = 162 000	100,4 MWp
Inverters	4.6 MVA	18	82.8 MVA
MV transformers	4.6 MVA	18	82.8 MVA
HV transformers	100 MWa	1	100 MVa
Batteries	-	-	25 MW/4h or 50 MW/2h

4.4.3 Component models

4.4.3.1 Battery model

The BESS is modeled as a collection of identical battery containers, each with a rated capacity of 2 MWh (EnergyX, 2025). A total of 50 containers is installed on site, resulting in a rated capacity of 100 MWh. Each container is composed of several racks, with each rack assembled from multiple modules. In the model, each module consists of groups of 100 cells (each cell having a capacity of 1.5Ah to match the design of the K2 LFP18650E cell from Chapter 3).

The SOC is constrained to a 5-95 % range to reflect operating limits and preserve battery lifetime. Battery self-discharge is accounted for in the model and assumed to be 2 % per month (R-Smith et al., 2023).

In the model, a P_{grid} setpoint is given as an input, and P_{bat} is then deduced:

$$P_{grid} = P_{PV,MV} + P_{Bat,MV} - P_{aux} \quad 4.3$$

So

$$P_{grid} = P_{PV,MV} + f_{transfo}(f_{inv}(P_{Bat})) - P_{aux} \quad 4.4$$

Finally:

$$P_{bat} = f_{transfo}^{-1}(f_{inv}^{-1}\,(P_{grid} + P_{aux} - P_{PV,MV})) \quad 4.5$$

Where P_{xx} are the different powers as defined on Figure 4.14. f_{inv} is the inverter efficiency function, that will be defined in section 4.4.3.3. $f_{transfo}$ is the transformer efficiency function, that will be defined in section 4.4.3.4

4.4.3.2 Cable loss model

Ohmic losses induced by cables can be calculated using the model presented in PVsyst:

$$P_{Ohmic,DC}(I) = R_w * I^2 \quad 4.6$$

Where R_w is defined as the equivalent resistance of the wires. PVsyst offers a general solution to calculate this resistance when there is no final design of a solar farm:

$$R_w = 0.015 * V_{mp}/I_{mp} \quad 4.7$$

With the selected solar panels, R_w=0.0475 Ω. Over a year, the cable losses represent 1.15 % of the solar production.

4.4.3.3 Inverter model

Two different types of inverters need to be used. The PV-side ones are unidirectional inverters whereas the ones on the battery side are bidirectional. Their behavior and efficiency are modeled for both types according to the PVsyst inverter model (PVsyst SA, n.d.) that is represented on Figure 4.16 below. The conversion efficiency of the inverters is a function of both the load input and DC voltage operation point.

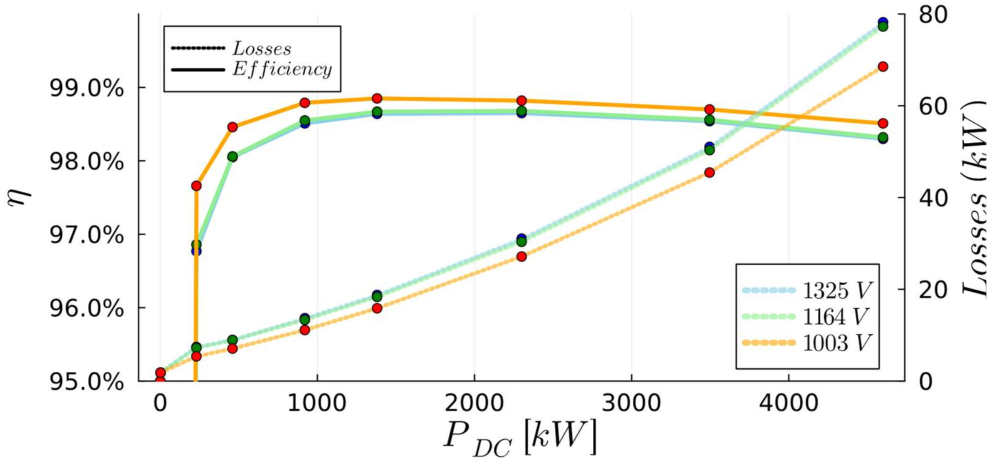

Figure 4.16 - inverter efficiency model

The inverters selected for this study are SMA Sunny Central 4600 units (SMA, 2024). Their allowable DC input voltage range is 1003 V to 1325 V. To remain within this range, PV panels are arranged in strings of 30 PV panels in series leading to a block architecture of 300 parallel strings per inverter. The resulting voltage output is presented in Figure 4.17.

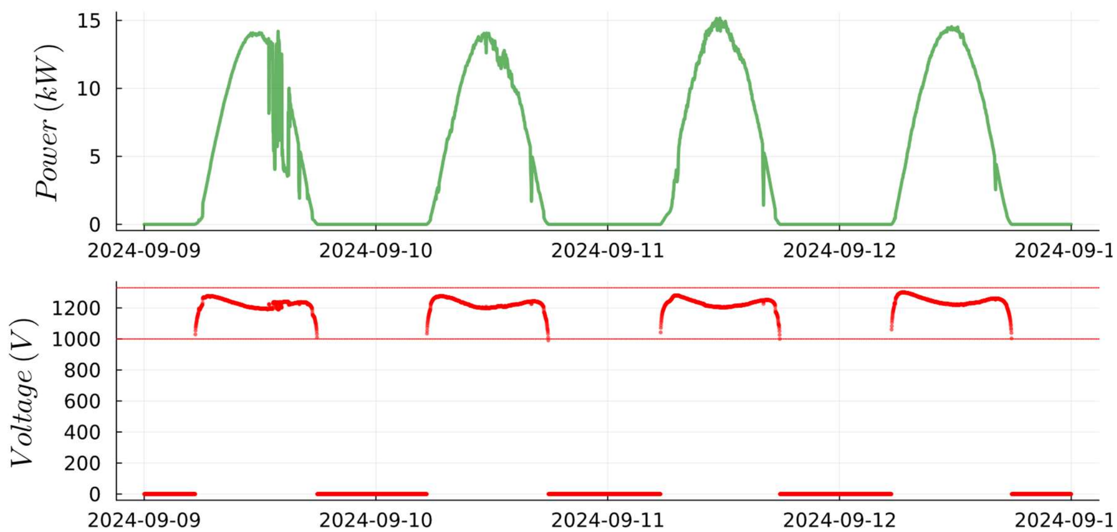

Figure 4.17 - power and voltage output for each string of 30 PV panels

Over a year, the inverter conversion adds 2.12 % of losses to the total PV production. The reduction is due to the imperfect efficiency and the curtailment that happens when the PV production is too high, as presented in Figure 4.18.

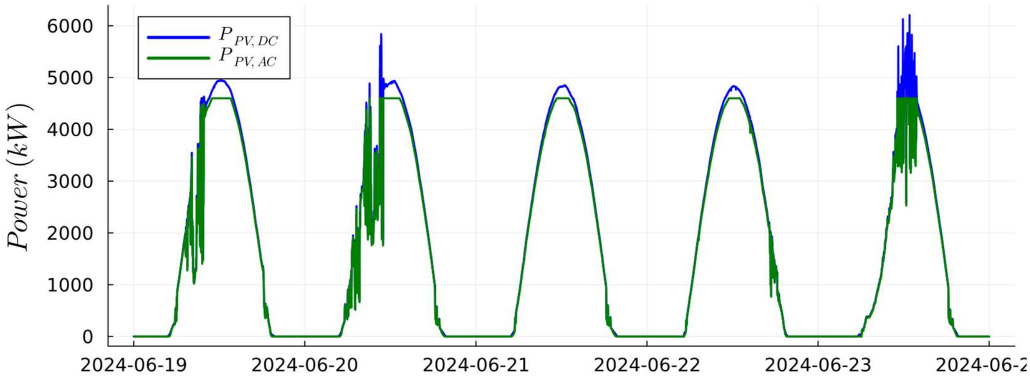

Figure 4.18 - Inverter induced losses illustration

4.4.3.4 Transformer model

There are three types of losses in a transformer:

- No-load losses (iron losses from Foucault induced current)
- Operating losses linked to the current (also called the copper losses)
- Cooling system consumption

According to the IEC 60076-20 standard (IEC, 2017), the efficiency index EI_A is defined as:

$$EI_A = \frac{S - L}{S} \quad 4.8$$

Where S is the input power and L the total losses. Here, the inverter has a power factor equal to 1, so $S = P_{AC}$ directly. The efficiency index can be calculated as:

$$EI_A = \frac{kS_r - (P_0 + P_{c0}) - (k^2 P_k + P_{ck}(k))}{kS_r} \quad 4.9$$

Where:

- S_r is the rated power in VA (ie Volt Amperes) of the transformer
- k is the load factor
- P_0 is the no load loss

- P_{c0} is the cooling power required
- P_k is the measured load loss in W at rated current and rated frequency
- $P_{ck}(k)$ is the additional electrical power in W required (in addition to P_{c0}) by the cooling system for operation at load factor k

So:

$$P_{losses} = (P_0 + P_{c0}) + \left(\left(\frac{P_{AC}}{S_r}\right)^2 P_k + P_{ck}(k)\right) \tag{4.10}$$

We assume that the cooling power P_0 and $P_{ck}(k)$ are negligible (Janic et al., 2023) so:

$$P_{Losses} = P_0 + P_k * \left(\frac{P_{AC}}{S_r}\right)^2 \tag{4.11}$$

P_0 and P_k values are either given in the datasheet or can be deduced from the PEI and k_{PEI} value with the following formulas:

$$\begin{cases} PEI = 1 - \dfrac{2}{S_r} * \sqrt{P_0/P_k} \\ k_{PEI} = \sqrt{\dfrac{P_0}{P_k}} \end{cases} \tag{4.12}$$

Where PEI and k_{PEI} are respectively the best efficiency reached by the transformer and the load at which it is reached. P_0 and P_k can then be calculated as:

$$\begin{cases} P_k = \dfrac{1 - PEI}{2} * \dfrac{S_r}{k_{PEi}} \\ P_0 = k_{PEI}^2 * P_k \end{cases} \tag{4.13}$$

If we consider an MV transformer with a rated load of 4600 kVa, a PEI = 99.542% and k_{PEI} = 32.75%, we get P_k = 32.1 kW and P_0 = 3.5 kW.

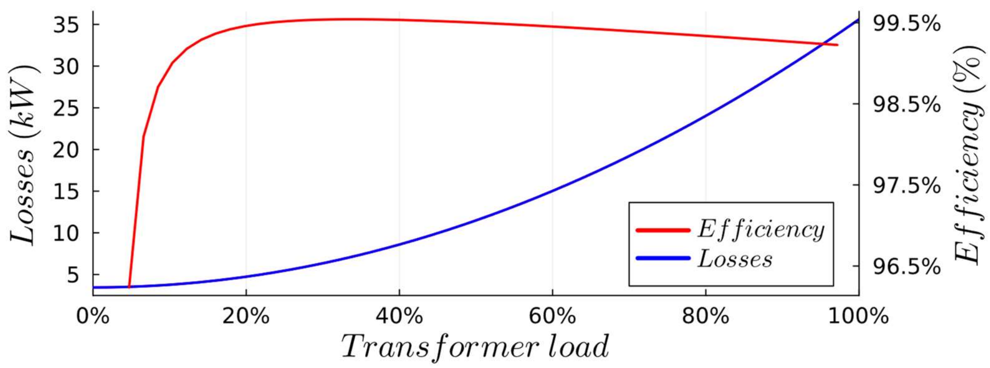

Figure 4.19 - Transformer efficiency and losses evolution with the load

Overall, the annual conversion losses of the MV transformer represent 0.8 % of the energy output of the inverter. The effect of the transformer can be seen in Figure 4.20.

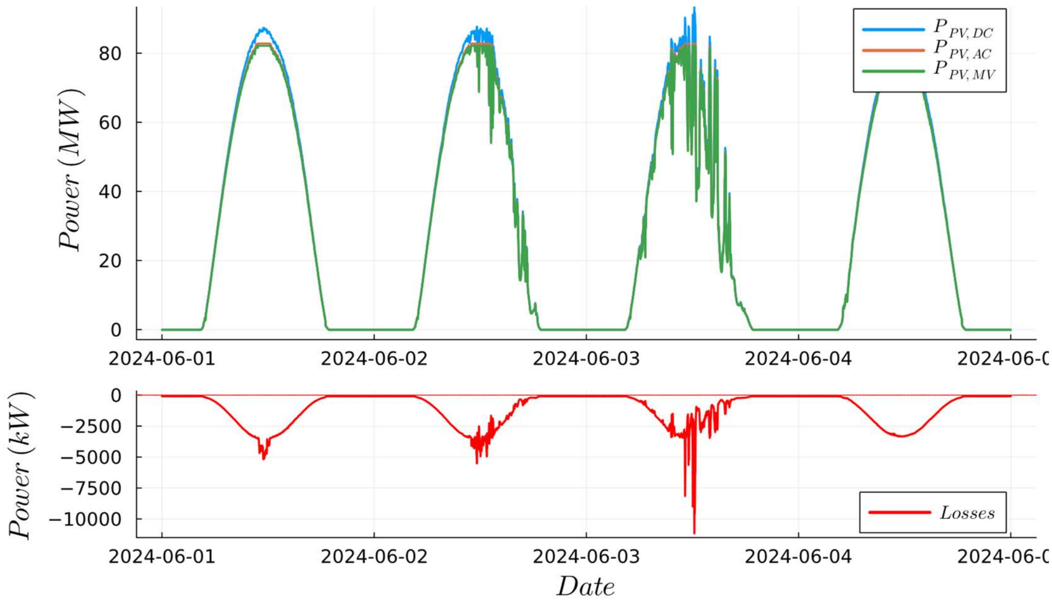

Figure 4.20 - Transformer induced losses illusration

In summary, the total losses are equal to 4.01% of the initial PV production.

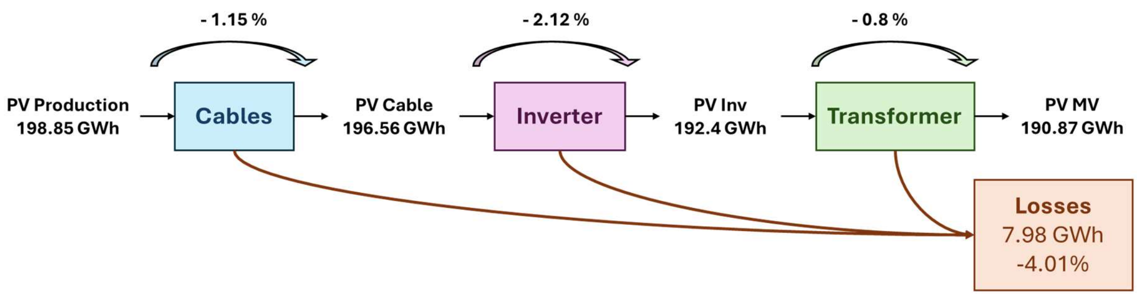

Figure 4.21 - Total PV system losses at Grid connection point

4.4.3.5 HVAC

The HVAC model from Rosewater et al. (2019) is used. This model is applied to a lumped volume, here it will be applied to the aggregated module of 100 cells (with $R_0 = R_{ini}/100$). The first equation represents the heat balance of the batteries, i.e. the difference between the heat generated by the batteries (ohmic losses) and the heat exchanged with the container air volume. The second equation represents the heat balance of the container volume, i.e. the difference between the heat gains from the batteries and the heat exchanged with the environment, accounting for the heat added or removed by the HVAC system. Solar gains on the container are neglected.

$$C_{bat}\frac{dT_{bat}}{dt} = R_0 * I_{bat}^2 + UA_{bat}(T_{cont} - T_{bat})$$

$$C_{cont}\frac{dT_{cont}}{dt} = N_{cell}\big(UA_{bat}(T_{bat} - T_{cont})\big) + UA_{cont}(T_{amb} - T_{cont}) - \eta_{HVAC}P_{HVAC} \tag{4.14}$$

P_{HVAC} is < 0 in cooling mode and > 0 in heating mode. The following constants are used:

Table 4.4 – HVAC model components coefficients

UA_{bat}	UA_{cont}	C_{cont}	η_{HVAC}
0.5 W/K (Rosewater et al., 2019)	30 W/K (Olis et al., 2023)	30 kJ /K (Olis et al., 2023)	6 (Rosewater et al., 2019)

In the model, T_{bat} is considered as a constant, so $C_{bat}\frac{dT_{bat}}{dt} = 0$.

On a year the total HVAC consumption depends on the scenarios investigated below but a representative value is 585 kWh, with strong variations throughout the day, as shown in Figure 4.22, which illustrates conditions requiring heating during the night and cooling during the day.

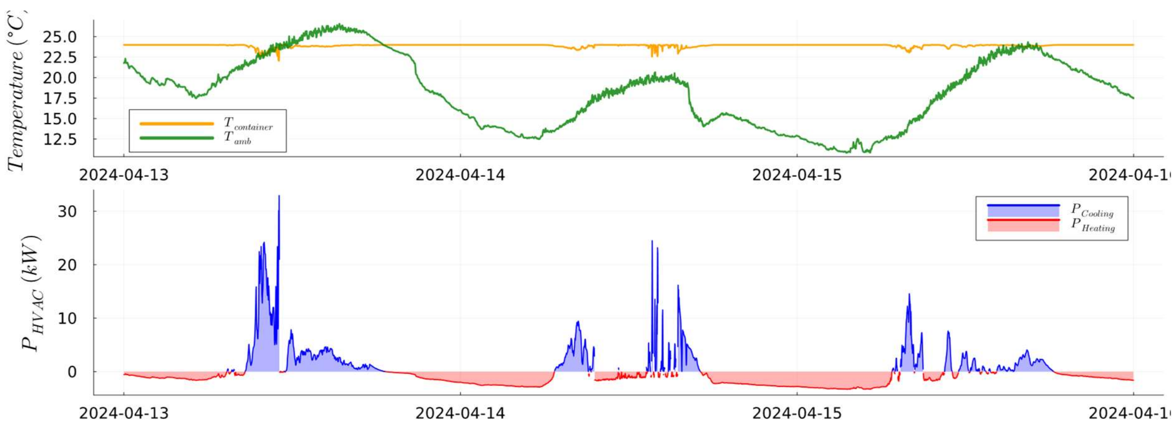

Figure 4.22 – Total P_{HVAC} for the fifty BESS containers

Additional auxiliary loads, such as the battery management system (BMS), lighting, and CCTV, are modeled as a fixed consumption equal to 0.2% of the installed PV capacity (Pandey, 2017), corresponding to an auxiliary power demand of 20 kW.

4.5 PV power ramp-up stabilization

4.5.1 Mathematical optimization framework

In this configuration, the battery operates as a ramp-rate controller to mitigate the steep variations in power output that typically occur at sunrise and sunset. The objective is to ensure smoother transitions in the morning and evening by absorbing or supplying power so that the net PV power injected into the grid evolves gradually. This approach reduces stress on grid infrastructure and is a response to the duck curve phenomena that can be observed in areas supplied by high levels of renewable energy.

There are three control variables in this scenario that need to be adjusted every day:

- $t_{morning}$ and $t_{evening}$: they are the difference between the start of the ramp-up and stop of ramp-down periods with the real sunrise and sunset times.
- $P_{Cut-off}$: maximum PV power allowed to be exported to the grid.

The mathematical definition of the instruction P_{obj} using those three parameters to create the shape presented in Figure 4.23 is details in Appendix C.

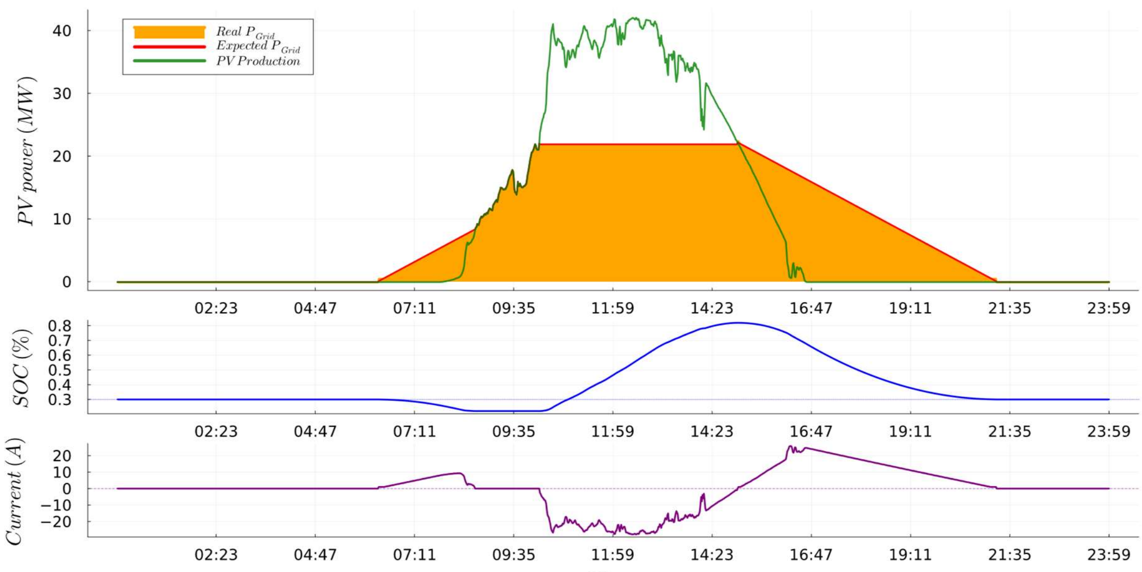

Figure 4.23 - Illustration of Scenario 1 on a perfect day

In the optimization process, three types of penalty are defined:

- The balance penalty : $Penalty_1 = |SOC_{end} - 0.2| * \gamma_1$, the goal here is to have a SOC at the beginning and the end of the end around 20 % to ensure the proper functioning on the following day. The battery can't end the day being too much charged or it won't be able to absorb the next day peak.
- The accuracy penalty: $Penalty_2 = \sum\left(P_{grid} - P_{obj}\right)^2 * \gamma_2$, the goal here is to have a result as close as possible to the given instruction. P_{grid} is the actual power sent to the grid, while P_{obj} is the instruction given to the batter.
- The time penalty: $Penalty_3 = \left(\frac{1}{t_{morning}} + \frac{4}{t_{evening}}\right) * \gamma_3$, the goal here is to ensure that the ramp up and ramp down will start/stop enough time in amount of the sunrise/down time. A bigger weight is attributed to the $t_{evening}$ parameters reflecting the real behavior of BESS operator (Figure 4.2) that discharge most of their energy at night.

Finally, the optimization process will be to find each day set of parameters that minimize the sum of those three penalties:

$$Min_{(t_{morning}, t_{evening}, Cut-off)}(Penalty_1 + Penalty_2 + Penalty_3) \quad 4.15$$

4.5.2 Perfect forecast and deduction of heuristic operation strategy

In the first phase, the optimization presented in last section is performed under the assumption of a perfect knowledge of all data. The results over multiple days are presented on Figure 4.24.

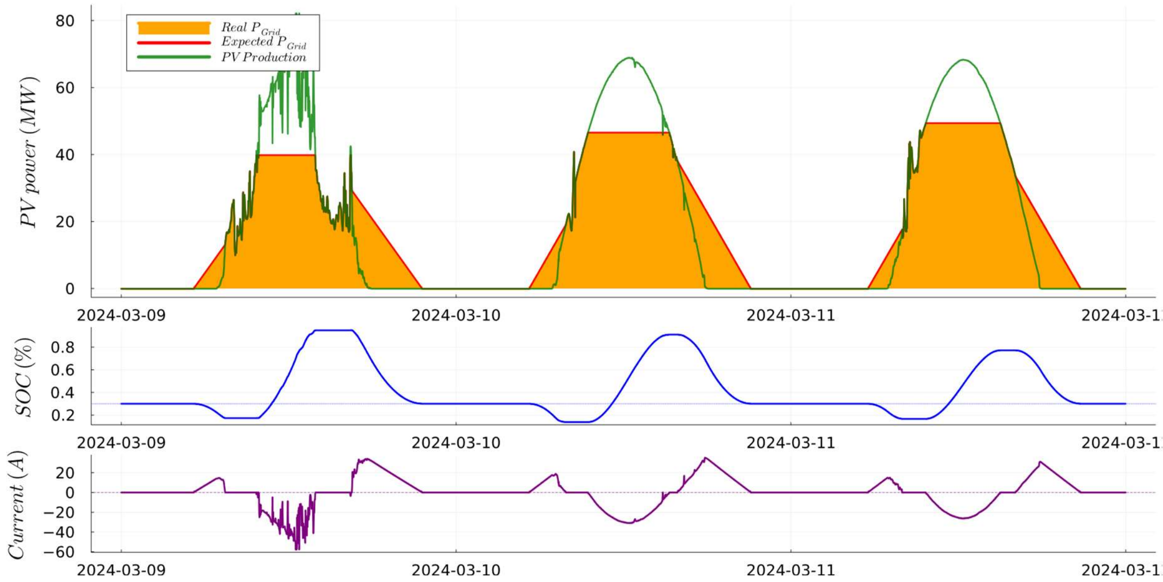

Figure 4.24- Illustration of Scenario 1 over several days

As we can see, the instructions are consistently respected, and the battery behavior is regular. From those results, we can see that the relationship between the P_{cut-o} parameter and $\overline{P_{PV}}$ is a linear relationship across all weather conditions, as illustrated in Figure 4.25. This proportionality reflects the fact that, on brighter days, the cut-off level must increase to avoid excessive PV curtailment.

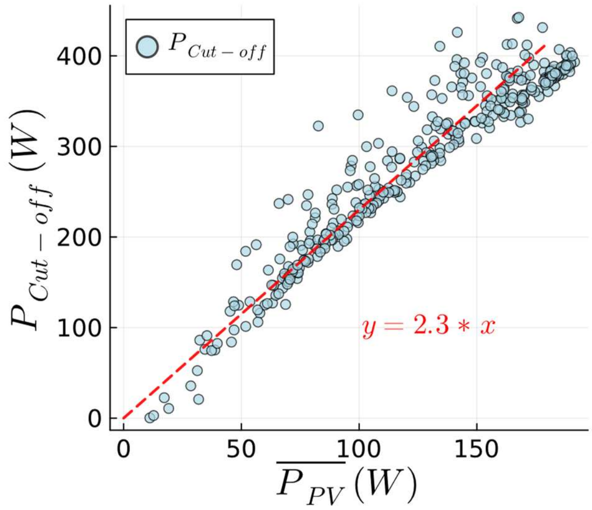

Figure 4.25 - $P_{cut-off}$ as a linear function of $\overline{P_{PV}}$

Additionally, we can also see that the temporal parameters $t_{morning}$ and $t_{evening}$ follow sinusoidal trends that need to be fitted for each weather. The numerical results are detailed in Appendix C.

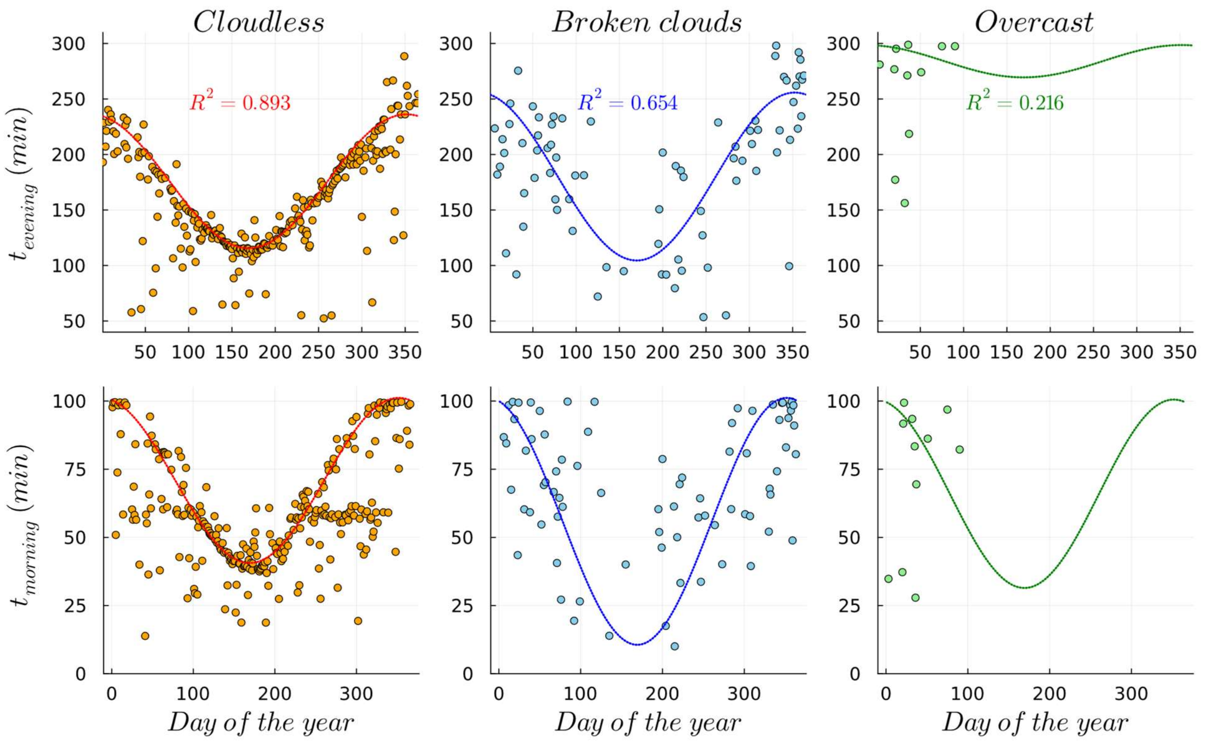

Figure 4.26 - coefficient evolution model in scenario 1

4.5.3 Uncertain situation

In this section, P_{obj} is fixed - and not optimized anymore - each day, based only on the weather class of the day, the time of the year and the operational control derived in the previous section.

To ensure that these instructed setpoints can be followed, SOC guardrails are applied. Indeed, initial SOC can significantly reduce feasibility: a battery that begins the day nearly empty or full cannot correctly follow its given instructions. As the ideal SOC at the beginning of each day should be around 20 %, the instructions are adapted if the SOC is too far from this value.

If $SOC < 0.15$, it means that the ramp-up control in the morning must be reduced. Additionally, the reserve made from peak-shaving can be increased.

$$\begin{cases} P_{cut-off,adapted} = 0.9 * P_{cut-off,calculated} \\ time_{motning} = time_{motning} * 0.5 \end{cases} \quad 4.16$$

If $SOC > 0.3$, it means the battery has too much reserve and will not be able to absorb as much energy during the day as initially expected. Therefore, $P_{cut-off}$ must be increased to limit charging.

$$P_{cut-off,adapted} = 1.1 * P_{cut-off,calculated} \quad 4.17$$

These adaptations are derived from a heuristic process of trials and errors to find the best adaptation that would ensure the proper execution of the given instruction.

To compare the different results, several metrics are introduced. The round-trip efficiency of the battery is defined as:

$$\frac{\sum|P_{charged}(t)| - \sum P_{discharged}(t)}{\sum|P_{charged}(t)|} \qquad 4.18$$

The success rate of the scenario is defined as:

$$Success\ rate\ (\%) = 100 * \left(1 - \frac{N_{error}}{N_{steps}}\right) \qquad 4.19$$

With N_{steps} the number of time steps where $P_{PV} > 0$ and N_{error} is the number of time steps where the battery follows the instruction within the given tolerance ϵ = 0.1 MW.

$$N_{error} = \sum_{t=1}^{N_{steps}} \mathbf{1}\left(\left|P_{grid}(t) - P_{obj}(t)\right| > \epsilon\right) \qquad 4.20$$

The two P_{grid} value are calculated as:

$$Initial\ P_{grid} = P_{PV,MV} - P_{aux} \qquad 4.21$$

$$Scenario\ P_{grid} = P_{PV,MV} + P_{bat,MV} - P_{aux} \qquad 4.22$$

Where $P_{PV,MV}$ value is given in section 4.4.3.4.

Finally, all the percentages values are calculated in reference to the initial scenario.

The comparison between scenario optimized with perfect forecast and the uncertain one are presented below for the two tariff zones, North and South.

Table 4.5 – Comparison between scenario 1 scenario optimized with perfect forecast and the uncertain one

	North		South	
	Perfect forecast	Uncertain	Perfect forecast	Uncertain
Initial P_{Grid}	126.8 GWh	126.8 GWh	189.31 GWh	189.31 GWh
Scenario P_{Grid}	124.97 GWh	125.16 GWh	187.24 GWh	187.36 GWh
P_{lost}	1.8 GWh	1.6 GWh	2.07 GWh	1.95 GWh
	1.43 %	1.28 %	1.11 %	1.04 %
Profit ($)	3.44 M$	3.39 M$	1.95 M$	1.83 M$
	+ 13.11 %	+ 11.2 %	+ 78.84 %	+67.84 %

N_{ecc}	457.8	412.7	543.42	484.78
$P_{charged}$	24.9 GWh	22.4 GWh	29.5 GWh	26.4 GWh
$P_{discharged}$	23.1 GWh	20.7 GWh	27.3 GWh	23.4 GWh
Round-trip efficiency	92.5 %	92.5 %	92.5 %	92.1 %
Instruction followed	97 %	85.4 %	98.12 %	83.32 %

In conclusion, this scenario demonstrates that ramp-up smoothing is predictable: the optimal parameters depend on the day of the year and the predicted mean PV production. The linear and sinusoidal models derived here provide a practical rule-based controller that responds almost 85 % of the time to the given instructions.

Additionally, the energy shifting occurring thanks to the energy ramp-down control offers financial improvements as it allows the BESS to capture the high energy price in the beginning of the evening while simultaneously reducing the amount of energy sold at midday.

4.6 PV power production firming

4.6.1 Mathematical optimization framework

The main objective of this strategy is to reduce the fluctuations in PV production throughout the day. The goal is to obtain a more regular and predictable power profile by compensating for intra-hour variations due to passing clouds or irradiance instability. This strategy, often referred to as power firming or power smoothing, improves power quality and facilitates grid integration by reducing volatility on shorter time scales.

The strategy consists in correcting the real PV production curve toward a smooth reference shape. This reference is obtained by applying a scalar form factor f to a perfect irradiance profile G_{ext} to get the instruction P_{obj} to the battery as illustrated on Figure 4.27.

$$P_{obj} = f * G_{ext} \tag{4.23}$$

Two types of penalty are defined to control the optimization process:

- The balance penalty : $Penalty_1 = |SOC_{end} - 0.5| * \gamma_1$, the goal here is to have a SOC at the beginning and the end of the end around 50% to ensure the good functioning of the following day. This value was chosen so the battery has equal capacity available for both charging (absorbing excess PV production) and discharging (supplementing dips in PV output)

- The accuracy penalty: $Penalty_2 = \sum(P_{grid} - P_{obj})^2 * \gamma_2$, the goal here is to have a result as close as possible to the instruction to smoothen the production every day

Finally, the optimization process will be to find each day the parameter f that minimizes the sum of those two penalties:

$$Min_f(Penalty_1 + Penalty_2) \tag{4.24}$$

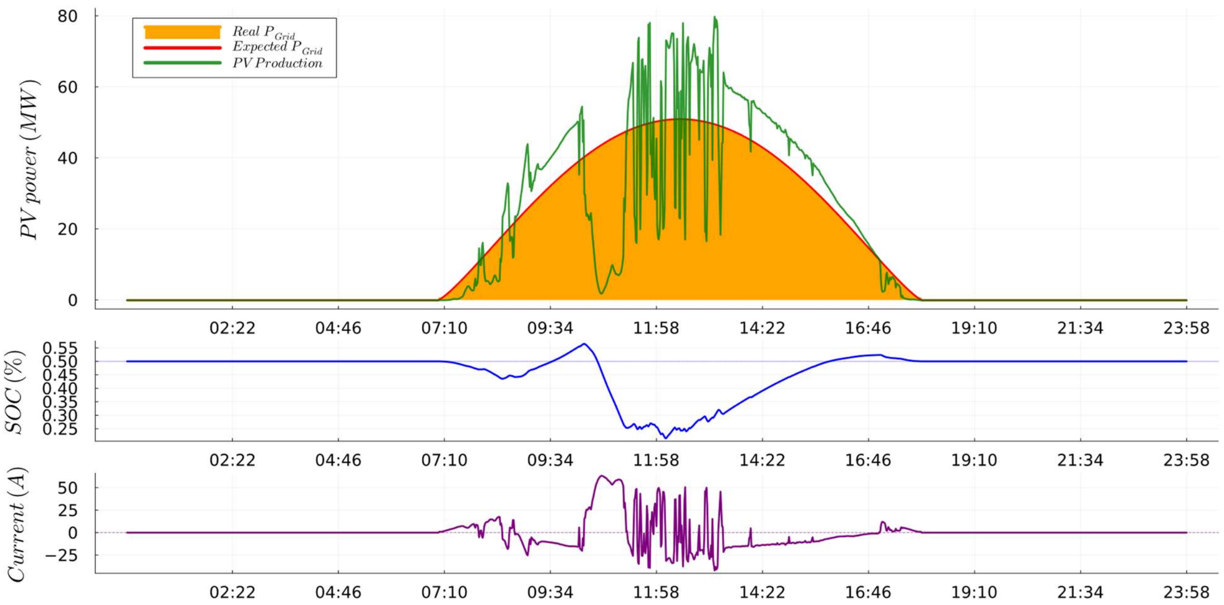

Figure 4.27 -Scenario 2 illustration on a perfect day

4.6.2 Perfect forecast and deduction of heuristic operation strategy

Following the same process than in section 4.5, the optimization presented in last section is first performed under the assumption of a perfect knowledge of all data. From the results obtained, we can remove the deterministic part of f by normalizing it by $\max(G_{ext})$ and linking it to $\overline{P_{PV}}$ for each weather type as illustrated on Figure 4.28. The numerical results are detailed in Appendix C.

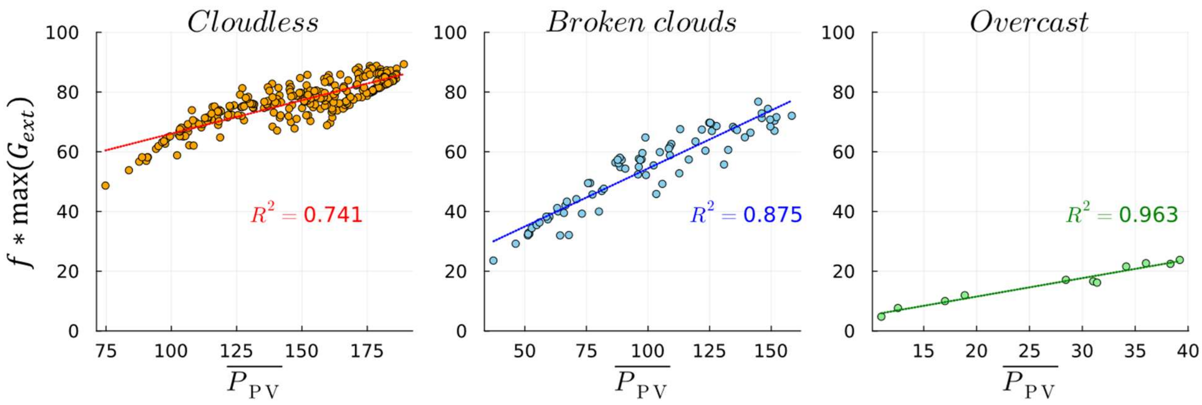

Figure 4.28 – f parameter generalization

4.6.3 Uncertain situation

As for the first scenario, the instruction factor f is adapted to the initial SOC. If the SOC is too low, f must be reduced so the battery will charge more than it discharges through the day. In the opposite situation, f must be increased so the battery discharges more than it get charged.

$$f = \begin{cases} 0.85 * f, & SOC_{ini} \leq 0.3 \\ 1.15 * f, & SOC_{ini} \geq 0.7 \end{cases} \tag{4.25}$$

The table below summarizes the performance of the different scenarios, using the same metrics presented in section 4.5.

Table 4.6 – Comparison between scenario 2 scenario optimized with perfect forecast and the uncertain one

	North		South	
	Perfect forecast	Uncertain	Perfect forecast	Uncertain
Initial P_{Grid}	126.8 GWh	126.5 GWh	189.31 GWh	189.31 GWh
Scenario P_{Grid}	125.64 GWh	125.76 GWh	188.19 GWh	188.14 GWh
P_{lost}	1.12 GWh	1.0 GWh	1.12 GWh	1.17 GWh
	0.89 %	0.8 %	0.6 %	0.62 %
Profit ($)	3.1 M$	3.1 M$	1.105 M$	1.12 M$
	+ 1.13 %	+ 1.2 %	+ 1.26 %	+ 3.04 %
N_{ecc}	264.7	264.14	198.57	251.32
$P_{charged}$	14.5 GWh	14.7 GWh	13 GWh	14.1 GWh
$P_{discharged}$	13.4 GWh	13.7 GWh	11.8 GWh	12.9 GWh
Round-trip efficiency	92.1 %	93.1 %	90.3 %	91.7 %
Instruction followed	90 %	74.89 %	92.08 %	82.62 %

In conclusion, the power firming scenario highlights the ability of a BESS to transform variable PV generation into a smooth, predictable power profile. The success rate of this scenario is lower than the previous one, whether it is in the perfectly optimized or uncertain one, but it remains high around 75%.

As expected, this scenario provides minimal financial gain, since no energy shifting occurs, and the battery utilization remains relatively low. Nevertheless, it is a scenario adapted for applications requiring predictable and stable PV output, such as self-consumption schemes or micro-grid integration.

4.7 Energy arbitrage

In this scenario, the battery is operated to shift energy in time to maximize the electricity revenue from the solar farm. The goal is to store electricity during periods of high PV generation (and low value) and discharge it during periods of high demand or higher market prices. This strategy aims to maximize the economic value of the system and can also contribute to peak-load reduction.

4.7.1 Two-shot strategy

In the literature, a commonly applied energy trading strategy under perfect foresight assumes that the operator has complete knowledge of future electricity prices. Under this idealized condition, the battery is scheduled to fully charge during the two cheapest hours and fully discharge during the two most expensive hours of each day. This approach, here referred to as the two-shot strategy, aims to maximize daily revenue by exploiting the largest possible intraday price spread. (Serafin & Weron, 2025)

The selection of the cheapest and most expensive hours can be based on either real-time prices or day-ahead prices to be more realistic. The scenario illustrated on Figure 4.29 presents the optimal configuration for a day, using day-ahead prices. The energy is purchased during the cheapest hours around midday and then sold back at the end of the day. The profit made that day comes from the price spread between those hours.

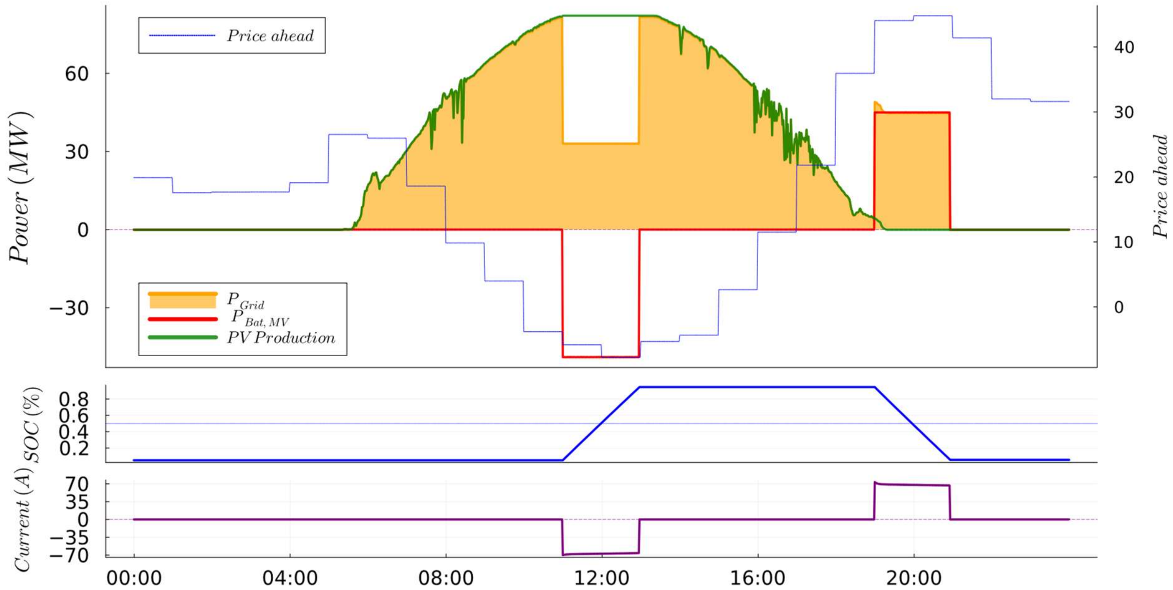

Figure 4.29 -Two-shots strategy illustration

The results of both scenarios are presented in Table 4.7.

Table 4.7 – Scenario comparison between RTM and DAM arbitrage

	North		South	
	DAM	RTM	DAM	RTM
Initial P_{Grid}	126.8 GWh	126.8 GWh	189.31 GWh	189.31 GWh
Scenario P_{Grid}	123.38 GWh	123.38 GWh	186.05 GWh	186.05 GWh
P_{lost}	3.4 GWh	3.4 GWh	3.26 GWh	3.26 GWh
	2.73%	2.73%	1.75 %	1.75 %
Initial Profit	3.05 M$	3.05 M$	1.09 M$	1.09 M$
Profit ($)	4.3 M$	4.43 M$	3.01 M$	3.17M$
	+ 41.1 %	+ 45.4 %	+ 176 %	+191 %
N_{ecc}	651.5	651.5	651.5	651.5
$P_{charged}$	35 GWh	35 GWh	35 GWh	35 GWh
$P_{discharged}$	31.8 GWh	31.8 GWh	31.8 GWh	31.8 GWh
Round-trip efficiency	90.8 %	90.8 %	90.8 %	90.8 %

In conclusion, the energy arbitrage scenario demonstrates that a BESS can substantially increase revenue by strategically charging and discharging in response to market prices. In the simulated cases, profits were boosted significantly (up to nearly triple the initial value in the most favorable scenarios) highlighting the strong economic potential of arbitrage operations.

However, this financial gain comes at the cost of intensive battery cycling, with high numbers of cycles being performed in a year. This scenario implies increased battery degradation, which must be considered when evaluating long-term profitability and lifetime impact.

Additionally, while the revenue improvements are better in the RTM, it is dangerous to only trade in this market as it is volatile and has lower certainty compared with DAM. One option is to use daily DAM announcements to guide bets on favorable RTM slots. However, the main limitation of this strategy is that day-ahead market forecasts are becoming less accurate over time (Prakash et al., 2025). This is mainly due to greater price volatility caused by increasing renewable energy integration and by market reforms that now allow intraday trading and rebidding.

Based on the selected datasets, only about 45 % of the hours predicted as optimal by the day-ahead market are actually accurate. Only using that data would thus lead to missed opportunity.

4.7.2 Additional profitability mechanisms

In real market conditions, electricity prices are uncertain and highly variable, which limits the effectiveness of strategies based solely on perfect foresight. To improve profitability, several complementary mechanisms can be considered.

1) Capacity market participation.

Capacity market participation could represent a major complementary revenue source. In the Californian Resource Adequacy (RA) program, committing 7.5 MW of available capacity can secure approximately 1 M$/year in guaranteed income, providing a stable financial baseline to complement energy-market revenues. In 2025, RA revenue for BESS operators represented between 35 % and 70 % of their revenue in California (Hotz & Berini, 2025).

However, committing capacity in the RA has consequences for BESS health. Indeed, it imposes maintaining a higher minimum state of charge. This raises the battery's average resting SOC throughout the year, which then accelerates calendar ageing. In parallel, it also reduces the number of cycles that the battery has to go through.

Determining whether the RA commitment ultimately shortens or extends battery lifetime is thus not obvious and will be studied in a later section.

2) Day-ahead versus real-time spread opportunities.

When the real-time price is lower than the day-ahead price, a BESS operator who sold energy day-ahead but did not discharge in real time can still generate profit. The financial gain equals:

$$\text{Gain} = (\Pi_{DA} - \Pi_{RT}) * P_{DA} \qquad 4.26$$

This mechanism allows revenue even without physical energy delivery. It is called virtual bidding and exists to ensure that the energy supplied in the grid always matches the demand.

3) Dynamic rebidding.

In RTM, rebidding is allowed every five minutes, enabling operators to adjust their offers to short-term price variations. By strategically rebidding during periods of extreme high or low prices, the BESS can further increase profitability.

In the remainder of this work, only capacity market participation will be considered.

4.8 Long term performance

To quantify the impact of each scenario on battery degradation, multi-year simulations using repeated data from section 4.2 were performed using the coupled cyclic aging and calendar aging models established in Chapter 4. For each scenario the evolution of SOH was computed until the threshold of 80 % was reached.

Additionally, the instruction given in each scenario were adapted to the progressive degradation of the capacity, as presented in Annex C.

4.8.1 Scenario 1: Grid stabilization

Over multi-year operation, this control strategy produces an SOH trajectory in which cyclic aging dominates, while the contribution from calendar aging remains smaller, as presented on Figure 4.30. The battery reached its end-of-life threshold after **10.6 years**. Calendar aging remains moderate because the system spent **62.4 %** of its time in idle mode with a mean calendar SOC of only **29.3 %**. A total of **4064 cycles** were completed, and the battery observed a round-trip efficiency of **92.5 %**.

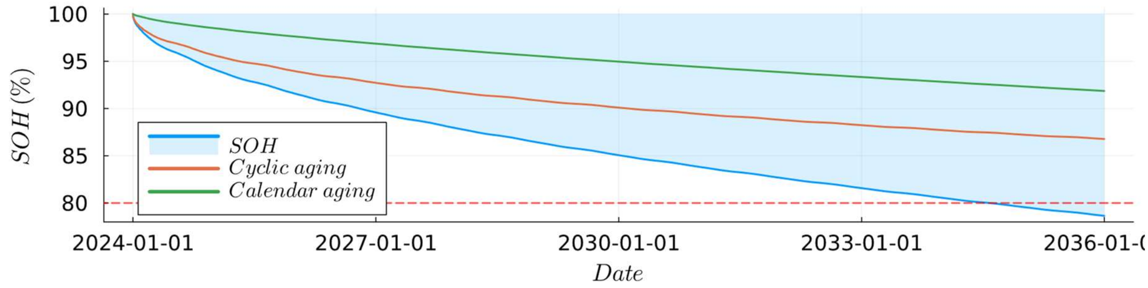

Figure 4.30 - SOH evolution in scenario 1

From a financial point of view, the trapezoidal expected shape was announced in the DAM to maximize profit. The total revenue increases by **145 %**, corresponding to a revenue of **26.07 $M**. Finally, the ramp-rate objective was fulfilled **85 %** of the time, which is consistent with the expected precision presented in section 4.5.3.

We can see on Figure 4.31 that even though the capacity of the battery had already lost 15% of its original value at the represented time, the instructions given are still respected: energy is shifted from midday to the evening period.

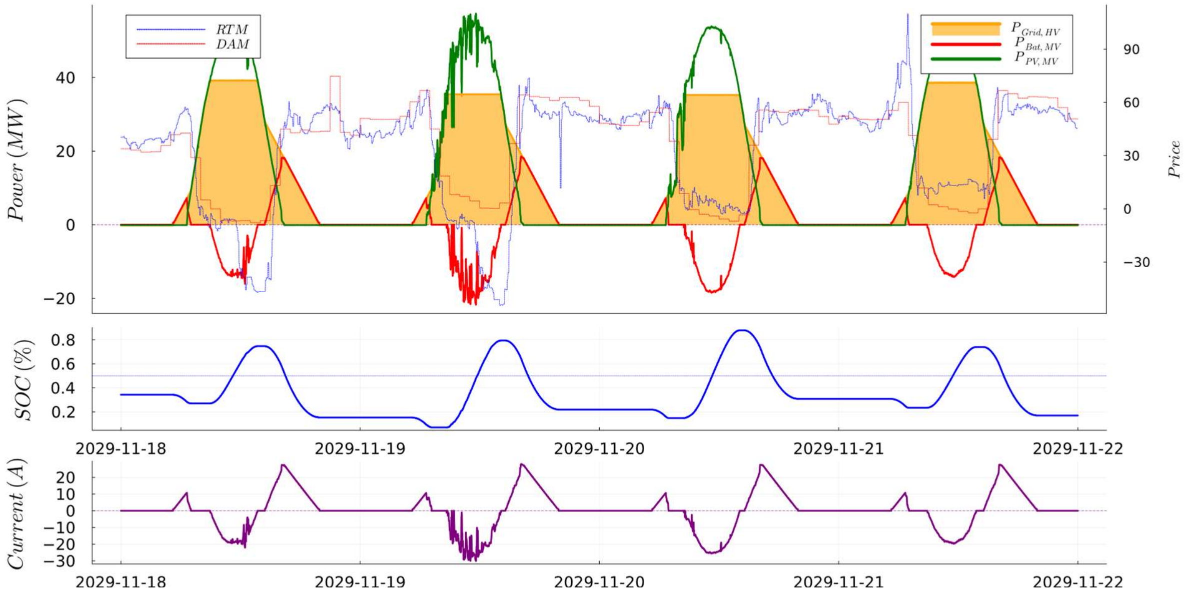

Figure 4.31 - Scenario 1 long-term performance illustration

4.8.2 Scenario 2: Power firming

Compared to the previous scenario, this control strategy produces an SOH evolution which reflects a more balanced distribution between cyclic and calendar degradation, as presented on Figure 4.32.

The battery reached its end-of-life threshold after **10.8 years**. A characteristic of this scenario is the higher SOC maintained throughout the day. The system spends **59.9 %** of its time in calendar mode with a mean calendar SOC of **45.8 %**, a level that increases the contribution of calendar aging. A total of **3067 cycles** were completed, and the battery observed a round-trip efficiency of **92.5 %**.

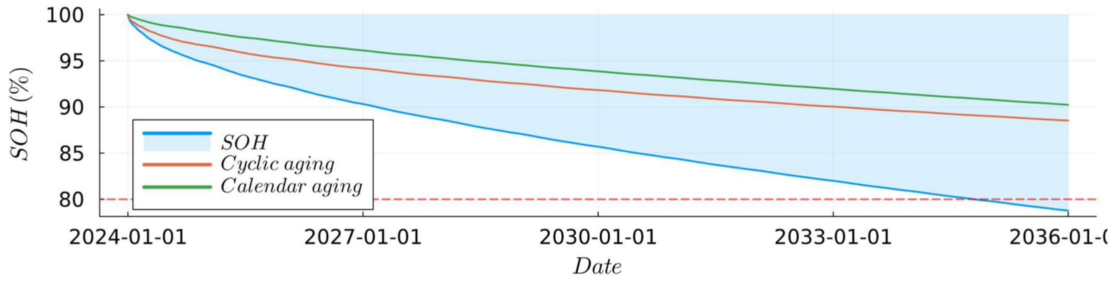

Figure 4.32 - Scenario 2 SOH evolution

To reduce the profit losses due to negative prices around midday, an expected PV production calculated as $f * G_{ext}$ was announced in the DAM. The total revenue increases by **64.0 %**, corresponding to a revenue of **19.02 $M**. Finally, the ramp-rate objective was fulfilled **76.1 %** of the time, which is consistent with the expected precision presented in section 4.6.3.

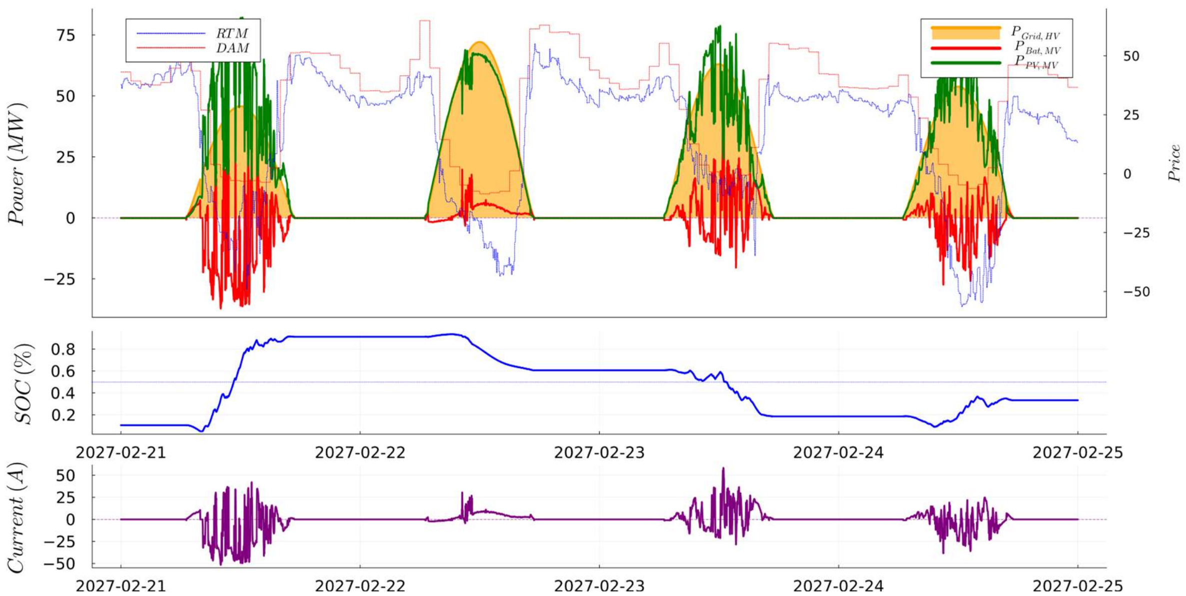

Figure 4.33 - Scenario 2 long-term performance illustration

4.8.3 Scenario 3: Energy arbitrage

4.8.3.1 DAM vs RTM

In this strategy, buying and selling decisions are split between DAM and RTM. In RTM, electricity prices are lower on average (Figure 4.34), making it advantageous for the BESS operator to buy energy in this market. On the contrary, the DAM is used to declare selling orders as the prices are higher on average, as well as guaranteed.

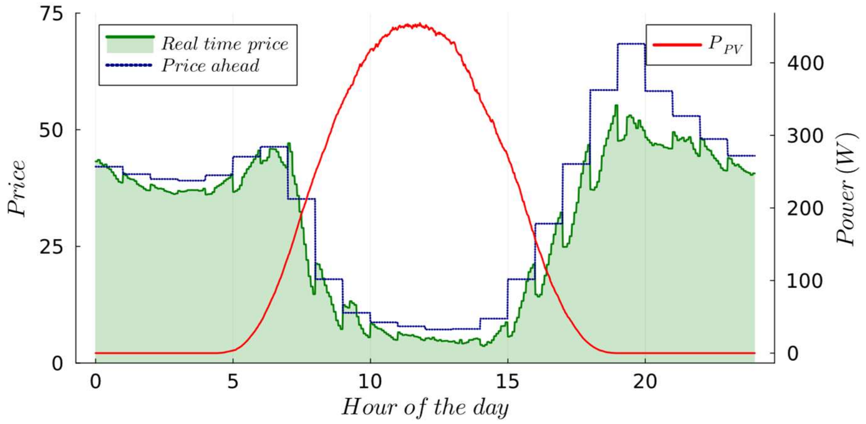

Figure 4.34 - Average annual electricity prices and PV production (South)

Additionally, an expected PV production, calculated as presented in Eq. 4.27, is declared in the DAM to avoid negative prices as much as possible.

$$P_{PV,expected} = \overline{P_{PV}} / \overline{\mathrm{G}_{\mathrm{ext}}} * G_{ext} \qquad 4.27$$

Finally, RA responses for the committed capacity are triggered as soon as $\Pi_{RTM} \geq 35 + \Pi_{DAM}$ as defined in section 4.3.2.2, With Π_{RTM} & Π_{DAM} in \$/MWh. This control strategy is illustrated in Figure 4.35, where an RA commitment was dispatched on the 24th July for example.

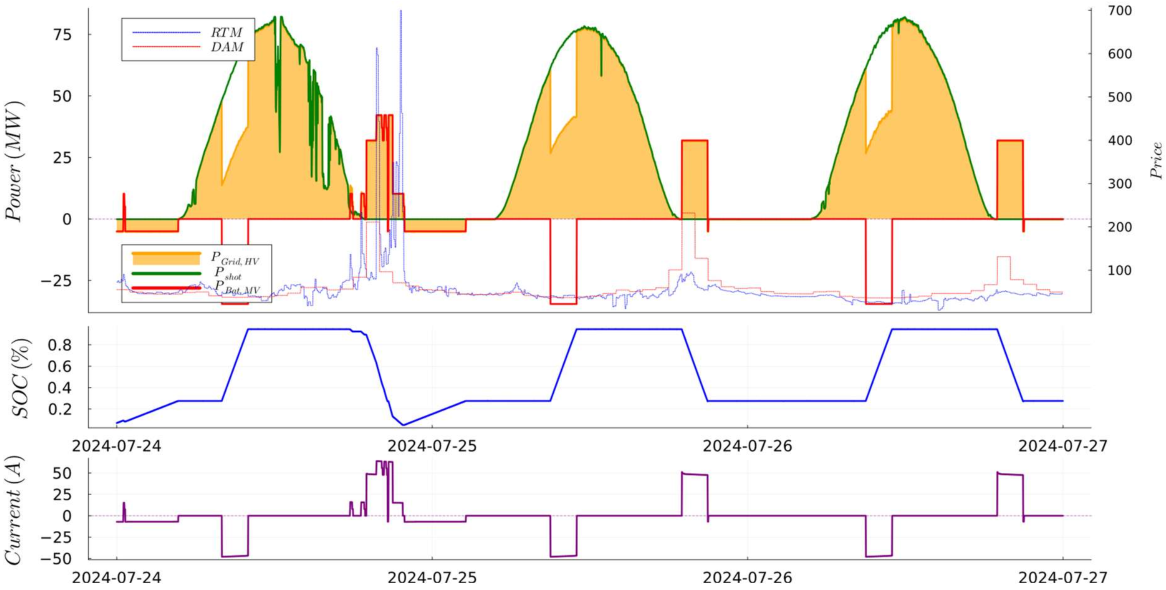

Figure 4.35 – Scenario 3 BESS behavior

4.8.3.2 Capacity market impact

While the two-shot strategy was presented with a full utilization of the battery capacity in section 4.7.1, a potential strategy to reduce the intensity of cyclic aging is instead to operate only a fraction of the available BESS capacity.

To study how RA participation impacts both the battery lifetime and its economic performance, a parametric study was conducted for four levels of RA commitment (0, 5, 10, and 15 MW) and four levels of remaining BESS capacity utilization (100 %, 75 %, 50 %, and 25 %). The results are presented in Table 4.8 and Table 4.9.

The results show that higher RA commitments increase the battery lifetime because part of the battery capacity becomes reserved and cannot be cycled freely, which lowers the number of equivalent full cycles. Additionally, reducing the available capacity used extends lifetime, because it also reduces the number of cycles completed.

However, this approach has limits. The configuration with the highest RA commitment and lowest utilization (15 MW, 25 %) is not the most durable, because the battery operates with a very high resting calendar SOC. This increases calendar aging, which eventually offsets the gains achieved by reducing cyclic usage.

Table 4.8 – years of usage before reaching SOH = 80%

Committed capacity \ Available capacity used	100 %	75 %	50 %	25 %
0 MW	6.56	8.20	9.42	11.80
5 MW	6.87	8.32	10.41	13.94
10 MW	7.18	8.29	9.79	12.10
15 MW	7.56	8.22	9.03	10.11

Table 4.9 - Total revenue before reaching SOH = 80% (M$)

Committed capacity \ Available capacity used	100%	75%	50%	25%
0 MW	23.21	26.66	25.25	27.89
5 MW	26.71	29.14	32.79	40.91
10 MW	29.77	32.03	36.33	42.71
15 MW	32.02	34.99	37.73	41.44

The influence of different aging mechanisms is illustrated in Figure 4.36 and

Figure 4.37 with two different utilizations of the battery. In the first scenario (high RA commitment), degradation is mainly due to calendar aging, as the average resting SOC is at 80 %. On another hand, in the second one (no RA commitment) the dominant aging mechanism is cyclic aging.

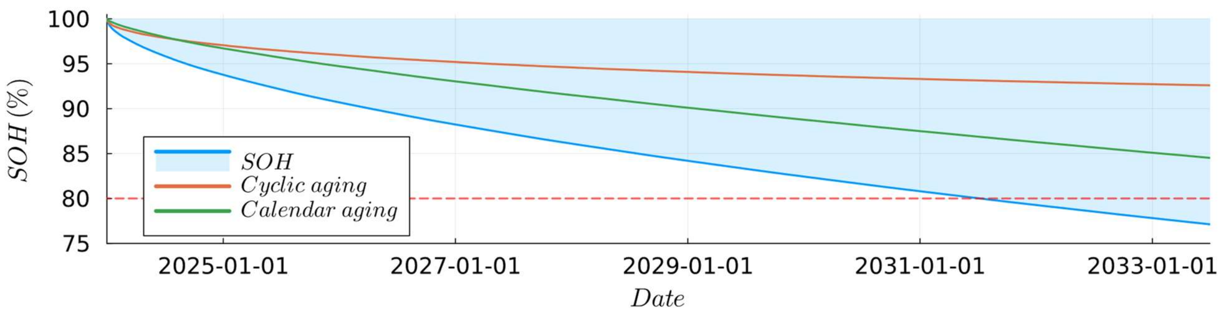

Figure 4.36 - SOH evolution, 15 MW, 100 %

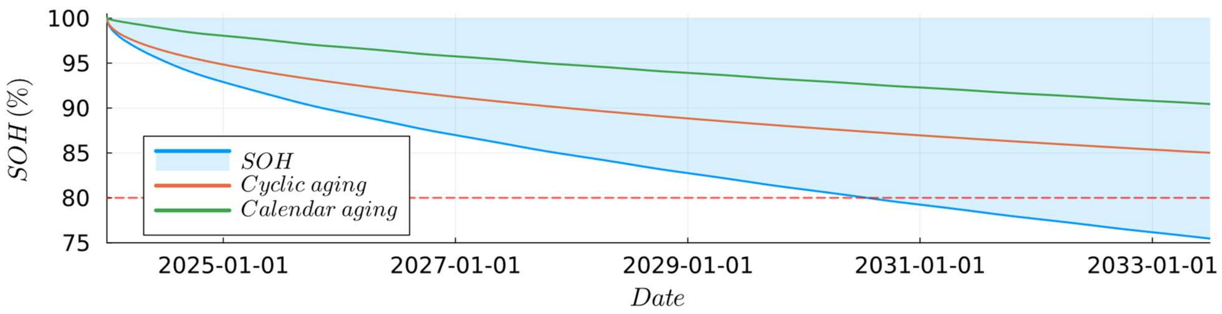

Figure 4.37 - SOH evolution, 0 MW, 100 %

The numerical values for those two scenarios are summarized in Table 4.10.

Table 4.10 - Aging factor for different scenarios of energy arbitrage

	15 MW, 100 %	**0 MW, 100 %**
Cycle	1274	4168
Calendar time	83.45 %	83.45 %
$\overline{SOC_{calendar}}$	80.19 %	28.3 %
EOL	7.56 years	6.56 years

4.9 Economic analysis

4.9.1 Indicators

The definitions of the selected financial indicators were obtained from the System Advisor Model, SAM (NREL, 2025).

1. Net present value (NPV)

NPV is a financial metric that measures the value of a project or investment by considering all future cash flows, both revenues and costs, back to their value today. To be considered financially viable, a project needs to have a positive NPV. It is calculated as:

$$NPV = -C_{initial} + \sum_{t=0}^{T} \frac{A * (1+i)^t}{(1+r)^t} \qquad 4.28$$

Where T is the lifetime of the BESS, A the annual cashflow (revenue – expense), i the inflation and r the nominal discount rate.

2. Discounted payback period (DPBP)

Discounted payback period is the number of years required for the discounted cumulative cash flows to recover the initial investment.

$$DPBP = \min_{T} \left\{ \sum_{t=0}^{T} \frac{A * (1+i)^t}{(1+r)^t} \geq C_{initial} \right\} \qquad 4.29$$

4.9.2 Cost breakdown

The CAPEX and O&M costs were sourced from the NREL (2024b) study on utility scale BESS. CAPEX includes all the costs for battery modules, containers, BMS, thermal systems, inverters, transformers, DC cabling, civil works, installation labor, materials and engineering. O&M costs cover the recurring annual costs of operating the plant, including administrative labor, insurance, land leases, taxes, site security, routine and scheduled maintenance, and general operating labor.

The CAPEX of a BESS depends on both its energy capacity and its maximum rated power. While the cost of the battery modules is primarily linked with the total installed capacity, the associated components, such as inverters, transformers, and other power electronics, must be sized according to the peak power output. In consequence, the overall capital cost reflects a combination of energy and power requirements.

Table 4.11 summarizes the minimum energy duration required for different BESS power ratings under varying levels of committed capacity. For high committed capacity a 25MW-4h BESS can be set-up as the maximum power output injected into the grid will never be higher than 25MW. In contrast, under the most intensive usage scenario, a 50 MW-2 h system is required to support the higher power injection levels.

Table 4.11 - BESS sizing

Committed capacity \ Available capacity used	100%	75%	50%	25%
0 MW	2h	2h	4h	4h
5 MW	2h	4h	4h	4h
10 MW	4h	4h	4h	4h
15 MW	4h	4h	4h	4h

For a 2-hour storage system, the reported values are:

- CAPEX = 835 $/kW => 41.75 M$ for 100 MWh
- O&M = 17.65 $/kW/year => 882 k$/year for 100 MWh

For a 4-hour storage system, the reported values are:

- CAPEX = 1290 $/kW => 32.5 M$ for 100 MWh
- O&M = 28.043 $/kW/year => 700 k$/year for 100 MWh

Economic assumptions follow the guidance of Pullutasig & Belding (2024), with an inflation rate of 2.5 % and a nominal discount rate of 5.6 %.

To reduce the CAPEX investment of BESS, developers often seek to obtain subsidies. In the USA, the Inflation Reduction Act (IRA) provides a 30 % investment tax credit for standalone battery storage, which must be claimed in the first year of operation. However, many developers cannot benefit from the full credit as their taxes are lower than the amount they could claim. To address this, the IRA allows credit transferability, where developers can sell the credit to third parties who can use the credits to offset their own taxes. These transferred credits typically sell for 90–95 cents per dollar (LegalClarity, 2025).

4.9.1 Financial results

4.9.1.1 Grid stabilization & power firming

The first two scenarios do not achieve profitability when the BESS reaches its end of useful life. This was expected, as the revenue improvement achieved by the BESS is significantly lower than in the energy arbitrage scenario. The NPV in the grid stabilization scenario is -8.0 M$, while in the power firming scenario, it is -14.6 M$.

4.9.1.2 Energy arbitrage

The NPV and DPBP were calculated for all combinations of RA commitment and usable BESS capacity as defined in section 4.8.3.2. Table 4.12 and

Table 4.13 summarize the different results.

The results show that as the committed RA capacity increases, the NPV of the project improves due to the stable and important revenue provided by capacity payments. Additionally, moderate utilization of the BESS also improves the rentability of the project as it extends the battery life.

Table 4.12 NPV when reaching SOH = 80%

Committed capacity \ Available capacity used	100%	75%	50%	25%
0 MW	-6.77	-5.26	-7.52	-7.53
5 MW	-3.84	-2.72	-1.53	1.47
10 MW	-0.55	0.28	1.96	5.63
15 MW	1.04	3.45	5.26	7.17

Table 4.13 - DPBP SOH = 80%

Committed capacity \ Available capacity used	100%	75%	50%	25%
0 MW				
5 MW				12
10 MW		8	8	9
15 MW	7	7	7	7

The annual NPV evolution for the best-performing case (15 MW commitment, 25% utilization) is illustrated in Figure 4.38. The impact of the IRA investment tax credit appears clearly in the first year, significantly reducing the CAPEX, which then allows the project to be profitable within 7 years.

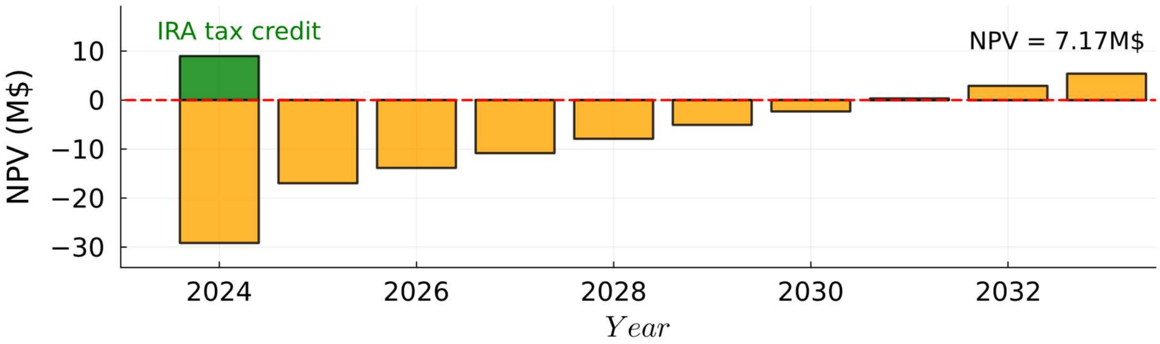

Figure 4.38 - NPV evolution in the energy arbitrage scenario

4.10 Conclusion

The objectives of this chapter were to model the interaction between a utility-scale PV power plant with BESS and the electrical grid, and to assess its economic performance. To that end, electrical components, conversion losses, auxiliary loads, HVAC consumption, and detailed market mechanisms were modeled, enabling realistic simulation of grid-connected PV-BESS operation under both technical and economic constraints (Figure 4.39).

Three distinct battery integration strategies were studied, corresponding to the main objectives identified in the literature: grid stabilization, PV production firming, and energy arbitrage. For each strategy, control laws were first optimized under perfect foresight to establish theoretical best-case scenario and then reformulated into practical rule-based controllers capable of operating under forecast uncertainty to assess the economic performance in realistic conditions.

The results show that grid stabilization and power firming strategies primarily enhance grid compatibility, reducing ramp rates and short-term variability. Those scenarios offer limited economic benefits, but they ensure a high longevity for battery. On the other hand, energy arbitrage is the dominant revenue driver, especially when combined with participation in the capacity market. The scenarios also have different impacts on aging mechanisms, and the different scenario impacts on the BESS are presented in Table 4.14. For the energy arbitrage scenario, as multiple parametric simulations were conducted, we included the best case scenario, which is the one where 15MW where committed in the capacity market and the remaining battery capacity was only used at 25 %.

Table 4.14 - Scenario impact results analysis

	Grid stabilization	**Power firming**	**Energy arbitrage (15 MW, 25 %)**
Longevity	10.6 years	10.8 years	10.1 years
Calendar aging	Low	Medium	High
Cyclic aging	High	Medium	Low
Economic upside	26.07 M$	19.02 M$	41.44 M$

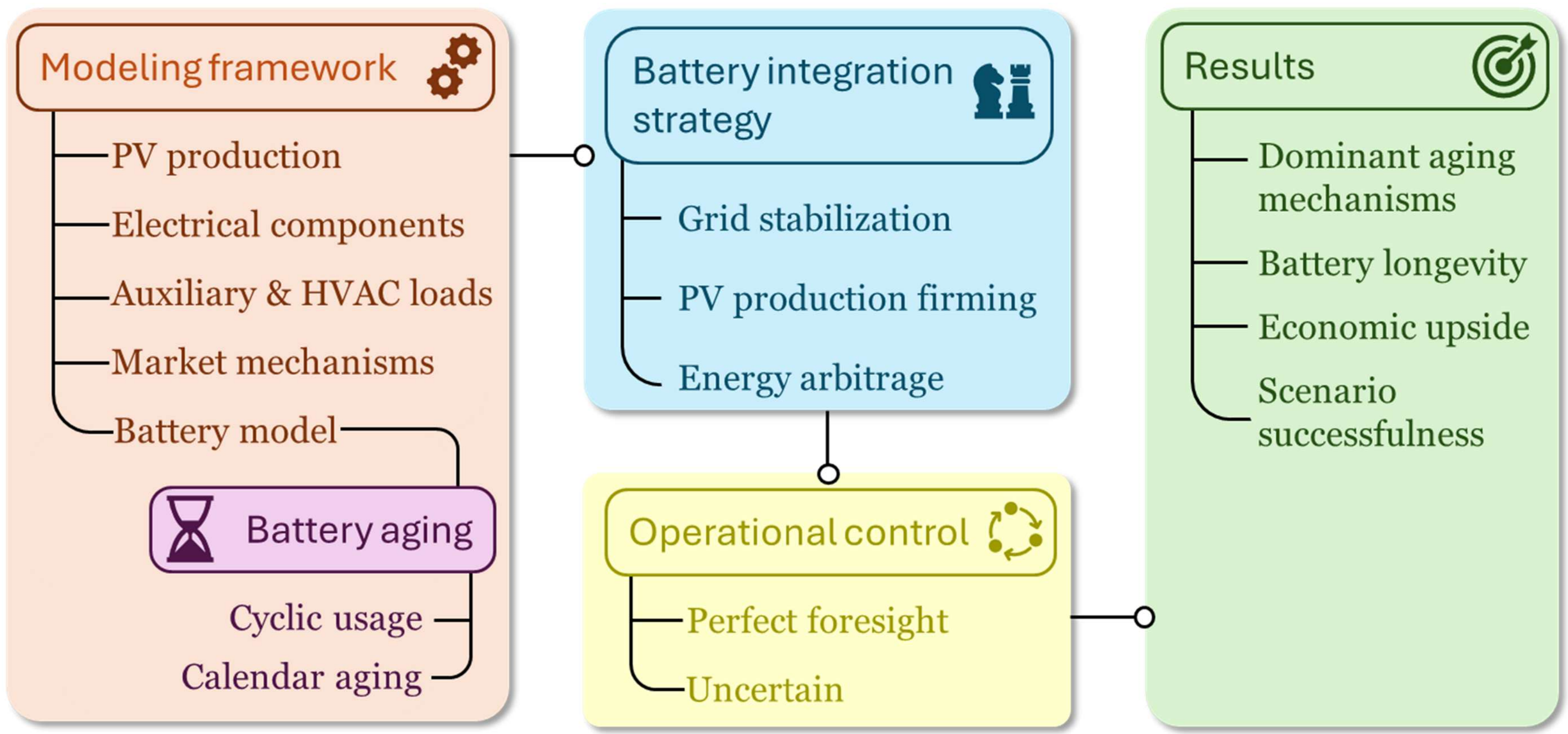

Figure 4.39 -PV-BESS integration complete framework

CHAPTER 5 CONCLUSION AND RECOMMENDATIONS

5.1 Conclusion

The objective of this thesis was to model and optimize the performance of a battery energy storage system in a utility-scale solar photovoltaic power plant. To do so, the research addressed three key pillars of utility-scale PV-BESS: accurate representation of PV generation, realistic representation of battery behavior and aging, and operational strategies that link technical performance with economic outcomes. The complete Julia model developed through this thesis is summarized and presented in Figure 5.1 (p. 127).

The first contribution of this work was to implement in Julia the necessary models to calculate the incident radiation on PV panels and their production. The PV models were based on Duffie & Beckman's work (2013). Additionally, one aspect often neglected in PV simulations using typical hourly weather data files is the short-term variations in solar radiation, which can have an impact on the assessment of curtailment and battery cycling. One contribution of this thesis is the reproduction and improvement of a downscaling methodology based on the Hofmann (2014) approach. By reconstructing sub-hourly irradiance and PV output, this method captured short-term variability that is critical for BESS management. The results showed that ignoring minute-level fluctuations can lead to the underestimation of cyclic battery aging, highlighting the importance of minute-resolution PV data for realistic PV-BESS simulations. The method was tested against measured and modeled PV data and achieved an error of 0.8 % and 0.3 %, respectively.

The second contribution of this work was to present a full-domain equivalent circuit model for lithium iron phosphate (lithium ferro phosphate, LFP) batteries, parameterized using only datasheet information and valid across the complete (SOC, I) operating range of the cell. The model combined low complexity computational need with good accuracy as, for the selected commercial cell, the normalized mean absolute error across all current rates was equal to 0.34 % and R^2 = 0.9803. A generic formulation suitable for early-stage simulations was also proposed, as a solution when detailed datasheet information is unavailable. A complete aging model, separated into calendar and cyclic contributions, was also developed and fitted using experimental data from the same commercial cell.

Finally, this thesis investigated different BESS integration strategies, linking operational behavior with economic outcomes. The analysis showed that profitability was achieved only under the energy arbitrage scenario, and even then, additional revenue mechanisms were necessary to reach economic viability. The other scenarios offered no financial benefits but remained relevant for grid security purposes. Additionally, the results showed that the main drivers for battery aging are different in each scenario.

Overall, this work presents a comprehensive modeling framework for PV-BESS power plants, combining high-resolution data with detailed BESS simulation to ensure technical accuracy, while considering technical and economic constraints. The methodology developed in this work supports the design, management, and techno-economic assessment of future utility-scale solar power plants, particularly as PV penetration increases and the role of energy storage continues to grow.

5.2 Recommendations

The results of this thesis lead to several practical recommendations for the design and operation of utility-scale PV plants equipped with BESS:

- Using an hourly time step is not appropriate for BESS integration studies, as it significantly underestimates battery utilization, despite being commonly adopted in most energy simulation software.
- An effective mitigation strategy to reduce battery degradation, that does not limit battery utilization, is to monitor its SOC to avoid prolonged resting periods at high SOC.
- For AC/DC architectures, round-trip efficiency is often assumed to be constant around 91 %. However, the results of this work showed that using a detailed battery model could result in better performance (in the first two scenarios) or worse performance (energy arbitrage).
- The increasing penetration of renewable energy sources is reshaping intraday electricity price profiles, with prices being low or even negative during periods of high PV production and then increasing during evening demand peaks. In this context, BESS are becoming an essential component of the financial viability of utility-scale solar power plants by enabling energy shifting to higher-paid periods.
- Despite declining battery costs, public support mechanisms such as tax credits remain necessary to ensure the economic feasibility of PV-BESS projects. These mechanisms play a critical role in reducing the necessary CAPEX and ensuring the profitability of BESS addition.

5.3 Future research directions

Several extensions of this work can be considered to further improve the modeling and operational assessment of PV-BESS systems.

- **Thermal effects:** Integrate temperature-dependent battery behavior to improve performance and lifetime predictions under varying climatic conditions.
- **Additional revenue streams:** Extend the economic analysis to include virtual bidding markets and ancillary services (e.g., frequency regulation, reserves) to improve BESS profitability.
- **Long-duration storage:** Investigate 8-10 hour storage configurations to reduce average SOC, mitigate calendar aging, and downsize BESS accessories.
- **Real-time control:** Develop real-time battery control strategies to improve robustness to forecast errors and optimize the trade-off between operational performance and degradation.
- **Data-driven modeling approaches:** Investigate the possibility of developing simplified, technology-agnostic models trained on large datasets generated from high-fidelity electrochemical models. Such approaches could enable fast evaluation of multiple operating scenarios while maintaining a representative description of battery behavior.
- **Digital twins integration:** Explore the development of adaptive digital twins based on AI techniques, capable of rapidly calibrating to operational data. This would help reduce dependence on extensive laboratory testing, while facilitating real-time monitoring and control of PV-BESS systems.

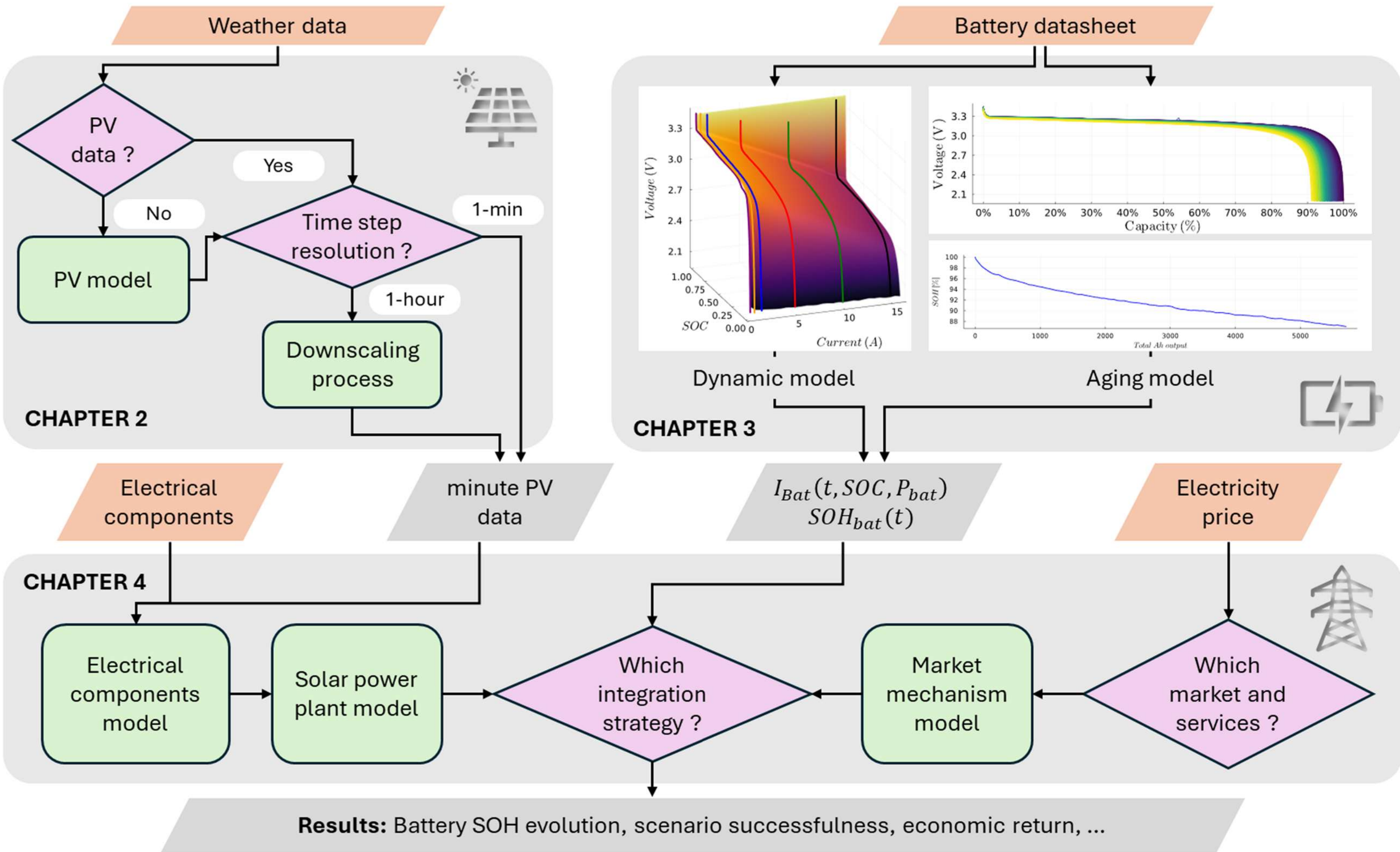

Figure 5.1 – Complete framework graphical presentation

REFERENCES

A123. (2019, January). *Datasheet ANR26650M1B*. https://a123batteries.com/product_images/uploaded_images/26650.pdf

Ankit, R. (2023). *WebPlotDigitizer*. https://automeris.io/

Apribowo, C. H. B., Sarjiya, S., Hadi, S. P., & Wijaya, F. D. (2022). Optimal Planning of Battery Energy Storage Systems by Considering Battery Degradation due to Ambient Temperature: A Review, Challenges, and New Perspective. *Batteries*, *8*(12), 290. https://doi.org/10.3390/batteries8120290

Arote, S. A. (2022). Fundamentals and perspectives of lithium-ion batteries. In *Lithium-ion and Lithium–Sulfur Batteries* (pp. 1–1 to 1–26). IOP Publishing. https://doi.org/10.1088/978-0-7503-4881-2ch1

ASHRAE. (2025). Chap. 15: Fenestration. In *2025 ASHRAE Handbook—Fundamentals*. American Society of Heating, Refrigerating and Air-Conditioning Engineers.

Battery model—PVsyst documentation. (n.d.). Retrieved January 16, 2025, from https://www.pvsyst.com/help/physical-models-used/batteries/battery-model/index.html

Bezanson, J., Edelman, A., Karpinski, S., & Shah, V. B. (2017). Julia: A Fresh Approach to Numerical Computing. *SIAM Review*, *59*(1), 65–98. https://doi.org/10.1137/141000671

Boparai, K. S., & Singh, R. (2020). Electrochemical Energy Storage Using Batteries, Superconductors and Hybrid Technologies. In *Encyclopedia of Renewable and Sustainable Materials* (pp. 248–254). Elsevier. https://doi.org/10.1016/B978-0-12-803581-8.11277-9

CAISO. (2025). *2024 Special Report on Battery Storage* (p. 28). California Independent System Operator. https://www.caiso.com/documents/2024-special-report-on-battery-storage-may-29-2025.pdf

Chandler, D. (2014, June 9). Seeing how a lithium-ion battery works. *MIT News*. https://energy.mit.edu/news/seeing-how-a-lithium-ion-battery-works/

Chen, Y., Kang, Y., Zhao, Y., Wang, L., Liu, J., Li, Y., Liang, Z., He, X., Li, X., Tavajohi, N., & Li, B. (2021). A review of lithium-ion battery safety concerns: The issues, strategies, and testing standards. *Journal of Energy Chemistry*, *59*, 83–99. https://doi.org/10.1016/j.jechem.2020.10.017

Chueh, W. C., Onori, S., Cui, X., Lam, V., Stroebl, F., & Uppaluri, M. (2024). *Stanford Long Term Calendar Aging Dataset*. https://doi.org/10.17605/OSF.IO/JU325

CPUC. (2025). *2023 Ressource adequacy report* (No. 17; CPUC RA Report, p. 73). California Public Utilities Commision. https://www.cpuc.ca.gov/-/media/cpuc-website/divisions/energy-division/documents/resource-adequacy-homepage/2023-resource-adequacy-reportv2.pdf

Cugnet, M. (2024). Vieillissement des accumulateurs lithium-ion. *Conversion de l'énergie électrique*. https://doi.org/10.51257/a-v1-d7000

Desert Knowledge Australia Centre. (2016). *Yulara Solar System, Australia, including photovoltaic generation and meteorological data* [Download dataset; CSV]. https://dkasolarcentre.com.au/download?location=yulara

DOE. (n.d.). *Engineering Reference—EnergyPlus 25.1 Documentation* (p. 2025) [Technical Documentation]. U.S. Department of Energy.

DOE. (2023). *Long Duration Energy Storage*. US Department of Energy. Pathways to Commercial Liftoff. https://liftoff.energy.gov/long-duration-energy-storage/

Duffie, J. A., & Beckman, W. A. (2013). *Solar Engineering of Thermal Processes* (Fourth edition). Wiley.

Durvasulu, V., Murphy, C., & Denholm, P. (2021). *Evaluating Utility-Scale PV Battery Hybrid in Operational Models for the Bulk Power System.* (NREL/TP-6A20-78850). National Renewable Energy Laboratory. https://docs.nlr.gov/docs/fy21osti/78850.pdf

EIA. (2024, June 25). *Utilities report batteries are most commonly used for arbitrage and grid stability*. https://www.eia.gov/todayinenergy/detail.php?id=62405

EnergyOnline. (2024). *CAISO - Real-time electricity price* [Dataset]. California Independent System Operator. https://www.energyonline.com/Data/GenericData.aspx?DataId=19&CAISO___Real-time_Price

EnergyX. (2025). *20ft 2MWh Outdoor Liquid-Cooling Energy Storage Container for BESS System*. https://www.energy-x.org/energy-storage-system-solutions/2mwh-outdoor-liquid-cooling-energy-storage-container.html

Equans. (2025). *Cotoperi Solar Farm, weather and production data* [Dataset]. Personnal communication.

Erbs, D. G., Klein, S. A., & Duffie, J. A. (1982). Estimation of the diffuse radiation fraction for hourly, daily and monthly-average global radiation. *Solar Energy*, *28*(4), 293–302. https://doi.org/10.1016/0038-092X(82)90302-4

F. Holmgren, W., W. Hansen, C., & A. Mikofski, M. (2018). pvlib python: A python package for modeling solar energy systems. *Journal of Open Source Software*, *3*(29), 884. https://doi.org/10.21105/joss.00884

Fan, Y., Zhang, Z., Yang, G., Pan, T., Tian, J., Li, M., Liu, X., & Wang, P. (2025). A comparative study of modeling and parameter identification for lithium-ion batteries in energy storage systems. *Measurement*, *243*, 116263. https://doi.org/10.1016/j.measurement.2024.116263

First Solar. (2024). *FS-7540A-FT1 Datasheet* [Technical Documentation]. First Solar Inc. http://64.34.194.100/pt-BR/-/media/First-Solar/Technical-Documents/Series-7/Series-7-FT1-Datasheet.ashx?la=en

Forbes, C., Evans, M., Hastings, N., & Peacock, B. (2010). *Statistical Distributions* (1st ed.). Wiley. https://doi.org/10.1002/9780470627242

Ge, M., & Friedrich, J. (2024, December 5). *Where Do Emissions Come From? 4 Charts Explain Greenhouse Gas Emissions by Sector*. World Ressource Institute. https://www.wri.org/insights/4-charts-explain-greenhouse-gas-emissions-countries-and-sectors

Geisbauer, C., Wöhrl, K., Koch, D., Wilhelm, G., Schneider, G., & Schweiger, H.-G. (2021). Comparative Study on the Calendar Aging Behavior of Six Different Lithium-Ion Cell Chemistries in Terms of Parameter Variation. *Energies*, *14*(11), 3358. https://doi.org/10.3390/en14113358

Gevorgian, V., Koralewicz, P., Shah, S., & Mendiola, E. (2022). *Photovoltaic Plant and Battery Energy Storage System Integration at NREL's Flatirons Campus* (NREL/TP-5D00-81104). National Renewable Energy Laboratory. https://docs.nlr.gov/docs/fy22osti/81104.pdf

Ghosh, S., Roy, J. N., & Chakraborty, C. (2022). A model to determine soiling, shading and thermal losses from PV yield data. *Clean Energy*, *6*(2), 372–391. https://doi.org/10.1093/ce/zkac014

Gifford, J. (2020, August 4). Why Large-Scale Solar Alone no Longer Makes Sense. *PV Magazine*. https://www.pv-magazine.com/webinars/why-large-scale-solar-alone-no-longer-makes-sense/

Grid Status. (2025, January 14). https://www.gridstatus.io/

Gutsch, M., & Leker, J. (2024). Costs, carbon footprint, and environmental impacts of lithium-ion batteries – From cathode active material synthesis to cell manufacturing and recycling. *Applied Energy*, *353*, 122132. https://doi.org/10.1016/j.apenergy.2023.122132

Heydarzadeh, M., & Toivola, T. (2024). *NMC, NCA, and LFP Cells Degradation Under Randomized Current Profiles* (p. 5379266617) [Dataset]. Mohsen Heydarzadeh. https://doi.org/10.23729/B07462E8-9E31-428C-BDD5-DEB1890C608B

Hofmann, M., Riechelmann, S., Crisosto, C., Mubarak, R., & Seckmeyer, G. (2014). Improved Synthesis of Global Irradiance with One-Minute Resolution for PV System Simulations. *International Journal of Photoenergy*, *2014*, 1–10. https://doi.org/10.1155/2014/808509

Hotz, L., & Berini, P. (2025, October 20). *The State of BESS in CAISO: Key Takeaways through 2025 Q3*. Modo Energy. https://modoenergy.com/research/fr/battery-caiso-bess-resource-adequacy-capacity-energy-arbitrage-2025-q3

IEA. (2024a). *Integrating Solar and Wind—Global Experience and Emerging Challenges*. International Energy Agency. https://www.iea.org/reports/integrating-solar-and-wind

IEA. (2024b, July 19). Global electricity demand set to rise strongly this year and next, reflecting its expanding role in energy systems around the world. *IEA*. https://www.iea.org/news/global-electricity-demand-set-to-rise-strongly-this-year-and-next-reflecting-its-expanding-role-in-energy-systems-around-the-world

IEC. (2017). *Power transformers—Energy efficiency* (IEC TS 60076-20:2017-01; Version Edition 1.0). International Electrotechnical Commission. https://atecco.ir/fa/wp-content/uploads/2025/06/IEC60076-20-2017.pdf

Islam, A., Jawad, A., & Masood, N.-A. (2024). Optimal dispatch strategy of battery energy storage system in utility-scale photovoltaic integrated grid under variability. *Journal of Energy Storage*, *95*, 112562. https://doi.org/10.1016/j.est.2024.112562

Janic, Z., Gavrilov, N., & Roketinec, I. (2023). Influence of Cooling Management to Transformer Efficiency and Ageing. *Energies*, *16*(12), 4626. https://doi.org/10.3390/en16124626

K2 Energy Solutions, Inc. (n.d.-a). *Datasheet K2 LFP18650E-1500*. Retrieved February 4, 2025, from https://www.batteriesinaflash.com/amfile/file/download/file/441/product/17049/

K2 Energy Solutions, Inc. (n.d.-b). *Datasheet K2 LFP18650P - 1250*. Retrieved October 16, 2025, from https://liionbms.com/pdf/k2/LFP18650P.pdf

K2 Energy Solutions, Inc. (n.d.-c). *Datasheet K2 LFP18650P-1350*. Retrieved January 5, 2025, from https://www.batteriesinaflash.com/regular-rechargeable-batteries/k2-energy-3-3v-1350mah-1-35ah-18650p-li-ion-high-capacity-rechargeable-battery

K2 Energy Solutions, Inc. (s. d.a). *K2 HIGH CAPACITY LFP18650P-1350-02 Power cell Datasheet*. https://www.batteriesinaflash.com/amfile/file/download/file/440/product/17052/

K2 Energy Solutions, Inc. (s. d.b). *K218650E02 High Capacity Energy Cell Datasheet*. https://www.master-instruments.com.au/products/62567/k218650e.html

Kummert, M. (2024). *Rayonnement solaire* [Lecture slides]. MEC6214 – Énergie solaire et applications, Polytechnique Montréal.

Lam, V. N., Cui, X., Stroebl, F., Uppaluri, M., Onori, S., & Chueh, W. C. (2025). A decade of insights: Delving into calendar aging trends and implications. *Joule*, *9*(1), 101796. https://doi.org/10.1016/j.joule.2024.11.013

LegalClarity. (2025, December 8). *Federal Tax Incentives for Battery Storage Systems*. https://legalclarity.org/federal-tax-incentives-for-battery-storage-systems/

LithiumWerks. (2021, June). *Datasheet APR18650M1B*. https://www.master-instruments.com.au/file/61900/1/Lithiumwerks-APR18650M1B.pdf

LithiumWerks. (2024, September). *DatasheetANR26650M1B*. https://lithiumwerksbatteries.com/lithiumwerks-anr26650m1b-3-3-v-2-6-ah-lithium-iron-phosphate-lifepo4-battery/

Llamas-Orozco, J. A., Meng, F., Walker, G. S., Abdul-Manan, A. F. N., MacLean, H. L., Posen, I. D., & McKechnie, J. (2023). Estimating the environmental impacts of global lithium-ion battery supply chain: A temporal, geographical, and technological perspective. *PNAS Nexus*, *2*(11), pgad361. https://doi.org/10.1093/pnasnexus/pgad361

Lo Franco, F., Morandi, A., Raboni, P., & Grandi, G. (2021). Efficiency Comparison of DC and AC Coupling Solutions for Large-Scale PV+BESS Power Plants. *Energies*, *14*(16), 4823. https://doi.org/10.3390/en14164823

LONGI solar. (2024). *LR7-72HGD-620M Bifacial Datasheet* [Technical Documentation]. LONGi Green Energy Technology Co., Ltd. https://static.longi.com/L_Gi_LE_PM_T_PMD_059_F151_LR_7_72_HGD_595_625_M_V2_30_30_and_15_V8_0_EN_9e801112d3.pdf

Marie, J.-J., & Gifford, S. (2023). Developments in lithium-ion battery cathodes. *The Faraday Institution*, (18).

Medhi, A., & Moherenhout, T. (2023, September 20). The IRA and the US Battery Supply Chain: One Year On. *Center on Global Energy Policy at Columbia*. https://www.energypolicy.columbia.edu/publications/the-ira-and-the-us-battery-supply-chain-one-year-on/

Meng, H., Jia, H., Xu, T., Wei, W., Wu, Y., Liang, L., Cai, S., Liu, Z., Wang, R., & Li, M. (2022). Optimal configuration of cooperative stationary and mobile energy storage considering ambient temperature: A case for Winter Olympic Game. *Applied Energy*, *325*, 119889. https://doi.org/10.1016/j.apenergy.2022.119889

NASA. (2025). *National Aeronautics and Space Administration (NASA) Langley Research Center (LaRC) Prediction Of Worldwide Energy Resources (POWER) Project funded through the NASA Earth Science/Applied Science Program.* (Version v10.0.0) [Dataset]. https://power.larc.nasa.gov/

Navas, S. J., González, G. M. C., Pino, F. J., & Guerra, J. J. (2023). Modelling Li-ion batteries using equivalent circuits for renewable energy applications. *Energy Reports*, *9*, 4456–4465. https://doi.org/10.1016/j.egyr.2023.03.103

Nguyen Quoc Minh, Nguyen Duy Linh, Nguyen Trong Khiem, Tran Huu Quynh, Pham Tuan Nghia, & Bui Minh Quan. (2023). Optimization models to flatten duck curve in power grid with high penetration of solar energy. *Journal of Military Science and Technology*, *91*, 45–53. https://doi.org/10.54939/1859-1043.j.mst.91.2023.45-53

NREL. (2015). *Technoeconomic Modeling of Battery Energy Storage in SAM* (TNREL/TP-6A20-64641). National Renewable Energy Laboratory. https://docs.nrel.gov/docs/fy15osti/64641.pdf

NREL. (2024a). *Utility-Scale Battery Storage*. National Renewable Energy Laboratory. https://atb.nrel.gov/electricity/2024/utility-scale_battery_storage

NREL. (2024b). *Utility-Scale Battery Storage Annual Technology Baseline*. National Renewable Energy Laboratory. NREL Annual Technology Baseline. https://atb.nrel.gov/electricity/2024/utility-scale_battery_storage

NREL. (2025). *System Advisor Model™ Version 2025.4.16 (SAM™ 2025.4.16) Website. Financial models*. National Renewable Energy Laboratory. Government Research Laboratory Website. https://sam.nrel.gov/financial-models.html

Olis, W., Rosewater, D., Nguyen, T., & Byrne, R. H. (2023). Impact of heating and cooling loads on battery energy storage system sizing in extreme cold climates. *Energy*, *278*, 127878. https://doi.org/10.1016/j.energy.2023.127878

Omoyele, O., Hoffmann, M., Koivisto, M., Larrañeta, M., Weinand, J. M., Linßen, J., & Stolten, D. (2024). Increasing the resolution of solar and wind time series for energy system modeling: A review. *Renewable and Sustainable Energy Reviews*, *189*, 113792. https://doi.org/10.1016/j.rser.2023.113792

Pandey, S. (2017). Analysis of Auxiliary Energy consumption in Utility scale Solar PV Power plant. *International Journal of Current Engineering and Technology*, *7*(5).

Pedroza-Díaz, A., Rodrigo, P. M., Dávalos-Orozco, Ó., De-la-Vega, E., & Valera-Albacete, Á. (2025). Review of explicit models for photovoltaic cell electrical characterization. *Renewable and Sustainable Energy Reviews*, *207*, 114979. https://doi.org/10.1016/j.rser.2024.114979

Peukert, W. (1897). Über die Abhängigkeit der Kapazität von der Entladestromstärke bei Bleiakkumulatoren. *Elektrotechnische Zeitschrift*, *20*.

Pierro, M., Perez, R., Perez, M., Prina, M. G., Moser, D., & Cornaro, C. (2021). Italian protocol for massive solar integration: From solar imbalance regulation to firm 24/365 solar generation. *Renewable Energy*, *169*, 425–436. https://doi.org/10.1016/j.renene.2021.01.023

Pitra, G. M., & Musti, K. S. S. (2021). Duck Curve with Renewable Energies and Storage Technologies. *2021 13th International Conference on Computational Intelligence and Communication Networks (CICN)*, 66–71. https://doi.org/10.1109/CICN51697.2021.9574671

Plumer, B., & Popovich, N. (2024). Giant Batteries Are Transforming the Way the U.S. Uses Electricity. *The New York Times*. https://www.nytimes.com/interactive/2024/05/07/climate/battery-electricity-solar-california-texas.html

Prakash, A., Bruce, A., & MacGill, I. (2025). The scheduling role of future pricing information in electricity markets with rising deployments of energy storage: An Australian National Electricity Market case study. *Energy Economics*, *142*, 108191. https://doi.org/10.1016/j.eneco.2025.108191

Prakash, K., Ali, M., Siddique, M. N. I., Chand, A. A., Kumar, N. M., Dong, D., & Pota, H. R. (2022). A review of battery energy storage systems for ancillary services in distribution grids: Current status, challenges and future directions. *Frontiers in Energy Research*, *10*, 971704. https://doi.org/10.3389/fenrg.2022.971704

Precedence Research. (2024, October 8). *Solar Cell Market Size, Share, and Trends 2024 to 2034*. Precedence Research. https://www.precedenceresearch.com/solar-cell-market

Preger, Y., Barkholtz, H. M., Fresquez, A., Campbell, D. L., Juba, B. W., Romàn-Kustas, J., Ferreira, S. R., & Chalamala, B. (2020). Degradation of Commercial Lithium-Ion Cells as a Function of Chemistry and Cycling Conditions. *Journal of The Electrochemical Society*, *167*(12), 120532. https://doi.org/10.1149/1945-7111/abae37

Pullutasig, B., & Belding, S. (2024). *Evaluating Utility Costs Savings and Resilience: A Case Study in Port Arthur, Texas* (PR-7A40-87735). NREL. https://docs.nrel.gov/docs/fy25osti/87735.pdf

PVsyst. (n.d.). *PVsyst Documentation Overview*. Retrieved https://www.pvsyst.com/help/

PVsyst. (2015). *Generic polycrystalline PV module 250 Wp (60 cells)* [Internal PV module model].

PVsyst SA. (n.d.). *Grid inverter Model*. PVsyst Documentation. Retrieved https://www.pvsyst.com/help/physical-models-used/grid-inverter/inverter-model-efficiency.html

PVsyst SA. (2025). *PVsyst* (Version 8.0) [Computer software]. https://www.pvsyst.com

Rahman, M. M., Dadon, S. H., He, M., Giesselmann, M., & Hasan, M. M. (2024). An Overview of Power System Flexibility: High Renewable Energy Penetration Scenarios. *Energies*, *17*(24), 6393. https://doi.org/10.3390/en17246393

Ríos-Ledesma, F., Barrutia, L., Ramírez-Ledesma, J., Narvarte, L., & Lorenzo, E. (2026). Angular losses in photovoltaic energy estimation: A review of models and a comparative analysis using the enhanced SISIFO simulation tool. *Renewable and Sustainable Energy Reviews*, *226*, 116377. https://doi.org/10.1016/j.rser.2025.116377

Rosewater, D. M., Copp, D. A., Nguyen, T. A., Byrne, R. H., & Santoso, S. (2019). Battery Energy Storage Models for Optimal Control. *IEEE Access*, *7*, 178357–178391. https://doi.org/10.1109/ACCESS.2019.2957698

R-Smith, N. A.-Z., Moertelmaier, M., Gramse, G., Kasper, M., Ragulskis, M., Groebmeyer, A., Jurjovec, M., Brorein, E., Zollo, B., & Kienberger, F. (2023). Fast method for calibrated self-discharge measurement of lithium-ion batteries including temperature effects and comparison to modelling. *Energy Reports*, *10*, 3394–3401. https://doi.org/10.1016/j.egyr.2023.10.031

Saldaña, G., Martín, J. I. S., Zamora, I., Asensio, F. J., Oñederra, O., & González-Pérez, M. (2022). Empirical calendar ageing model for electric vehicles and energy storage systems batteries. *Journal of Energy Storage*, *55*, 105676. https://doi.org/10.1016/j.est.2022.105676

Sarasketa-Zabala, E., Gandiaga, I., Rodriguez-Martinez, L. M., & Villarreal, I. (2014). Calendar ageing analysis of a LiFePO4/graphite cell with dynamic model validations: Towards realistic lifetime predictions. *Journal of Power Sources*, *272*, 45–57. https://doi.org/10.1016/j.jpowsour.2014.08.051

Serafin, T., & Weron, R. (2025). Loss functions in regression models: Impact on profits and risk in day-ahead electricity trading. *Energy Economics*, *148*, 108596. https://doi.org/10.1016/j.eneco.2025.108596

Shepherd, C. M. (1965). Design of Primary and Secondary Cells. *Journal of The Electrochemical Society*, *112*(7), 657. https://doi.org/10.1149/1.2423659

SMA. (2024). *Sunny Central 4600 UP – Technical Datasheet* [Datasheet]. SMA Solar Technology AG. https://www.sma.de/en/products/solarinverters/sunny-central-up

Sobianowska-Turek, A., Urbańska, W., Janicka, A., Zawiślak, M., & Matla, J. (2021). The Necessity of Recycling of Waste Li-Ion Batteries Used in Electric Vehicles as Objects Posing a Threat to Human Health and the Environment. *Recycling*, *6*(2), Article 2. https://doi.org/10.3390/recycling6020035

Staadecker, M., Szinai, J., Sánchez-Pérez, P. A., Kurtz, S., & Hidalgo-Gonzalez, P. (2024). The value of long-duration energy storage under various grid conditions in a zero-emissions future. *Nature Communications*, *15*(1), 9501. https://doi.org/10.1038/s41467-024-53274-6

SunPower. (2011). *SPR-327NE-WHT-D PV Datasheet* [Technical Documentation]. SunPower Corporation. https://www.mvcommission.org/sites/default/files/docs/DATASHEET___SPR_327NE_WHT_D_FOR_NORTH_AMERICA.pdf

Synergy. (2023). *Graphical representation of the "Duck Curve" in western Australia* [Graphic]. https://www.synergy.net.au/Blog/2021/10/Everything-you-need-to-know-about-the-Duck-Curve

Thakur, P., & Labanya Prakash, L. (2024, May 10). *How to finance battery energy storage*. World Economic Forum. https://www.weforum.org/stories/2024/05/how-to-finance-battery-energy-storage-clean-energy/

Tremblay, O., Dessaint, L.-A., & Dekkiche, A.-I. (2007). A Generic Battery Model for the Dynamic Simulation of Hybrid Electric Vehicles. *2007 IEEE Vehicle Power and Propulsion Conference*, 284–289. https://doi.org/10.1109/VPPC.2007.4544139

Vermeer, W., Chandra Mouli, G. R., & Bauer, P. (2022). A Comprehensive Review on the Characteristics and Modeling of Lithium-Ion Battery Aging. *IEEE Transactions on Transportation Electrification*, *8*(2), 2205–2232. https://doi.org/10.1109/TTE.2021.3138357

Wang, J., Liu, P., Hicks-Garner, J., Sherman, E., Soukiazian, S., Verbrugge, M., Tataria, H., Musser, J., & Finamore, P. (2011). Cycle-life model for graphite-LiFePO4 cells. *Journal of Power Sources*, *196*(8), 3942–3948. https://doi.org/10.1016/j.jpowsour.2010.11.134

Wang, Z., Li, S., Jin, Z., Li, Z., Liu, Q., & Zhang, K. (2023). Oil and gas pathway to net-zero: Review and outlook. *Energy Strategy Reviews*, *45*, 101048. https://doi.org/10.1016/j.esr.2022.101048

Wiatros-Motyka, M. (2025). *Global Electricity Mid-Year Insights 2025*. EMBER. https://ember-energy.org/app/uploads/2025/10/Global-Electricity-Mid-Year-Insights-2025-PDF.pdf

Wilcox, S. ., & Andreas, A. (2007). *Solar Radiation Monitoring Station (SoRMS): Humboldt State University, Arcata, California (Data)* [Dataset]. https://doi.org/10.5439/1052559

Wilcox, S., & Andreas, A. (2010). *Solar Resource Meteorological Assessment Project (SOLRMAP): Rotating Shadowband Radiometer (RSR); Cedar City, Utah (Data)* [Dataset]. https://doi.org/10.5439/1052231

Xing, Y., He, W., Pecht, M., & Tsui, K. L. (2014). State of charge estimation of lithium-ion batteries using the open-circuit voltage at various ambient temperatures. *Applied Energy*, *113*, 106–115. https://doi.org/10.1016/j.apenergy.2013.07.008

Zhang, H., Qian, Y., Pang, J., Jiang, J., Liu, X., Lan, Q., Qi, X., & Wang, J. (2025). Insight into the effect of current rates on the ageing performance of LiFePO4/graphite cells with ultra-long cycles. *Electrochimica Acta*, *529*, 146290. https://doi.org/10.1016/j.electacta.2025.146290

Zhang, T., Stackhouse, P. W., Macpherson, B., & Colleen Mikovitz, J. (2024). A CERES-based dataset of hourly DNI, DHI and global tilted irradiance (GTI) on equatorward tilted surfaces: Derivation and comparison with the ground-based BSRN data. *Solar Energy*, *274*, 112538. https://doi.org/10.1016/j.solener.2024.112538

APPENDIX A SOLAR IRRADIANCE CALCULATION

The following sections have been adapted from (Kummert, 2024).

I. Solar position calculations

The first step in assessing the photovoltaic power production potential of a site is to estimate the annual solar irradiation it receives. It depends on several factors:

- n, the time of the year [hour]
- Φ, the site latitude
- L_{loc}, the site longitude
- L_{st}, the site time zone longitude
- UTC, the site time zone
- δ, the solar declination
- ω, the solar time
- θ_z, the zenith angle
- γ_s, the azimuth angle
- α_s, the solar altitude
- β, the solar panel slope
- γ, the solar panel azimuth angle

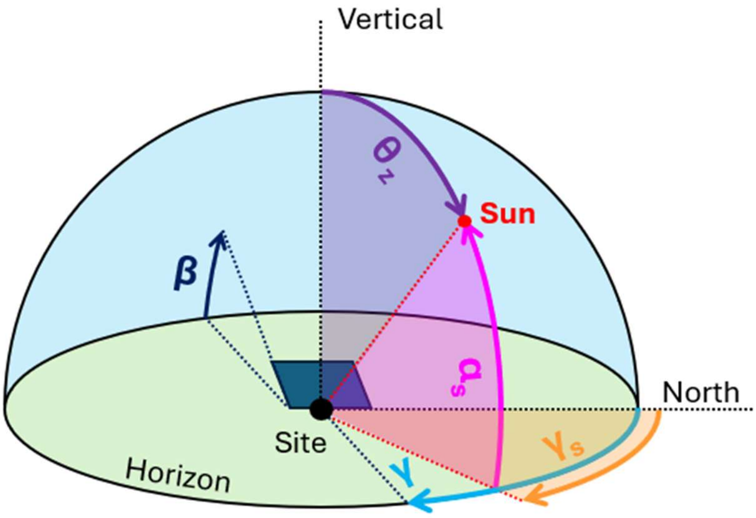

Figure A.1 - Characteristics solar angles

First, the Spencer equation can be used to calculate δ:

$$\begin{cases} \delta = \frac{180}{\pi}\begin{pmatrix} 0.006918 - 0.399912cosB + 0.070257sinB - 0.006758cos2B + 0.000907sin2B \\ -0.002697cos3B + 0.001480sin3B \end{pmatrix} \\ B = \frac{360}{365} * (\frac{n}{24} - 1) \end{cases} \quad 5.1$$

Solar time ω, can then be calculated using L_{st} and E, which is a factor added to consider the eccentricity of the elliptical orbit of the earth and other fluctuations.

$$\begin{cases} E = 2.2918(0.00075 + 0.1868cosB - 3.2077sinB - 1.4615cos2B - 4.0849sin2B) \\ L_{st} = 15 * UTC \\ t_{solar} = \frac{L_{loc} - L_{st}}{15} + t_{civil} + \frac{E}{60} \\ \omega = 15(t_{solar} - 12) \end{cases} \quad 5.2$$

After that, the position of the sun can be determined by calculating its three characteristics angles: θ_z, γ_s and α_s

$$\begin{cases} \theta_z = \operatorname{acos}\left(\cos(\Phi).\cos(\delta).\cos(\omega) + \sin(\Phi).\sin(\delta)\right. \\ \alpha_s = 90 - \theta_z \end{cases} \quad 5.3$$

And

$$\gamma_s = \begin{cases} 180 - \operatorname{acos}\left(\frac{\cos(\theta_z).\sin(\Phi) - \sin(\delta)}{\sin(\theta_z).\cos(\Phi)}\right), & \omega < 0 \\ 180 + \operatorname{acos}\left(\frac{\cos(\theta_z).\sin(\Phi) - \sin(\delta)}{\sin(\theta_z).\cos(\Phi)}\right), & \omega \geq 0 \end{cases} \quad 5.4$$

Finally, $\theta,$ the incidence angle of solar radiation on a given surface, is defined as:

$$\cos(\theta) = \cos(\theta_z).\cos(\beta) + \sin(\theta_z).\sin(\beta).\cos(\gamma - \gamma_s) \quad 5.5$$

II. Solar radiation calculations

Solar radiation reaching Earth's surface is often described by 3 quantities:

- GHI (Global Horizontal Irradiation): The total solar radiation received on a horizontal surface, including both direct and diffuse components. It is often denoted as G.
- DHI (Diffuse Horizontal Irradiation): The portion of solar radiation that has been scattered in multiple directions by the atmosphere before reaching the surface. It is denoted as $\boldsymbol{G_d}$.
- DNI (Direct Normal Irradiation): The solar radiation received directly from the Sun without atmospheric scattering. It is denoted as $\boldsymbol{G_{bn}}$

The total incident radiation on an inclined surface can be calculated thanks to the formula presented below:

$$Global = Direct + Diffuse + Reflected$$

$$G_t = G_{bn}\cos(\theta) + G_d\left(\frac{1+\cos(\beta)}{2}\right) + \rho_G G\left(\frac{1-\cos(\beta)}{2}\right) \quad 5.6$$

Where ρ_G is the ground albedo

APPENDIX B PV PANNELS DATA

This appendix presents the specification of all the different PV panels used in this work.

I. Longi bifacial

Name	LR7-72HGD-620M Bifacial
Used in	Chapter 2, IV curve comparison
	Chapter 2, MPP calculation
	Chapter 4, Solar farm design
Manufacturer	Longi solar
Reference	(LONGI solar, 2024)

Data sheet:

Electrical Characteristics STC : AM1.5 1000W/m² 25°C NOCT : AM1.5 800W/m² 20°C 1m/s

C D A-A B-B

Test uncertainty for Pmax: ±3%

Module Type	LR7-72HGD-595M		LR7-72HGD-600M		LR7-72HGD-605M		LR7-72HGD-610M		LR7-72HGD-615M		LR7-72HGD-620M		LR7-72HGD-625M	
Testing Condition	STC	NOCT	STC	NOCT	STC	NOCT	STC	NOCT	STC	NOCT	STC	NOCT	STC	NOCT
Maximum Power (Pmax/W)	595	452.9	600	456.7	605	460.6	610	464.4	615	468.2	620	472.0	625	475.8
Open Circuit Voltage (Voc/V)	52.23	49.64	52.34	49.74	52.44	49.84	52.55	49.94	52.66	50.04	52.77	50.15	52.88	50.25
Short Circuit Current (Isc/A)	14.45	11.61	14.53	11.67	14.61	11.74	14.69	11.80	14.77	11.86	14.85	11.92	14.93	11.99
Voltage at Maximum Power (Vmp/V)	43.79	41.63	43.90	41.72	44.00	41.82	44.11	41.92	44.22	42.03	44.33	42.13	44.44	42.23
Current at Maximum Power (Imp/A)	13.59	10.88	13.67	10.95	13.75	11.02	13.83	11.08	13.91	11.14	13.99	11.21	14.07	11.27
Module Efficiency(%)	22.0		22.2		22.4		22.6		22.8		23.0		23.1	

Operating Parameters

Operational Temperature	-40°C ~ +85°C
Power Output Tolerance	0 ~ 3%
Maximum System Voltage	DC1500V (IEC/UL)
Maximum Series Fuse Rating	30A
Nominal Operating Cell Temperature	45±2°C
Protection Class	Class II
Bifaciality	80±5%
Fire Rating	UL type 29 IEC Class C

Mechanical Loading

Front Side Maximum Static Loading	5400Pa
Rear Side Maximum Static Loading	2400Pa
Hailstone Test	25mm Hailstone at the speed of 23m/s

Temperature Ratings (STC)

Temperature Coefficient of Isc	+0.045%/°C
Temperature Coefficient of Voc	-0.230%/°C
Temperature Coefficient of Pmax	-0.280%/°C

Figure B.1 - LR7-72HGD-620M Bifacial datasheet

II. PVsyst

Name	Poly160Wp36 Generic panel
Used in	Chapter 2, IV curve comparison
Manufacturer	PVsyst generic panel
Reference	(PVsyst, 2015)

Data sheet:

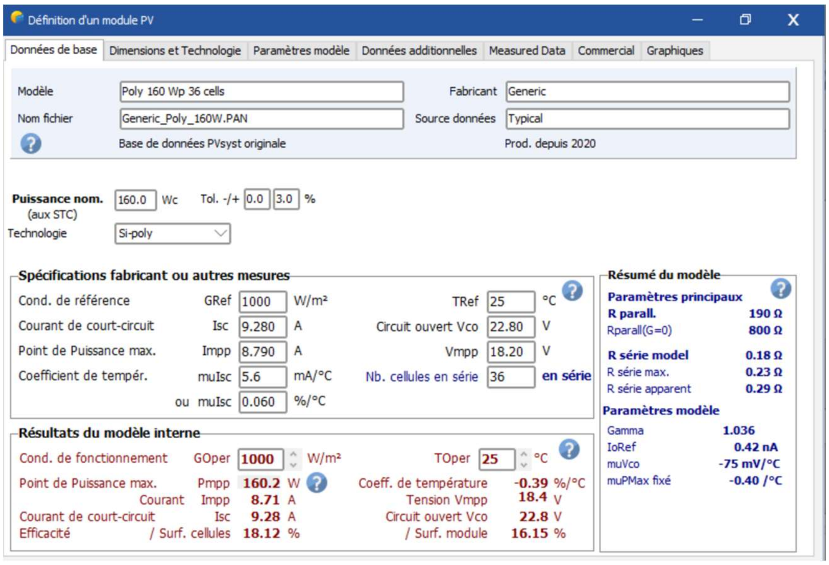

Figure B.2 - Poly160Wp36 Generic panel datasheet

III. First solar panel

Name	FS-7540A-FT1
Used in	Chapter 2, IV curve comparison
Manufacturer	First Solar
Reference	(First Solar, 2024)

Data sheet:

MODEL TYPES: FS-7XXXA-FT1 (XXX = NOMINAL POWER)
RATINGS AT STANDARD TEST CONDITIONS (1000W/m², AM 1.5, 25°C)[2]

Nominal Power[3] (-0/+5%)	P_{MAX} (W)	525	530	535	540	545	550
Efficiency (%)	%	18.8	19.0	19.1	19.3	19.5	19.7
Cell Efficiency (%)	%	19.7	19.9	20.1	20.3	20.4	20.6
Voltage at P_{MAX}	V_{MAX} (V)	186.0	186.9	187.8	188.7	189.6	190.4
Current at P_{MAX}	I_{MAX} (A)	2.82	2.84	2.85	2.86	2.88	2.89
Open Circuit Voltage	V_{OC} (V)	226.1	226.7	227.2	227.7	228.2	228.8
Short Circuit Current	I_{SC} (A)	3.04	3.05	3.06	3.06	3.07	3.08
Maximum System Voltage	V_{SYS} (V)	1500[5]					
Limiting Reverse Current	I_R (A)	5.0					
Maximum Series Fuse	I_{CF} (A)	5.0					

TEMPERATURE CHARACTERISTICS

Module Operating Temperature Range	(°C)	-40 to +85
Temperature Coefficient of P_{MAX}	T_K (P_{MAX})	-0.32%/°C [Temperature Range: 25°C to 75°C]
Temperature Coefficient of V_{OC}	T_K (V_{OC})	-0.28%/°C
Temperature Coefficient of I_{SC}	T_K (I_{SC})	+0.04%/°C
Nominal Operating Cell Temperature	(°C)	43

PACKAGING INFORMATION

Model Type	Modules Per Pack	Packs per 12m Container
FS-7XXXA-FT1	48	8

Mechanical Specifications

Figure B.3 - FS-7540A-FT1 datasheet

IV. Sunpower solar panel

Name	SPR-327NE-WHT-D PV
Used in	Chapter 2, MPP calculation
Manufacturer	SunPower
Reference	(SunPower, 2011)

Data sheet:

MODEL: SPR-327NE-WHT-D

ELECTRICAL DATA Measured at Standard Test Conditions (STC): irradiance of 1000W/m², AM 1.5, and cell temperature 25° C		
Peak Power (+5/-3%)	P_{max}	327 W
Cell Efficiency	η	22.5 %
Panel Efficiency	η	20.1 %
Rated Voltage	V_{mpp}	54.7 V
Rated Current	I_{mpp}	5.98 A
Open Circuit Voltage	V_{oc}	64.9 V
Short Circuit Current	I_{sc}	6.46 A
Maximum System Voltage	UL	600 V
Temperature Coefficients	Power (P)	– 0.38%/K
	Voltage (V_{oc})	–176.6mV/K
	Current (I_{sc})	3.5mA/K
NOCT		45° C +/– 2° C
Series Fuse Rating		20 A
Grounding	Positive grounding not required	

Figure B.4 - SPR-327NE-WHT-D PV datasheet

APPENDIX C SCENARIO MODEL DETAILS

I. Grid stabilization

1. P_{obj} formulation

The objective of scenario 1 is to transform P_{pv} to shift the energy injected into the grid. The algorithm to define P_{obj} is divided into three steps as follows:

```
:P_bat = [zeros]
:
:i = t_sunrise - t_morning                          #y1 section in the morning
:while P_bat[i] >= P_PV[i]
:      P_bat[i+1]=y1[i+1]
:      if i > t_sunset
:            break
:      end
:      i += 1
:end
:
:j=t_evening + t_sunset                             #y3 section in the evening
: while P_bat[j] >= P_PV[j]
:      P_bat[j-1]=y3[j-1]
:      if j < i
:            break
:      end
:      j += 1
:end
:
:for k in i:j                                       #y2 section in the midday
:      P_bat[k]=min(P_cutoff, P_PV[k]
:end
:
:P_obj = P_bat - P_PV
```

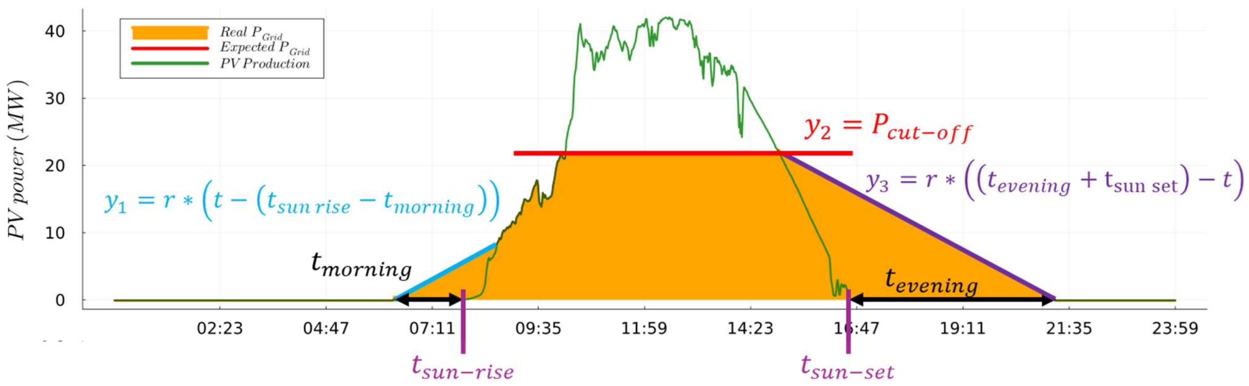

Figure C.1 - P_{obj} determination illustration in scenario 1

r is the ramp-up value and is a function of $\overline{P_{pv}}$ so that it is not as steep in winter as in summer.

$$r = \min\left(0.15, \overline{P_{pv}} * N_{pv}/180\right) \quad \text{C.1}$$

Where N_{pv} is the number of solar panels in the PV power plants, and $\overline{P_{pv}}$ [in GW] is either known in a perfect forecast situation or approximated using the method presented in section 4.3.3. The value of 180 has been chosen to represent a progressive ramp-up over three hours.

2. Penalty weight value

The mathematical optimization formulation of the problem is:

- $Penalty_1 = |SOC_{end} - 0.2| * \gamma_1$
- $Penalty_2 = \sum\left(P_{grid} - P_{obj}\right)^2 * \gamma_2$
- $Penalty_3 = \left(\frac{1}{t_{morning}} + \frac{4}{t_{evening}}\right) * \gamma_3$

The optimization process searches for the set of parameters that minimize the sum of those three penalties:

$$Min_{(t_{morning}, t_{evening}, Cut-off)}(Penalty_1 + Penalty_2 + Penalty_3) \quad \text{C.2}$$

The different penalty weights numerical values are:

$$\begin{cases} \gamma_1 = 3000 \\ \gamma_2 = 1 \\ \gamma_3 = 5000 \end{cases} \quad \text{C.3}$$

3. Generalization formulation

The general formulation of the parameters $t_{morning}$ and $t_{evening}$ is:

$$t_{morning/evening} = \alpha \sin\left(\frac{2\pi}{365} * n + \beta\right) + \gamma \quad \text{C.4}$$

For $t_{morning}$ the parameters are:

Table C.1 - $t_{morning}$ parameters in scenario 1

	α	β	γ
Clear	30.24	1.80	65.78
Broken clouds	45.29	1.80	55.88

Overcast	34.55	1.80	66.00

For $t_{evening}$ the parameters they are:

Table C.2 - $t_{evening}$ parameters in scenario 1

	α	β	γ
Clear	60.28	1.80	175.88
Broken clouds	75.62	1.79	180.16
Overcast	14.56	1.80	284.02

4. Aging adaptation

To adapt the instruction to the battery capacity degradation, the parameters have the following evolution:

$$\begin{cases} P_{cut,off}^{t} = P_{cut,off}^{instruction} * (2 - SOH(t)) \\ t_{evening}^{t} = t_{evening}^{instruction} * SOH(t) \\ t_{morning}^{t} = t_{morning}^{instruction} * SOH(t) \end{cases} \quad \text{C.5}$$

II. Power firming

1. Penalty weight value

The mathematical optimization formulation of the problem is:

- $Penalty_1 = |SOC_{end} - 0.5| * \gamma_1$
- $Penalty_2 = \sum(P_{grid} - P_{obj})^2 * \gamma_2$

The optimization process searches the parameter f that minimizes the sum of those two penalties:

$$Min_f(Penalty_1 + Penalty_2) \quad \text{C.6}$$

The different penalty weights numerical values are:

$$\begin{cases} \gamma_1 = 500 \\ \gamma_2 = 100/maximum(P_{obj}) \end{cases} \quad \text{C.7}$$

2. Generalization formulation

The general formulation of parameter f is:

$$f = \frac{\alpha * \overline{P_{pv}} + \beta}{maximum(G_{ext})} \quad \text{C.8}$$

The paramaters for the different weather class are:

Table C.3 - f parameters in scenario 3

	α	β
Clear	0.223	43.742
Broken clouds	0.389	15.521
Overcast	0.618	-0.852